Air-Sea Interactions during Cold Air Outbreaks in a coupled Mixed Layer Model

Kjersti Konstali

Master Thesis in Climate Dynamics
Geophysical Institute
June 2019

UNIVERSITY OF BERGEN
Faculty of Mathematics and Natural Sciences

Abstract

Cold air outbreaks play a crucial role in the air-sea heat exchange in high latitudes. To explore the sensitivity to ocean coupling, the role of latent heating and the sensitivity to sea ice distributions in cold air outbreaks, we couple an atmospheric to an oceanic mixed layer model. The mixed layer model of the atmosphere is based on the equations for liquid water potential temperature and the total mixing ratio and the oceanic mixed layer model is based on the equations for temperature and salinity. A steady state is obtained through heat exchange between the atmosphere and ocean, as well as advection in the atmosphere and relaxation toward a climatological state in the ocean. The results show that the coupling with the ocean has only a marginal impact on the atmospheric boundary layer structure, but that cold air outbreaks can lead to an increase in the oceanic mixed layer depth. Latent heating acts to increase the atmopsheric boundary layer growth, which leads a reduction of sensible heat fluxes. We further investigate the effect of different sea ice distributions with and without coupling between the atmosphere and ocean, and show that the sea ice distribution does not change the effect of the cold air outbreak when integrating the fluxes from the ice edge to far downstream the fetch, but it does change the distribution of the fluxes and thereby the local response between the atmosphere and the ocean. The model shows that the oceanic mixed layer depth is deeper when there is a sharper transition from sea ice to open water.

Acknowledgements

First of all I would like to thank my main supervisor Thomas Spengler, for not giving me up when I changed my mind for the topic of this thesis every second day for two months. I'm very pleased with the topic we agreed on in the end. It has been challenging, but mostly enjoyable. Hands-on experience in the IGP flight campaign in Iceland was a motivational boost (I would like to thank Harald Sodemann who provided a place for me to stay), and flying over the sea ice edge outside of Greenland in a small Twin Otter was spectacular. Not only was I given the opportunity to go to Iceland, but I was able to participate at the NORPAN workshop, both in Japan and in Bergen. So really, thanks for believing enough in my science to let me participate.

Apart from that, I would like to thank both Thomas Spengler and Clemens Spensberger for the thorough proofreading, the endless amount of e-mails I never answered to, and not least the discussions. And thanks for letting me do things at my own pace without interfering too much. However, thanks for good guidance and advice, such as telling me to start writing in September.

Thanks to Ådne for feeding me during times I had planned on eating Wasa Husman for dinner and for keeping my spirits high the last semester. However, most of all I would like to thank all my fellow classmates through all my years at GFI. Thanks for the study sessions, the lunch breaks, the ligretto breaks, the other breaks, and friendships that extend beyond GFI. Also, I will never forget our Julebord, which somehow always exceeds expectations.

And finally, thanks to everyone who contributed to the proof reading I forced upon them, especially my Canadian friend who gave a lot of useful comments and suggestions. I'll be your guide again if you ever come back to Norway.

Contents

Todo list

List of Figures

List of Tables

Acronyms

ABL	Atmospheric Boundary Layer
AMOC	Atlantic Meridional Overturning Circulation
CAO	Cold Air Outbreak
hPa	hectopascal
MIZ	Marginal Ice Zone
OML	Oceanic Mixed Layer
SST	Sea Surface Temperature

1 Introduction

The most intense heat fluxes in the high latitudes occur during marine cold air outbreaks (CAOs, figure 1.1), which account for up to 80% of the heat loss in the regions of deep water formation (figure 1.2) (Papritz and Spengler, 2017). As cold and dry air is being advected off the sea ice over open water, the turbulent heat fluxes can be as large as 700 W/m^2 (Brümmer, 1996a), which is similar to the heat fluxes observed during ocean convection (Moore et al., 2008). CAOs are the main drivers of heat and moisture fluxes in the Nordic Seas and thus likely contribute to deep water formation (Våge et al., 2015; Eldevik et al., 2009). Papritz and Spengler (2017) in fact concluded that the deepening of the oceanic mixed layer in the Nordic Seas might result from a few intermittent but intense CAOs and not continuous heat losses during weak CAOs.

However, exactly where and how the water-mass transformation occur remain unclear, as well as the role of individual CAOs. That the deepest mixed layer in the Iceland Sea is found in the outskirts of the cyclonic gyre (Våge et al., 2015), rather than in the middle where the ocean stratification is weakest (Marshall and Schott, 1999), does indicate that CAOs are important. The location of the deepest mixed layer in the Iceland Sea is also where the heat fluxes are strongest (Våge et al., 2015). The turbulent heat fluxes are thought to be most important for deep convection in the Iceland and Greenland Sea (Brakstad et al., 2018), and if CAOs are indeed important for ocean convection, a change in frequency of occurrence might have profound impact on the climate on the large scale as convection in the Nordic Seas is an important source of the Atlantic Meridional Overturning Circulation (AMOC). We therefore want to assess the individual contribution of a CAO event on the oceanic mixed layer.

The turbulent heat fluxes are important for deep ocean convection, and the changing sea ice in the Arctic might change both the distribution of the turbulent heat fluxes, and the location of the maximum fluxes. The maximum turbulent heat fluxes are found just off the sea ice edge where the air is both dry and cold (Papritz and Sodemann, 2018). Furthermore, the width of the transition zone between fast ice and open affects the distribution of the heat fluxes (Våge et al., 2015). This transition zone is called the marginal ice zone (MIZ). Whereas a narrow MIZ is characterized by a steep gradient in the turbulent heat fluxes, a broad MIZ gives stronger heat fluxes over a much larger area (Våge et al., 2015). The MIZ has narrowed between 1979 and

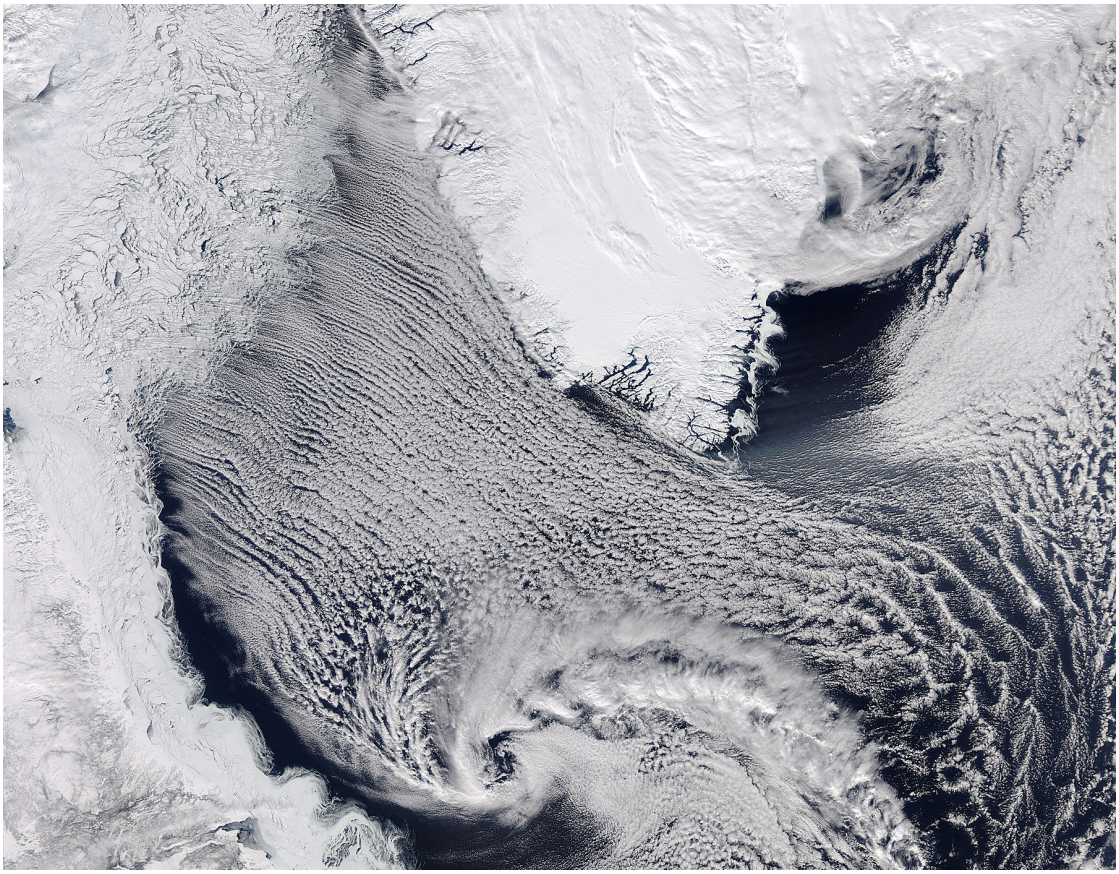

Figure 1.1: Satellite picture of CAO over the Labrador Sea 26 March 2014 captured by NASA. Available from `https://polarlows.files.wordpress.com/2014/04/image04062014_1km.jpg`, accessed June 3, 2019. The cloud streets are clearly visible and so is the polar low that is associated with the CAO.

2010 (Strong, 2012), and the sea ice edge in the Greenland and Iceland Sea is retreating (Moore et al., 2015). The decrease of sea ice might be associated with the observed decrease in ocean convection in the Iceland and Greenland Sea (Moore et al., 2015). We expect the sea ice to change further due to climate change, but the impact is uncertain as the climate models struggle to represent the MIZ due to its high variability and sharp gradients (Pagowski and Moore, 2001; Bourassa et al., 2013). This might lead to inaccurate energy exchange between the ocean and the atmosphere, which could cause uncertainties in climate predictions through changes in AMOC.

To study the ABL characteristics during CAOs, Chechin et al. (2013) used a non-hydrostatic 2-D mesoscale dry atmospheric model. Of particular interest was the effect of the spatial horizontal resolution upon sharp gradients in sea ice concentration. Using a coarse resolution equivalent to what is used in climate models (60 km), the maximum heat fluxes were underestimated by about 15% close to the sea ice edge in the coarse resolution run, which might have a profound

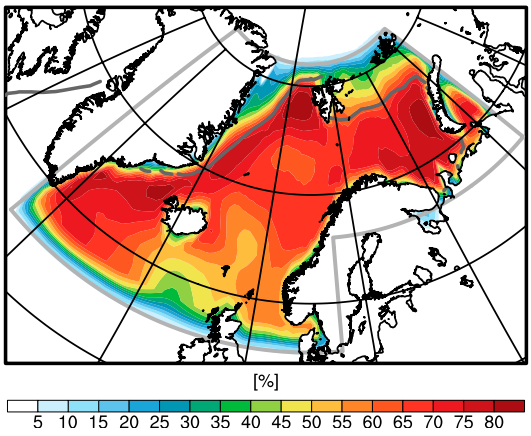

Figure 1.2: Percentage of positive surface turbulent heat flux associated with CAO trajectories for all trajectories in the Nordic Seas. The mean sea ice boundary 50% concentration is shown in dark grey contour. From Papritz and Spengler (2017)

impact on the mixed layer depth of the ocean. However, the sea surface temperature (SST) was assumed constant, and the coupling to the ocean might reduce the heat fluxes also further downstream.

If the SST is allowed to respond to the heat fluxes, the heat fluxes might decrease as they cool the ocean and hence decrease the air-sea temperature difference. Li (2002) and Xue et al. (2002) showed that heat fluxes associated with cyclones over the Gulf Stream were 10% lower in the coupled experiment compared to the uncoupled. On the other hand, Chao (1992) concluded that for time scales of less than a week, and assuming constant SST seems to be a reasonable approximation for CAOs over the Gulf Stream in a dry model. However, Chao (1992) did not take into account the latent heat flux, which tends to dominate over the sensible heat flux above the warm waters of the Gulf Stream. As a result, the coupling might be more important than what the study suggests.

Even though CAOs are crucial for the heat exchange at high latitudes, little is known about the sensitivity to latent heating in the atmosphere and the coupling to the ocean. Furthermore, simulations of CAOs with numerical weather prediction models rely heavily on subgrid scale processes due to the highly diabatic nature of CAOs (Papritz and Sodemann, 2018) and hence parameterizations. Parameterizations in climate models have been developed for regions with vastly different thermodynamic properties than the Arctic atmosphere (Curry et al., 1996). Therefore, a better understanding of the processes during CAOs are important, thereby also assess how parameterizations can influence the evolution of CAOs.

Such a parameterized quantity is the precipitation, which is difficult to measure during field campaigns and therefore associated with large uncertainties. During field campaigns it is either calculated as a residual or simply ignored (Hartmann et al., 1997; Brümmer, 1996b). As the air flows off the sea ice, the high fluxes transform the cold and stably stratified polar air mass into a warmer and more humid air mass that is often associated with precipitation downstream (Papritz and Sodemann, 2018). Papritz and Sodemann (2018) argued recently that precipitation during CAOs contributes to a substantial fraction of the freshwater balance in the Nordic Seas. However, most of the moisture that precipitates during a CAO has been evaporated during the same CAO. Nonetheless, the redistribution of freshwater might be important and could potentially trigger ocean convection in one place while inhibiting it in another. We therefore aim to quantify the role of precipitation in changing the ocean stratification and its impact on the heat exchange during CAOs.

Given the important role of the heat exchange during CAOs, the uncertainty of the effect of the coupling, moisture, biases in sea ice distribution in climate models, and the sharp gradients of the MIZ combined with a climate models' coarse resolution calls for a closer investigation to try to quantify their effect on air-sea heat exchange. To approach these issues, we develop two mixed layer models, the first representing the atmospheric boundary layer (ABL) and the second the ocean mixed layer (OML) and couple them. The ABL model includes moisture, and hence latent heating and precipitation. Both the latent heat flux and the precipitation impact the heat and freshwater content in the OML, which are accounted for in the model. The MIZ can also be represented by varying a static sea ice distribution.

Mixed layer models have been used to investigate the atmospheric response to CAOs previously, but few of them have included moisture (e.g. Renfrew and King, 2000). Furthermore, those who have, have not included precipitation (e.g. Stage and Businger, 1981; Økland, 1983). In contrast, several mixed layer models of the ocean exists and most of them more complicated than what presented here (Price et al., 1986; Niiler and Kraus, 1977; Stevens, 2007). However, none of them has been coupled to a mixed layer model of the atmosphere. When we couple the two mixed layer models, we are able to maintain a minimum complexity with respect to the problem at hand. Furthermore, the simplistic nature of the model makes it possible to quantify the processes' relative contributions and hence gain more knowledge of the important processes during CAOs. We take advantage of the computational efficiency and perform a wide range of sensitivity tests that we will explore here.

In summary, we use a novel coupled atmosphere-ocean mixed layer model to address the following questions:

- Is the mixed layer model able to realistically represent the ABL structure during CAOs?
- How does moisture affect ABL characteristics?

- Does the coupling between the atmosphere and the ocean impact the fluxes and the structure of the ABL, and what is the effect of ocean stratification?
- How does the distribution of sea ice affect the structure of the ABL through coupling?

2 Model description

In this chapter we derive the model equations for both the ABL and the OML, and outline the approximations used to solve the equations, followed by a description of the model initialization.

2.1 Moist atmosphere mixed layer model

A mixed layer model assumes that variables are constant with height within the mixed layer with a discontinuity aloft. Renfrew and King (2000) developed a convective internal boundary layer model that successfully represented flow evolution during cold air outbreaks. Their model is based on the dry thermodynamic equation and explains how the mixed layer potential temperature and boundary layer height change with fetch.

However, when including moisture one needs to accommodate for phase changes in addition. This means that potential temperature is no longer a conserved quantity and one usually resorts to liquid water potential temperature (θ_l) or equivalent potential temperature (θ_e). One advantage of θ_l over θ_e is that θ_l reverts directly to the thermodynamic value of interest, θ, for unsaturated air (Deardorff, 1976a).

The liquid water potential temperature and total mixing ratio in the atmosphere are given by

$$\theta_l = \theta - \frac{L_v \theta}{c_p T} q_l \quad \text{and} \tag{2.1}$$

$$q = q_v + q_l \ , \tag{2.2}$$

where the liquid water potential temperature is the potential temperature a parcel would attain if all the liquid water in the air parcel evaporated. The last term on the rhs in (2.1) accommo-

dates for the phase changes, where L_v is the latent heat of vaporization and c_p the specific heat capacity of the air, and q_l is the liquid water. q is the total mixing ratio and consists of water vapour q_v and liquid water.

The setup of the atmospheric part of the model is shown in figure 2.1. The air column with an initial temperature and humidity is advected over a warmer water surface by the wind. This causes air-sea heat exchange through turbulent fluxes from below, as well as and entrainment from the layer above. These processes modify both the temperature and mixing ratio in the boundary layer and lead to an increase of the boundary layer height. If the air moistens sufficiently, condensation will occur within the boundary layer, forming a cloud layer. This release latent heat, which warms the air within the cloud layer. The inversion layer is assumed to be infinitesimally thin, such that there is a discontinuity in both temperature and humidity at the top of the ABL. Previous studies using mixed layer models have shown that the errors resulting from such an approximation are negligible (Pelly and Belcher, 2001). For simplification, we neglect all the radiative effects, which in the presence of a cloud would act to both heat the ABL and increase the entrainment rate (Stage and Businger, 1981).

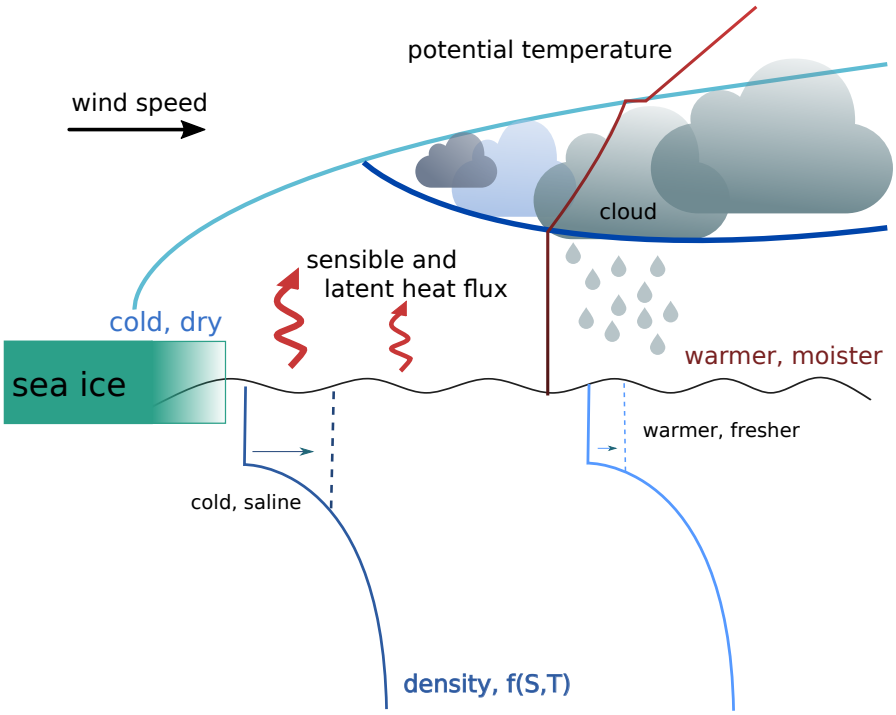

Figure 2.1: Schematic showing the setup of the model, with cold and dry air being advected over the relatively warmer ocean.

2.1.1 Derivation of the atmopsheric mixed layer model

Liquid water potential temperature

We start from the thermodynamic equation for liquid water potential temperature, θ_l,

$$\frac{D\theta_l}{Dt} = \frac{\partial\theta_l}{\partial t} + u\frac{\partial\theta_l}{\partial x} + v\frac{\partial\theta_l}{\partial y} + w\frac{\partial\theta_l}{\partial z} = \nu\nabla^2\theta_l + \dot{\theta}_l, \tag{2.3}$$

which states that the total rate of change of θ_l can be due to molecular viscosity (first term on the rhs) and external heating or changes in liquid water content (last term on the rhs). Note that internal heating processes associated with phase changes from vapour to liquid are included in the definition of θ_l.

In reasonably shallow boundary layers, density in the mixed layer is assumed to be constant, together with incompressibility, $\nabla \cdot \vec{v} = 0$ (Stull, 1997). We can then rewrite (2.3) in flux form

$$\frac{\partial\theta_l}{\partial t} + \frac{\partial u\theta_l}{\partial x} + \frac{\partial v\theta_l}{\partial y} + \frac{\partial w\theta_l}{\partial z} = \nu\nabla^2\theta_l + \dot{\theta}_l. \tag{2.4}$$

We assume the viscosity term to be small and will henceforth neglect it. Applying Reynolds averaging yields

$$\frac{\partial\overline{\theta_l}}{\partial t} + \frac{\partial\bar{u}\bar{\theta_l}}{\partial x} + \frac{\partial\overline{u'\theta_l'}}{\partial x} + \frac{\partial\bar{v}\bar{\theta_l}}{\partial y} + \frac{\partial\overline{v'\theta_l'}}{\partial y} + \frac{\partial\bar{w}\bar{\theta_l}}{\partial z} + \frac{\partial\overline{w'\theta_l'}}{\partial z} = \bar{\dot{\theta}}_l, \tag{2.5}$$

where quantities with a bar on top are the Reynold's averaged quantities and the primed quantities are variations within the given space and time scales of the Reynold's average.

We assume two-dimensionality $\frac{\partial}{\partial y} = 0$ and steady state $\frac{\partial}{\partial t} = 0$, as well as horizontally homogeneous turbulence $\frac{\partial\overline{u'\theta_l'}}{\partial x} = 0$. Thus, (2.5) becomes

$$\frac{\partial\bar{u}\bar{\theta_l}}{\partial x} = -\frac{\partial\bar{w}\bar{\theta_l}}{\partial z} - \frac{\partial\overline{w'\theta_l'}}{\partial z} + \bar{\dot{\theta}}_l \ . \tag{2.6}$$

We assume $\bar{u}$ is constant within the ABL and integrate (2.6) over the mixed later depth h. As $h = h(x)$, we need to use Leibniz rule on the term on the lhs;

$$\int_0^{h(x)} \frac{\partial\bar{u}\bar{\theta_l}}{\partial x}dz = -\bar{u}\bar{\theta_l}|_{z=h}\frac{dh}{dx} + \frac{d}{dx}\left(\int_0^{h(x)} \bar{u}\bar{\theta}dz\right) \ . \tag{2.7}$$

We rewrite the last term on the rhs in (2.7) by taking the average of the function over the mixed layer. The average of a function is expressed as $\Psi_m = \frac{1}{a}\int_{z=0}^{z=a}\Psi dz$. This yields

$$\int_0^{h(x)} \frac{\partial\bar{u}\bar{\theta_l}}{\partial x}dz = -\bar{u}\bar{\theta_l}|_{z=h}\frac{dh}{dx} + \frac{d}{dx}\left(\bar{u}\theta_m h\right) \ . \tag{2.8}$$

We then use the product rule on the last term in (2.8)

$$\int_0^{h(x)} \frac{\partial\bar{u}\bar{\theta_l}}{\partial x}dz = -\bar{u}\bar{\theta_l}|_{z=h}\frac{dh}{dx} + h\frac{d}{dx}\left(\bar{u}\theta_m\right) + \theta_m\frac{d}{dx}\left(\bar{u}h\right) \ , \tag{2.9}$$

and assume that the quantities atop of the mixed layer are equal to the mean in the mixed layer, such that the first and the last term on rhs cancel each other out. Note that the total derivates in (2.9) can be replaced by partial derivatives. Using (2.9) in (2.6), the integrated and averaged equation over the mixed layer depth then reads

$$\frac{\partial \bar{u}\theta_{lm}}{\partial x} = -\frac{1}{h}\left(\overline{w'\theta'_l}|_{z=h} - \overline{w'\theta'_l}|_{z=0}\right) \ , \tag{2.10}$$

where we assumed that the mean vertical velocity at the top and bottom of the mixed layer vanish, and neither external heating nor internal sources of q_l within the mixed layer that are not associated with phase changes, because these are already included in the formulation of θ_l.

To solve (2.10), the fluxes at the top and the bottom of the mixed layer have to be parameterized. As the flux of liquid water potential temperature can be separated into a flux of potential temperature and liquid water

$$\overline{w'\theta'_l}\Big|_{z=0,h} \approx \overline{w'(\theta' - \frac{L_v\overline{\theta}}{c_p\overline{T}}q'_l)}\Big|_{z=0,h} = \overline{w'\theta'}\big|_{z=0,h} - \frac{L_v\overline{\theta}}{c_p\overline{T}}\overline{w'q'_l}\Big|_{z=0,h} \ , \tag{2.11}$$

we parameterize the fluxes at the top and bottom as

$$\overline{w'\theta'_l}|_{z=h} = -w_e\left(\Delta\overline{\theta} - \frac{L_v\overline{\theta}}{c_p\overline{T}}\Delta q_l\right) \quad \text{and} \tag{2.12}$$

$$\overline{w'\theta'_l}|_{z=0} = c_H\overline{u}\left(\overline{\theta}_{SST} - \overline{\theta}\right) - \frac{L_v}{c_p}P \ . \tag{2.13}$$

For the flux through the surface, (2.13), we use a standard bulk flux parameterization, $\rho c_p\ \overline{w'\theta'}\big|_{z=0} = Q_h = \rho c_p c_H \overline{u}(\overline{\theta}_{SST} - \overline{\theta})$. c_H is the transfer coefficient for sensible heat, and c_p is the specific heat capacity. $\bar{\theta}$ is the potential temperature at the surface, while θ_{SST} is the sea surface potential temperature. Note that while θ_l is constant throughout the mixed layer, θ is a function of z when water in the liquid phase is present. The second term on rhs in (2.13) accounts for the surface flux of liquid water, where P is the precipitation, defined as the negative liquid water flux through the surface. We neglected the effect of sea spray as an upward flux of liquid water and assumed that $\frac{\theta}{T} \approx 1$.

The flux at the top of the mixed layer in (2.12) represents entrainment, where w_e is the entrainment velocity and $\Delta\theta$ and Δq_l are the temperature and liquid water mixing ratio discontinuities at the top of the mixed layer, respectively. The most straightforward way of parameterizing the entrainment velocity w_e is to assume that the flux at the top of the boundary layer is proportional to the surface flux by a constant fraction Υ such that the flux at the top of the mixed layer can be written as;

$$\overline{w'\theta'}|_{z=h} = -\Upsilon\overline{w'\theta'}|_{z=0} \ . \tag{2.14}$$

We formulate the flux of potential temperature similar to (2.12), and combining this expression with (2.14) yields an expression for the entrainment velocity, w_e;

$$w_e = \Upsilon \frac{\overline{w'\theta'}|_{z=0}}{\Delta\theta} \ , \tag{2.15}$$

where $\Upsilon = 0.2$ is appropriate for a convective atmospheric boundary layers, (Stull, 1997).

The jump in potential temperature can be written as

$$\Delta\theta = \theta^b - \theta \ , \tag{2.16}$$

where $\theta^b = \gamma_\theta z + \theta_0$ is the background potential temperature profile, with θ_0, the background temperature at $x, z = 0$, and γ_θ, the background potential temperature lapse rate. Written in terms of liquid water potential temperature as defined in (2.1), (2.16) can be expressed as

$$\Delta\theta = \gamma_\theta h + \theta_0 - \theta_{lm} - \frac{L_v \overline{\theta}}{c_p \overline{T}} q_{l_{z=h}} \ . \tag{2.17}$$

To find the jump in liquid water mixing ratio, we assume that the background atmosphere is dry, $q_l^b = 0$, such that Δq_l can be written as;

$$\Delta q_l = q^b_{z=h} - q_{l_{z=h}} = -q_{l_{z=h}}, \tag{2.18}$$

We combine (2.17) with (2.18) in to the rhs in (2.12):

$$w_e \left(\Delta\theta - \frac{L_v \theta}{c_p T} \Delta q_l \right) = w_e \left(\gamma_\theta h + \theta_0 - \theta_{lm} \right) \ . \tag{2.19}$$

Using (2.19) and (2.13) in (2.10) yields the mixed layer liquid water potential temperature equation

$$\boxed{\frac{\partial \theta_{lm}}{\partial x} = \frac{w_e}{h\overline{u}} \left(\gamma_\theta h + \theta_0 - \theta_{lm} \right) + \frac{c_H \left(\overline{\theta}_{SST} - \overline{\theta} \right)}{h} - \frac{L_v \overline{\theta}}{c_p \overline{T} h \overline{u}} P} \ . \tag{2.20}$$

Boundary layer height and the discontinuity in potential temperature

To obtain an equation for the boundary layer height, we take the total derivative of (2.16) and assume steady state and two-dimensionality as before. Doing this yields

$$\frac{\partial \Delta\theta}{\partial x} = \gamma_\theta \frac{\partial h}{\partial x} - \frac{\partial \theta}{\partial x} \ . \tag{2.21}$$

It is important to note that in contrast to θ_{lm} which is well-mixed throughout the ABL, θ is a function of z. When phase changes occur, latent heat is released and θ will be changed internally in the mixed layer.

According to, e.g., Garratt (1992), assuming a zero-order jump in θ also means assuming that

$$\overline{w'\theta'}|_{z=h} = -\Delta\theta \bar{u} \frac{\partial h}{\partial x} \ . \tag{2.22}$$

Combining (2.21), (2.22) and (2.14) yields an expression for the discontinuity in potential temperature at the top of the boundary layer

$$\boxed{\frac{\partial \Delta\theta}{\partial x} = \left(\frac{\Upsilon \overline{w'\theta'}|_{z=0}}{\bar{u}\Delta\theta} \gamma_\theta - \frac{\partial \theta}{\partial x}\Big|_{z=h} \right)} \ . \tag{2.23}$$

(2.23) can be integrated and solved for $\Delta\theta$. The expression for $\Delta\theta$ can then be inserted into (2.21) to yield an expression for h;

$$\boxed{h = \frac{1}{\gamma_\theta} \left(\Delta\theta - \theta_0 + \theta|_{z=h} \right)} \ . \tag{2.24}$$

When $\Upsilon = 0$, the flux at the top of the boundary layer is zero. From (2.23), this can either be achieved by $\Delta\theta = 0$ or $\frac{\partial h}{\partial x} = 0$. However, as the boundary layer height growth can not be zero, we have to demand $\Delta\theta$ to be zero. Then (2.24) reduces to $h = 1/\gamma_\theta(\theta|_{z=h} - \theta_0)$

Mixing ratio

The derivation for the evolution of the total mixing ratio q is similar to the derivation for θ_l. The equivalent to equation (2.5) for the total mixing ratio is

$$\frac{\partial \bar{q}}{\partial t} + \frac{\partial \bar{u}\bar{q}}{\partial x} + \frac{\partial \overline{u'q'}}{\partial x} + \frac{\partial \bar{v}\bar{q}}{\partial y} + \frac{\partial \overline{v'q'}}{\partial y} + \frac{\partial \bar{w}\bar{q}}{\partial z} + \frac{\partial \overline{w'q'}}{\partial z} = \bar{\dot{q}} \ , \tag{2.25}$$

where $\bar{\dot{q}}$ is local losses and gains due to falling precipitation. Assuming steady state $\frac{\partial}{\partial t} = 0$, two-dimensionality $\frac{\partial}{\partial y} = 0$, and horizontal homogeneity $\frac{\partial \overline{u'q'}}{\partial x} = 0$, (2.25) reduces to

$$\frac{\partial \bar{u}\bar{q}}{\partial x} = -\frac{\partial \bar{w}\bar{q}}{\partial z} - \frac{\partial \overline{w'q'}}{\partial z} - \bar{\dot{q}} \ . \tag{2.26}$$

Integrating (2.26) over mixed layer depth and assuming the mean vertical velocity at the top and bottom of the mixed layer vanish, that there are no external sources of q, and applying the Leibniz' rule:

$$h\left(\frac{\partial \bar{u}\bar{q}}{\partial x}\right) = -(\bar{u}\bar{q})_{z=h}\frac{\partial h}{\partial x} + q_m \frac{\partial \bar{u}h}{\partial x} - \overline{w'q'}|_{z=h} + \overline{w'q'}|_{z=0} \ . \tag{2.27}$$

As the moisture flux consists of both vapour and liquid (see (2.2)), the flux can be separated

$$\overline{w'q'} = \overline{w'q'_v} + \overline{w'q'_l} \ . \tag{2.28}$$

Using (2.28) in (2.27), assuming that $q_{z=h} = q_m$, yields

$$h\bar{u}\frac{\partial \bar{q_m}}{\partial x} = -\overline{w'q'_v}|_{z=h} - \overline{w'q'_l}|_{z=h} + \overline{w'q'_v}|_{z=0} + \overline{w'q'_l}|_{z=0} \ . \tag{2.29}$$

The moisture fluxes can be expressed as

$$\overline{w'q'_l}|_{z=0} = P \ , \tag{2.30}$$

$$\overline{w'q'_v}|_{z=0} = c_E \bar{u}\,(q_{sw} - q_v) \quad \text{and} \tag{2.31}$$

$$\overline{w'q'_l}|_{z=h} + \overline{w'q'_v}|_{z=h} = \overline{w'q'}|_{z=h} = w_e \Delta q_m \ , \tag{2.32}$$

where (2.30) represents the liquid water flux through the surface, which is equal to the precipitation P, as we neglect the effect of sea spray. (2.31) states that the flux of water vapour through the surface is proportional to the latent heat flux, $Q_E = \rho L_v c_E \bar{u}(q_{sw} - q_m) = \rho L_v \overline{w'q'_v}$, where c_E is the transfer coefficient for moisture and L_v is the latent heat of vaporization. q_{sw} is 98% of the saturated mixing ratio at sea surface temperature. The factor 98% accounts for the effect of salinity (Talley, 2011, pp. 132). (2.32) represents the entrainment through the top of the mixed layer, which is proportional to the jump in total mixing ratio and the entrainment velocity.

$$\Delta q_m = \Delta q_v + \Delta q_l = -q_v - q_l = -q_m \tag{2.33}$$

where we assumed a dry background state as before. Inserting (2.30), (2.31), and (2.32) into (2.29) yields

$$\boxed{\frac{\partial q_m}{\partial x} = -\frac{w_e}{h\bar{u}} q_m + \frac{c_E\,(q_{sw} - q_v)}{h} - \frac{1}{h\bar{u}} P} \ . \tag{2.34}$$

2.1.2 Vertical distribution of moisture

To find the boundary layer height and the jump in potential temperature, it is necessary to know the vertical distribution of liquid water in the ABL. We derive this distribution by first finding the cloud base height. To find the cloud base height, we assume a dry adiabatic lapse rate beneath the cloud. Knowing the temperature profile allows us to calculate the saturation mixing ratio, q_s, beneath the cloud, and check where $q_m > q_s$. The level where $q_m > q_s$ is where condensation occurs. If this level is within the boundary layer, it is defined as the cloud base height.

The vertical gradient of the saturation mixing ratio, q_s, below the cloud layer is determined for dry-adiabatic conditions using the Clausis-Clapeyron equation. The Clausis-Clapeyron equation for water vapour pressure saturated over a plane surface, applicable to droplets large enough to neglect the curvature effect is

$$\frac{1}{e_s}\frac{de_s}{dT} = \frac{L_v}{R_v T} \ , \tag{2.35}$$

where e_s denote the saturation vapour pressure. Following Khvorostyanov and Curry (2014) chapter 3.7, (2.35) can be rewritten using the chain rule

$$\frac{de_s}{dz} = \frac{de_s}{dT}\frac{dT}{dz} \ . \tag{2.36}$$

We insert (2.36) in (2.35) and rearrange to yield

$$\frac{de_s}{dz} = e_s \frac{L_v}{R_v T^2}\frac{dT}{dz} \quad , \tag{2.37}$$

where R_v is the ideal gas constant for water vapour. (2.37) is written in terms of saturation vapour pressure, but to relate it to one of the model parameters, we convert it to water vapour saturation mixing ratio, q_s. The conversion is given as

$$e_s = \frac{pq_s}{\epsilon} \ , \tag{2.38}$$

where ϵ is the ratio $R_d/R_v = 0.622$, and R_d is the ideal gas constant for dry air. Inserting (2.38) into (2.37) yields

$$\frac{d(pq_s)}{dz} = \epsilon \frac{g}{c_p}\frac{pq_s}{\epsilon}\frac{L_v}{R_v T^2}\frac{dT}{dz} \ , \tag{2.39}$$

which can be rewritten as

$$\frac{dq_s}{dz} = q_s\left(\frac{dT}{dz}\frac{L_v}{R_v T^2} - \frac{1}{p}\frac{dp}{dz}\right) \ . \tag{2.40}$$

Using hydrostatic balance and the ideal gas law, the last term can be rewritten as

$$\frac{dp}{dz} = -\rho g = -\frac{p_d}{R_d T} g - \frac{e}{R_v T} g \ . \tag{2.41}$$

The last term can be neglected as $e \ll p_d$. We use (2.41) in (2.40)

$$\frac{dq_s}{dz} = q_s \left(\frac{dT}{dz} \frac{L_v}{R_v T^2} + \frac{g}{R_d T} \right) \tag{2.42}$$

We assume dry adiabatic conditions below the cloud base, such that $\frac{dT}{dz}$ in (2.42) can be rewritten to $-g/c_p$. Rewriting (2.42) yields

$$\boxed{\frac{dq_s}{dz} = -\frac{g}{R_d T} \left(\frac{L_v}{c_p T} \frac{R_d}{R_v} - 1 \right) q_s} \tag{2.43}$$

If the cloud base height is lower than the boundary layer height, such that $q_m > q_s(z)$ for $z < h$, then saturation is reached within the ABL. This means θ is no longer constant throughout the ABL. However, we need to know the temperature within the cloud layer to calculate the saturation mixing ratio and hence the liquid water content and precipitation. To find the vertical distribution of moisture in the cloud layer, we assume the temperature to follow the moist adiabat. Following Khvorostyanov and Curry (2014) chapter 3.11, it follows from the first law of thermodynamics that

$$c_p dT + L_v dq_s - v dp = 0 \ . \tag{2.44}$$

which accounts for the effect of latent heating in the second term. The last term in (2.44) can be rewritten with the use of the ideal gas law and hydrostatic balance;

$$c_p dT + L_v dq_s + g dz = 0 \ . \tag{2.45}$$

We divide (2.45) by $c_p dz$ and using the proper notation for the wet and dry adiabatic gradient, γ_w and γ_a, respectively, and solve for dT/dz

$$\gamma_w = -\frac{dT}{dz} = \gamma_a + \frac{L_v}{c_p} \frac{dq_s}{dz} \ . \tag{2.46}$$

Using (2.42) in (2.46) yields the equation

$$\gamma_w = \gamma_a - \frac{L_v}{c_p} q_s \left(\gamma_w \frac{L_v}{R_v T^2} - \frac{g}{R_d T} \right) \ , \tag{2.47}$$

which can be solved for γ_w;

$$\gamma_w = \gamma_a \frac{1 + \frac{L_v}{R_d T} q_s}{1 + \frac{L_v^2}{c_p R_v T^2} q_s} \ . \tag{2.48}$$

The numerator in (2.48) is close to one; such that the equation approximately can be written as:

$$\gamma_w \approx \gamma_a \frac{1}{1 + \frac{L_v}{c_p}\frac{dq_s}{dT}} = \frac{\gamma_a}{\Gamma_1}, \tag{2.49}$$

where

$$\Gamma_1 = 1 + \frac{L_v}{c_p}\frac{dq_s}{dT} = 1 + \frac{L_v^2}{c_p R_v T^2} q_s \quad . \tag{2.50}$$

To find the potential temperature from the liquid water potential temperature (see (2.1)), we calculate the temperature within the cloud layer. The density is assumed to be constant throughout the mixed layer, which allows us to also find the pressure by assuming hydrostatic balance. With pressure and temperature, we determine q_s throughout the cloud, which allows us to calculate $q_l = q_m - q_s$.

Calculation of saturation mixing ratio

However, in order to use (2.43), we need boundary conditions on q_s. We could integrate (2.35) directly, but that requires boundary conditions, and L_v is a function of temperature. A common approximation for this integral is $e_s(T) = e^{21.653 - \frac{5420}{T}}$, where T is in Kelvin. Another approach is to approximate the saturation vapour pressure with a polynomial, which is what we do here. We find the saturation mixing ratio based on Lowe and Ficke (1974), which was developed for being both computationally efficient and accurate. They showed that sixth order polynomials for both ice and liquid water reference gave errors of less than 1%. The polynomial formulation for saturation vapour pressure is

$$e_s = a_0 + T(a_1 + (T(a_2 + T(a_3 + T(a_4 + T(a_5 + a_6 T)))))) \tag{2.51}$$

where T is the temperature in °C

Table 2.1: The polynomial constants for calculating saturation vapour pressure. From Lowe and Ficke (1974)

For water	For ice
$a_0 = 6.107799961$	$a_0 = 6.109177956$
$a_1 = 4.436518521 \times 10^{-1}$	$a_1 = 5.034698970 \times 10^{-1}$
$a_2 = 1.428945805 \times 10^{-2}$	$a_2 = 1.886013408 \times 10^{-2}$
$a_3 = 2.650648471 \times 10^{-4}$	$a_3 = 4.176223716 \times 10^{-4}$
$a_4 = 3.031240396 \times 10^{-6}$	$a_4 = 5.824720280 \times 10^{-6}$
$a_5 = 2.034080948 \times 10^{-8}$	$a_5 = 4.838803174 \times 10^{-8}$
$a_6 = 6.136820929 \times 10^{-11}$	$a_6 = 1.838826904 \times 10^{-10}$

To compute the saturation vapour pressure, we evaluate the polynomial at T. We convert it to saturation mixing ratio with (2.38). q_s is valid at the cloud base. Knowing q_s at the cloud base allows us to calculate the gradient with (2.43).

Precipitation

As liquid water cannot be accumulated ad libitum, the model needs to allow for precipitation, which needs to be parameterized. One way of doing this is to assume that a transition between cloud water, q_l to rainwater can be described as a Kessler-like autoconversion type. Autoconversion is the process where cloud droplets collide and coalesce. This relationship can, according to, e.g., Stensrud (2011), be described as

$$q_p(z) = max[k_1(q_l(z) - q_l^p), 0] \tag{2.52}$$

where k_1 is a conversion rate and q_p^p is a threshold value for q_l (Stensrud, 2011). Below this threshold value, autoconversion does not happen. The standard values for the threshold value is $q_l^p = 0.0005$ kg kg^{-1} and the autoconversion rate is $k_1 = 0.001$ s^{-1} (Stensrud, 2011). q_p can be referred to as precipitation production, and is a function of z. To get the total precipitation forming in the cloud, we integrate (2.52) over the cloud depth. The precipitation forming is assumed to precipitate out immediately after formation, and there is no evaporation beneath the cloud base.

To get the precipitation rates more consistent with observations, we increase the autoconversion rate to $k_1 = 0.002$ s^{-1} and neglect the threshold value (figure 2.2). The largest effect comes from neglecting the threshold. Increasing the precipitation efficiency further increases the precipitation rate. The largest precipitation rate is still low compared to the estimates from Papritz and Sodemann (2018) for a vigorous CAO.

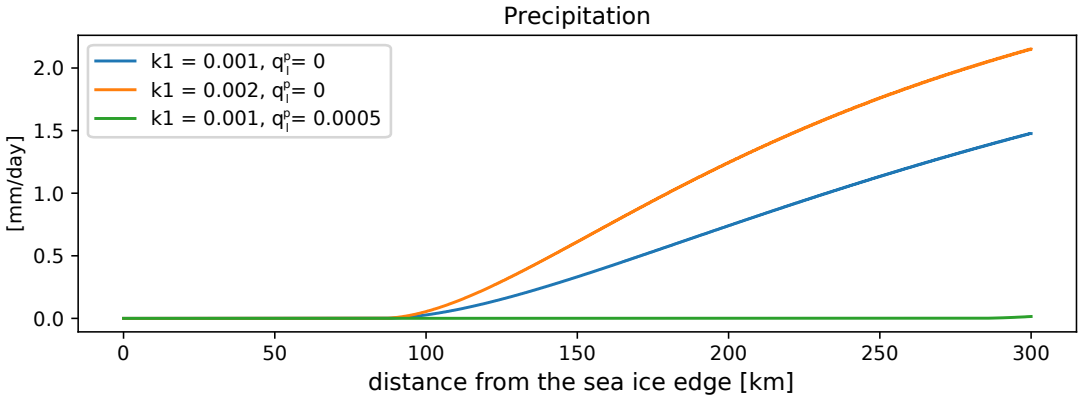

Figure 2.2: Precipitation with the different efficiencies, k_1 ([s^{-1}]), and threshold values q_l^p ([g/kg])

2.2 Ocean mixed layer model

The mixed layer model of the ocean consists of equations for temperature and salinity and a diagnostic equation for the mixed layer depth. The ocean mixed layer obtains a steady state by relaxation toward a predefined temperature and salinity profile.

The ocean cools through both sensible and latent heat fluxes if moisture is included in the ABL model. If the model is dry, the ocean will only cool through the sensible heat flux. In addition to changing the temperature, evaporation also increases the salinity of the mixed layer. Both the decreasing temperature and increasing salinity acts to make the mixed layer denser. If the mixed layer density becomes denser than the underlying layer, mixing occurs down to the depth where stability is restored.

We initialize our model with an idealized profile based on the NOAA-climatology for the Arctic (Boyer et al., 2015)[1]. We make it smooth by fitting it to an arctan-function, such that the gradient of the pycnocline, salinity in the upper layer, and the deep ocean are well represented. Any finer structures are removed, leaving only the main features of the structure in the ocean (e.g. figure 3.2).

2.2.1 Temperature

To end up with an equation for the temperature in the mixed layer, we start with the energy equation (e.g. Cushman-Roisin and Beckers (2011))

$$\rho C_p \frac{DT}{Dt} = k_T \nabla^2 T \ , \tag{2.53}$$

where k_T is the coefficient for heat diffusivity, ρ is the ocean density and C_p the heat capacity of the ocean. To obtain steady state in the ocean without advection, we introduce a Newtonian relaxation term to keep the ocean from cooling infinitely,

$$\frac{DT}{Dt} = \kappa_T \nabla^2 T + \frac{T_r - T}{\tau} \ . \tag{2.54}$$

In (2.54), τ is a Newtonian relaxation time scale and T_r is a reference temperature which the ocean is relaxed towards. Furthermore, the ocean is close to incompressible, such that $\nabla \cdot \vec{U} = 0$. This allows us to write (2.54) in flux form;

$$\left(\frac{\partial T}{\partial t} + \frac{\partial UT}{\partial x} + \frac{\partial VT}{\partial y} + \frac{\partial WT}{\partial z} \right) = \kappa_T \nabla^2 T + \frac{T_r - T}{\tau} \ . \tag{2.55}$$

We assume the viscosity term to be small and neglect it. Applying Reynolds averaging yields

$$\left(\frac{\partial \overline{T}}{\partial t} + \frac{\partial \bar{U}\bar{T}}{\partial x} + \frac{\partial \overline{U'T'}}{\partial x} + \frac{\partial \bar{V}\bar{T}}{\partial y} + \frac{\partial \overline{V'T'}}{\partial y} + \frac{\partial \bar{W}\bar{T}}{\partial z} + \frac{\partial \overline{W'T'}}{\partial z} \right) = \frac{T_r - \overline{T}}{\tau} \ . \tag{2.56}$$

[1] Available from `https://www.nodc.noaa.gov/OC5/regional_climate/arctic/` June 3, 2019

We assume two-dimensionality, $\frac{\partial}{\partial y} = 0$; horizontal homogeneous turbulence, $\frac{\partial \overline{U'T'}}{\partial x} = 0$; and stationarity, $\frac{\partial}{\partial t} = 0$; such that (2.56) can be simplified to

$$\frac{\partial \bar{U}\bar{T}}{\partial x} + \frac{\partial \bar{W}\bar{T}}{\partial z} + \frac{\partial \overline{W'T'}}{\partial z} = \frac{T_r - \overline{T}}{\tau} \ . \tag{2.57}$$

We integrate this equation over the mixed layer depth H, and take the average with the same notation as introduced in section 2.1.1. This yields

$$H\left[\frac{\partial \bar{U}\bar{T}}{\partial x}\right] + \bar{W}\bar{T}|_{z=H} - \bar{W}\bar{T}|_{z=0} + \overline{W'T'}|_{z=H} - \overline{W'T'}|_{z=0} = H\left[\frac{T_r - \bar{T}}{\tau}\right] \ . \tag{2.58}$$

Assuming the mean vertical velocity to be zero at the top and the bottom of the mixed layer further simplifies the equation to

$$H\left[\frac{\partial \bar{U}\bar{T}}{\partial x}\right] + \overline{W'T'}|_{z=H} - \overline{W'T'}|_{z=0} = H\left[\frac{T_r - \bar{T}}{\tau}\right] \ . \tag{2.59}$$

The heat flux at the top and bottom of the boundary layer must be approximated;

$$\overline{W'T'}|_{z=H} = W_e \Delta T \ \text{ and} \tag{2.60}$$

$$\overline{W'T'}|_{z=0} = Q_0 \ , \tag{2.61}$$

where Q_0 is the heat flux from the ocean to the atmosphere and defined as negative when the ocean is loosing buoyancy:

$$Q_0 = \frac{-1}{\rho_0 C_p}[Q_h + Q_e] \ . \tag{2.62}$$

Q_h is the sensible heat lost to the atmosphere, whereas Q_e is the latent heat flux. ρ_0 is a reference density for seawater. Further, W_e is the entrainment velocity at the bottom of the mixed layer, and ΔT is the temperature jump between the bottom of the mixed layer and the top of the pycnocline. We parameterize W_e as Niiler and Kraus (1977), except we assume that mixing by shear is negligible. Then, W_e can be written as

$$W_e = \frac{-HnB_0}{\Delta B H} \ . \tag{2.63}$$

(2.63) is only valid when the buoyancy flux at the surface, B_0, is negative. n is a buoyancy dissipation parameter, set to 0.02 according to Niiler and Kraus (1977), and ΔB is the jump in buoyancy between the top of the pycnocline and the mixed layer. B_0 and ΔB are expressed as

$$B_0 = g[\alpha Q_0 + \beta F_s] \tag{2.64}$$

$$\Delta B = g[\alpha \Delta T + \beta \Delta S] \ , \tag{2.65}$$

where α is the thermal expansion coefficient of seawater and β the haline contraction coefficient. However, contrary to the atmosphere, we do not have any explicit expression for ΔT or ΔS. As the surface layer densifies due to sensible heat loss to the atmosphere and evaporation, the jump in buoyancy decreases. As this happens, W_e increases rapidly, leading to unrealistic high values of both temperature and salinity. To avoid these problems and the unrealistic solutions that occurs, we omit entrainment from the pycnocline into the bottom of the mixed layer and set $W_e = 0$. This issue thus remains as a task for future development of this model (see chapter 6).

As we set $W_e = 0$, the only process that acts on the ocean temperature is the loss of heat to the atmosphere through the surface. We use (2.62) together with the flux approximation (2.61) in (2.59) and further drop the square brackets with the subscript m to denote the average quantity in the mixed layer. This yields:

$$\frac{\partial \overline{U} T_m}{\partial x} + \frac{-Q_0}{H} = \frac{T_r - T_m}{\tau} \ . \tag{2.66}$$

For simplicity, we assume the ocean to be motionless, $\bar{U} = 0$. Solving (2.66) for T_m yields

$$\boxed{T_m = T_r + \frac{\tau Q_0}{H}} \ . \tag{2.67}$$

(2.67) shows how the mixed layer temperature, T_m deviates from the reference temperature, T_r, as a result of heat loss from the ocean, Q_0, that acts over a time scale τ over the mixed layer depth H.

2.2.2 Salinity

A similar derivation of that for temperature can be done for salinity. Conservation of salinity requires that (e.g. Cushman-Roisin and Beckers, 2011)

$$\frac{DS}{Dt} = k_S \nabla^2 S \tag{2.68}$$

where k_S is the coefficient for salt diffusion. Following the same derivation as with the temperature, the analog to equation (2.59) for salinity is

$$H\left[\frac{\partial \bar{U}\bar{S}}{\partial x}\right] + \overline{W'S'}|_{z=H} - \overline{W'S'}|_{z=0} = H\left[\frac{S_r - \bar{S}}{\tau}\right] \ . \tag{2.69}$$

We approximate the fluxes of salinity similar to the fluxes of temperature ((2.61) and (2.60));

$$\overline{W'S'}|_{z=H} = W_e \Delta S \text{ and} \tag{2.70}$$

$$\overline{W'S'}|_{z=0} = F_S \ . \tag{2.71}$$

ΔS in (2.70) is the jump in salinity between the mixed layer and the top of the pycnocline, and F_S is the salt flux into the ocean at the surface. To find an equation for F_S, we use the concept that changes in salinity is due to changes in the volume that salinity is distributed in, while the actual mass of salt remains constant;

$$m_T = m_S + m_W \tag{2.72}$$

which describes the total mass, m_T, is equal to the mass of salt, m_S, and the mass of water, m_w. The density of salt, ρ_s, is written as;

$$\rho_S = \frac{m_S}{V} \tag{2.73}$$

where V is the volume. To see changes in this density, we take the derivative:

$$\frac{d\rho_S}{dt} = \frac{1}{V}\frac{dm_S}{dt} - \frac{m_S}{V^2}\frac{dV}{dT} \ . \tag{2.74}$$

The first term on rhs in (2.74) is zero because there is no changes in the actual salt content, only in volume. We multiply (2.74) by $\frac{1}{\rho_T}$, and introduce the salinity S, defined as $\frac{\rho_S}{\rho_T}$, equivalent to $S = \frac{m_S}{m_T}$. With this (2.74) can be rewritten as

$$\frac{1}{\rho_T}\frac{d\rho_S}{dt} \approx \frac{dS}{dt} = -\frac{S}{V}\frac{dV}{dt} \ . \tag{2.75}$$

The change in volume can be expressed through the change in total mass;

$$\frac{dS}{dt} = -\frac{S}{m_T}\frac{dm_W}{dT} \tag{2.76}$$

where the derivative on the rhs in (2.76) reduces to just the change in the mass of the water as the mass of salinity is constant. We rewrite to a more familiar notation;

$$F_S = \frac{S(E-P)}{\rho} \ , \tag{2.77}$$

where E is evaporation, given by $c_E \bar{u}(q_{sw} - q_v)$, P is precipitation, ρ is the density of seawater, and S is the salinity in the mixed layer. Inserting the flux approximations, (2.70) and (2.71), in (2.69), dropping the square brackets to the subscript m and assuming that the ocean is motionless such that $\bar{U} = 0$, we can solve (2.69) for S to give an equation for the salinity in the mixed layer

$$\boxed{S_m = S_r + \frac{\tau F_S}{H}} \ . \tag{2.78}$$

(2.78) shows how the mixed layer salinity S_m deviates from the reference salinity S_r as a result of the salinity flux F_s that acts with a time scale τ over the mixed layer depth H.

2.2.3 Mixed layer depth

An increase in the mixed layer depth H can only occur through convective adjustment. We calculate the density of the mixed layer, with the equation of state

$$\rho = \rho(S, T, p) \ . \tag{2.79}$$

As the equation of state for the ocean is quite complicated and involves a thermal expansion coefficient and a haline contraction coefficients, which both depend on temperature and salinity, we use the EOS-80 seawater package for python to calculate the density (Fernandes, 2014)[2]. We assume the ocean to be incompressible, and hence the pressure does not affect the density calculations. For details about the density calculations, refer to Fofonoff and Millard Jr (1983).

If the density of the mixed layer is larger than the density in the pycnocline, the water column is unstable. Mixing occurs down to the depth where the stability of the water column is restored.

[2]https://pypi.org/project/seawater/. Accessed June 3, 2019

2.3 Model implementation

2.3.1 ABL

In order to implement the equations, we integrate the equations for the atmospheric boundary layer with fetch, and solve them numerically.

The equations for the ABL are repeated below, where we have introduced the convenient notation for the surface sensible heat flux and latent flux as Q_h and Q_e respectively, where $Q_h = \rho c_p c_H \overline{u} \left(\overline{\theta}_{SST} - \overline{\theta}\right)$ and $Q_e = \rho L_v c_E \overline{u} \left(q_{sw} - q_v\right)$;

$$\begin{aligned}
\frac{\partial \Delta\theta}{\partial x} &= \frac{\gamma_\theta \Upsilon Q_h}{\rho c_p \Delta\theta \bar{u}} - \left.\frac{\partial \theta}{\partial x}\right|_{z=h} \ , \\
\frac{\partial \theta_{lm}}{\partial x} &= \frac{\Upsilon Q_h}{\rho c_p \Delta\theta} \frac{1}{h\bar{u}} \left(\gamma_\theta h + \theta_0 - \theta_{lm}\right) + \frac{Q_h}{\rho c_p h \bar{u}} - \frac{L_v}{c_p h \bar{u}} P \ , \text{ and} \\
\frac{\partial q_m}{\partial x} &= \frac{\Upsilon Q_h}{\rho c_p \Delta\theta} \frac{1}{h\bar{u}} (q_m^b - q_m) + \frac{Q_e}{\rho L_v h \bar{u}} - \frac{1}{h\bar{u}} P \ .
\end{aligned}$$

q_m^b in the last equation is the background humidity which we assume to be zero. While these equations needs to be integrated, the boundary layer height is directly diagnosed as

$$h(x) = \frac{1}{\gamma_\theta} \left(\Delta\theta(x) + \theta(x,h) - \theta_0\right) \ .$$

The integral equations for $\Delta\theta$, θ_{lm} and q_m read

$$\Delta\theta(x) = \Delta\theta_0 + \frac{\gamma_\theta \Upsilon}{\bar{u}} \int_0^x \frac{Q_h(x)}{\rho(x) c_p \Delta\theta(x)} dx - \Big(\theta(x) - \theta(0)\Big)_{z=h} \tag{2.80}$$

$$\begin{aligned}
\theta_{lm}(x) = \theta_{lm}(0) + \frac{1}{\bar{u}} \Bigg(\Upsilon \int_0^x \frac{Q_h(x)(\gamma_\theta h(x) + \theta_{lm0} - \theta_{lm}(x))}{\rho(x) c_p \Delta\theta(x) h(x)} dx \ \ldots \\
+ \int_0^x \frac{Q_h(x)}{\rho(x) c_p h(x)} dx - \frac{L_v}{c_p} \int_0^x \frac{P(x)}{h(x)} dx \Bigg)
\end{aligned} \tag{2.81}$$

$$\begin{aligned}
q_m(x) = q_{m0} + \frac{1}{\bar{u}} \Bigg(-\Upsilon \int_0^x \frac{Q_h(x)}{\rho(x) c_p \Delta\theta(x) h(x)} q_m(x) dx + \int_0^x \frac{Q_e(x)}{\rho(x) L_v h(x)} dx \ \ldots \\
- \int_0^x \frac{P(x)}{h(x)} dx \Bigg)
\end{aligned} \tag{2.82}$$

(2.80), (2.81), and (2.82) have to be solved numerically. We use the trapezoidal method to solve these integrals. This method works, but as Press et al. (1996a) states it in *Fortran numerical recipes: Vol. 1: Numerical recipes in Fortran 77: the art of scientific computing*;

> *The classical formulas for integrating a function whose value is known at equally spaced steps have a certain elegance about them, and they are redolent with historical*

association. Through them, modern numerical analyst communes with the spirits of his or her predecessors back across the centuries, as far as the time of Newton, if not farther. Alas, time do change; with the exception of two of the most modest formulas ("extended trapezoidal rule" and "extended midpoint rule"), the classical formulas are almost entirely useless. They are museum pieces, but beautiful ones.

As the quote says, the way we chose to integrate our equation might not be the best solution. Solving it with a Runge Kutta 4th order scheme, referred to as an "old work horse" in Press et al. (1996b) and what to use when "you don't know any better", might have given faster convergence and a more accurate solution to the equations. Nonetheless, the trapezoidal rule gives convergence normally within the five first iterations or less, and as our model is relatively computational efficient, we are satisfied with its performance.

Furthermore, we need to choose Δx to ensure stability of our solutions. As the equations are on the form $\frac{dA}{dx} = -kA$, this gives solutions that change over an interval $L = 1/k$. Δx needs to resolve this scale, such that approximately $10\Delta x = L$. If Δx is too large, the appropriate scales are not resolved, and hence the solution breaks down. To avoid this, we choose $\Delta x = 100m$.

Calculation routine

To initialize the model, we specify initial values. These values are used to calculate the sensible and latent heat fluxes, Q_{h0} and Q_{e0}. In $x = 0$, the first guess estimates are based on the following equations;

$$\theta_{lm}(0) = \theta_{lm0} + \frac{\Delta x}{\bar{u}} \left(\Upsilon \frac{Q_{h0}(\gamma_\theta h_0)}{\rho_0 c_p \gamma_\theta h_0} + \frac{Q_{h0}}{\rho_0 c_p h_0} - \frac{L_v}{c_p} \frac{P_0}{h_0} \right) \tag{2.83}$$

$$\Delta\theta(0) = \Delta\theta_0 + \frac{\Delta x}{\bar{u}} \left(\gamma_\theta \Upsilon \frac{Q_{h0}}{\rho_0 c_p \Delta\theta_0} - \theta(0)|_{z=h} + \theta_0|_{z=h} \right) \tag{2.84}$$

$$h(0) = \frac{1}{\gamma_\theta} \left(\Delta\theta(0) + \theta(0)|_{z=h} - \theta_0|_{z=h_0} \right) \tag{2.85}$$

$$q_m(0) = q_{m0} + \frac{\Delta x}{\bar{u}} \left(-\Upsilon \frac{Q_{h0}}{\rho_0 c_p \Delta\theta_0 h_0} q_{m0} + \frac{Q_{e0}}{\rho_0 L_v h_0} - \frac{P_0}{h_0} \right) \tag{2.86}$$

The density is a function of x, but it is assumed to be constant throughout the boundary layer. It is approximated to be

$$\rho(x) = \frac{p_0 \cdot 100}{R \cdot \overline{\theta_m}} \ , \tag{2.87}$$

where p_0 is a reference pressure, θ_m is the mean potential temperature in the layer at the same reference pressure and R is the gas constant.

1. The first-guess estimate for the atmospheric parameters in $x = x_0 + \Delta x \cdot i$ is guessed to be equal to the respective parameters in $x = x_0 + \Delta x \cdot (i-1)$, or if $x = 0$, the first-guess estimates are just the initial values.

2. The model proceeds with calculating the liquid water potential temperature, temperature discontinuity at the top of the boundary layer, and total mixing ratio based on the first-guess estimates with the following equations (or if $x = 0$, on equations (2.83), (2.84), and (2.86)):

$$\theta_{lm}(i) = \theta_{lm} + \frac{1}{\bar{u}}\frac{\Delta x}{2}\left[\left(\frac{Q_{h0}(\gamma_\theta h_0)}{\rho_0 c_p \Delta\theta_0} + \frac{Q_h(i)(\gamma_\theta h(i) + \theta_0 - \theta_{lm}(i))}{\rho(i)c_p\Delta\theta(i)h(i)} + \cdots\right.\right.$$
$$\left.\left. 2\sum_{k=1}^{i-1}\frac{Q_h(k)(\gamma_\theta h(k) + \theta_0 - \theta_{lm}(k))}{\rho(k)c_p\Delta\theta(k)h(k)}\right) + \left(\frac{Q_{h0}}{\rho_0 c_p h_0} + \frac{Q_h(i)}{\rho(i)c_p h(i)} + 2\sum_{k=1}^{i-1}\frac{Q_h(k)}{\rho(k)c_p h(k)}\right)\cdots\right.$$
$$\left.\cdots - \frac{L_v}{c_p}\left(\frac{P_0}{h_0} + \frac{P(i)}{h(i)} + 2\sum_{k=1}^{i-1}\frac{P(k)}{h(k)}\right)\right] \tag{2.88}$$

$$\Delta\theta(i) = \Delta\theta_0 + \frac{\gamma_\theta \Upsilon}{\bar{u}}\frac{\Delta x}{2c_p}\left(\frac{Q_{h0}}{\rho_0\Delta\theta_0} + \frac{Q_h(i)}{\rho(i)\Delta\theta(i)} + 2\sum_{k=1}^{i-1}\frac{Q_h(k)}{\rho(k)\Delta\theta(k)}\right) - \theta(i)|_{z=h} - \theta_0|_{z=h_0} \tag{2.89}$$

$$q_m(i) = q_{m0} + \frac{\Delta x}{\bar{u}}\left[-\Upsilon\left(\frac{Q_{h0}q_{m0}}{\rho_0 c_p\Delta\theta_0 h_0} + \frac{Q_h(i)q_m(i)}{\rho(i)c_p\Delta\theta(i)h(i)} + 2\sum_{k=1}^{i-1}\frac{Q_h(k)q_m(k)}{\rho(k)c_p\Delta\theta(k)h(k)}\right)\cdots\right.$$
$$\left. + \left(\frac{Q_{e0}}{\rho_0 L_v h_0} + \frac{Q_e(i)}{\rho(i)L_v h(i)}2\sum_{k=1}^{i-1}\frac{Q_e(k)}{\rho(k)L_v h(k)}\right) - \left(\frac{P_0}{h_0} + \frac{P(i)}{h(i)} + 2\sum_{k=1}^{i-1}\frac{P(k)}{h(k)}\right)\right] \tag{2.90}$$

3. To find an estimate for h, we need to diagnose the potential temperature at the top of the ABL. If moisture is not included or saturation does not occur, then $\theta|_{z=h} = \theta_{lm}$. However, if moisture is included, we need to calculate whether condensation occurs or not. To do this, we find the level where saturation occurs. We diagnose the saturation level based on the assumption that dry adiabatic conditions are valid beneath the cloud base. This gives us a temperature profile within the boundary layer from which we can infer the saturation mixing ratio with the Clausis-Clapeyron relationship. If the height where saturation occurs is below the boundary layer height, we take this height to be the cloud base z_c. If not, condensation does not occur in the ABL.

4. If the calculated cloud base height, z_c, is below the ABL height, then we know that saturation occurs within the ABL. We have the temperature and pressure at $z = z_c$, and we

assume that if a parcel continues to rise, it will follow the moist adiabat. Calculating the resulting q_s through the cloud gives the liquid water content; $q_l = q_m - q_s$

5. The knowledge of the liquid water content in the cloud, and the precipitation, allows us to use (2.1) to calculate the potential temperature at the top of the boundary layer. If condensation does not occur in the ABL, the potential temperature at the top of the ABL is just equal to θ_{lm}. When we know the potential temperature at the top of the ABL, we can return an estimate for the boundary layer height (or if $i = 0$, (2.85));

$$h(i) = \frac{1}{\gamma_\theta} \left(\Delta\theta(i) - \theta_0|_{z=h_0} + \theta(i)|_{z=h} \right) \ . \tag{2.91}$$

6. If the ocean is coupled to the atmosphere, the sensible and heat flux are used to calculate new mixed layer temperatures and salinity, which are returned. For details, see section 2.3.2.

7. We redo the calculations of the sensible and latent heat fluxes with the revised estimates of θ_l and q_m, and if the ocean the mixed layers are coupled, T_m, the ocean mixed layer temperature.

8. With the new heat fluxes, we redo step 2) to 7) with all the updated values until $\theta|_{z=h}$ converges within ε. We use $\theta|_{z=h}$ as our convergence criterion because it is affected by moisture. Therefore, when $\theta|_{z=h}$ has converged, the other variables have converged as well.

2.3.2 Mixed layer ocean model

To initialize the ocean, we first create idealized temperature and salinity profiles based on the NOAA climatology (Boyer et al., 2015). We mix the upper layer to a specified mixed layer depth, which can be arbitrary and is specified a priori. Further, we fit the profiles to an arctan-function such that the gradient, the depth of the thermocline or halocline, and the surface and deep value roughly match the profiles. An example is shown in figure 3.2, which shows that the salinity and density profiles match rather well, but with some finer structures removed. The temperature profile is less accurate, but the setup has a stable stratification.

The solution of the ocean is simpler as it does not contain an $x-$dependence. Instead, to mimic a time dependence or advection, the solution is relaxed toward a pre-defined state. The relaxation prevents the ocean from cooling the ocean infinitely, and allows for a steady state to be reached. The steps listed below are the same for all x.

1. We use the mixed layer temperature, T_m (which are equivalent to θ_{SST}) and the lowest value of the potential temperature to calculate the heat fluxes. With the heat fluxes, we can calculate the buoyancy loss from the ocean. This gives us new temperature and salinity values for the mixed layer.

2. After calculating the new temperature and salinity values for the mixed layer, we calculate the density of the mixed layer and check if this is heavier than the layer below. If it is, mixing occurs gradually until stability is achieved. Mixing occurs gradually in the sense that it the mixed layer depth is increased by one meter, mixed with the underlying water, and checked if the stability restored. If the stability is not restored, then the mixed layer is increased by another meter. The routine is repeated until stability is restored. This process provides new estimates of mixed layer depth, temperature, and salinity.

3. The new mixed layer temperature, T_m are used to calculate the new heat fluxes. Using the new heat fluxes, the model calculates revised estimates of the atmospheric properties, which are then used to calculate new heat flux values. Unlike the atmosphere, climatology is used as a first guess estimate for the ocean parameters at all x.

2.4 Sea ice distribution

To investigate the influence of the MIZ on air-sea interaction, we prescribe different sea ice distributions in our model. We assume that the sea ice is sufficiently thick so there is no flux from the ocean to the atmosphere in the sea ice covered regions. The sea ice representation in this model is significantly simplified, with constant heat and transfer coefficients. We compute the heat fluxes within the marginal ice zone by weighting it by the open-water area, which is often referred to as tiling.

We assume that the MIZ has a smooth shape and express the sea ice concentration (or area fraction) as a tangens hyperbolicus function, similar to Chechin et al. (2013),

$$A = 0.5 - 0.5 \tanh\left(\frac{x - x_c}{L}\right) \tag{2.92}$$

where $3L \approx L_{MIZ}$ is the width of the marginal ice zone and x_c is the centre of the MIZ.

To investigate whether the shape of the sea ice concentration has any influence on the downstream boundary layer development, we split the tanh function in two, such that the upper part, for $x < x_c$, represents the sea ice declining mostly at the end, whereas $x > x_c$ represents the sea ice concentration declining most at the beginning (figure 2.3). We also compare this with a linear profile, where the sea ice concentration declines uniformly through the domain as well as a step function. To best compare the different profiles, we make sure that the domain-integrated sea ice is identical.

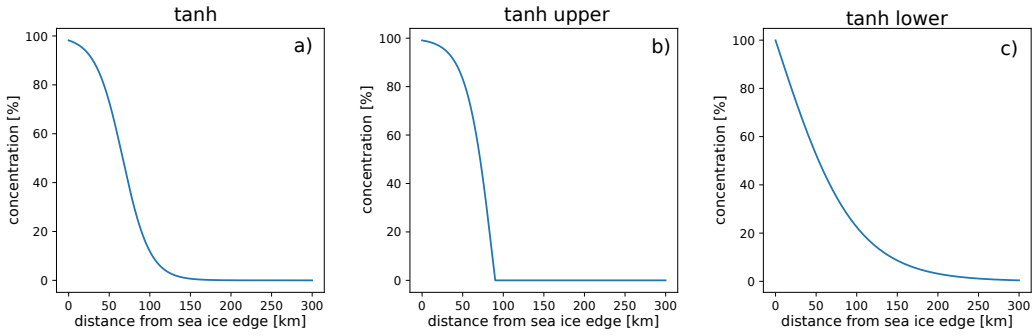

Figure 2.3: Three examples of the idealized setup of the MIZ. a) tanh sea ice distribution with width of 150 km, b) upper portion of a), modified to have the same area, and c) lower portion of a) also with the same area. The sea ice edge here is defined as the 100% concentration line

.

2.5 Diagnostics

In order to investigate the results in more detail, we construct budgets for the total mixing ratio, liquid water potential temperature, water vapour, liquid water, and potential temperature. The budgets for liquid water potential temperature and total mixing ratio are based directly on the model equations (2.20) and (2.34), respectively. On the other hand, the budgets for potential temperature, as well as water vapour and liquid water requires the knowledge of condensation, which has to be calculated. We calculate each term in the equations explicitly to look at their relative contribution. We also construct temperature and salinity budgets for the ocean, based directly on the model equations (2.67) and (2.78), respectively.

2.5.1 Budget for potential temperature

The budget for the potential temperature is similar to the budget for the liquid water potential temperature, except that condensation serves as a source of heating within the layer.

We once again assume horizontal homogeneity and stationarity within the mixed layer and no mean vertical motion at the top or bottom of the boundary layer, such that the equation for potential temperature can be expressed as:

$$\bar{u}\frac{\partial\theta(z)}{\partial x} = -\frac{\partial\overline{w'\theta(z)'}}{\partial z} + \frac{L\theta}{l_p T}c \ . \tag{2.93}$$

Here, c represents the condensation, which accounts for both the increase in liquid water content, $\frac{\partial q_{lm}}{\partial x}$, and the liquid water lost to the free atmosphere through entrainment in addition to the liquid water lost through precipitation. For simplicity, we assume that $\frac{\theta}{T} \approx 1$. We integrate (2.93) over the boundary layer height and take the average. As before, we ignore the Leibniz term (refer to section 2.1.1), and (2.93) can be written as

$$\bar{u}h\frac{\partial\theta_m}{\partial x} = -\overline{w'\theta'}|_{z=h} + \overline{w'\theta'}|_{z=0} + h\frac{L_v}{c_p}\tilde{c} \ , \tag{2.94}$$

where $\tilde{c}$ is the mean condensation within the layer. The fluxes at the top of the ABL and the surface fluxes in (2.94) are parameterized similarly as before ((2.13) and (2.12)).

2.5.2 Budget for water vapour

The budget for water vapour differs from that of the budget of total mixing ratio in that the sink for water vapour in addition to entrainment is through condensation - conversion from vapour to liquid water. The change of water vapour can be written similar as the potential temperature budget

$$\bar{u}\frac{\partial q_v}{\partial x} = -\frac{\partial\overline{w'q_v'}}{\partial z} - c \ . \tag{2.95}$$

We integrate (2.95) over the boundary layer, yielding

$$\bar{u}h\frac{\partial q_{vm}}{\partial x} = -\overline{w'q'_v}|_{z=h} + \overline{w'q'_v}|_{z=0} + h\tilde{c} \ . \tag{2.96}$$

We approximate the entrainment as $\overline{w'q'_v}|_{z=h} = -w_e\Delta q_v$, where the entrainment velocity is similar to before, and the surface flux is equal to (2.31).

2.5.3 Budget for liquid water

The only source for liquid water within the mixed layer is through condensation, and the sinks are entrainment and precipitation. The change in liquid water can therefore be expressed as

$$\bar{u}\frac{\partial q_l}{\partial x} = -\frac{\partial \overline{w'q'_l}}{\partial z} + \bar{\dot{q}} \ . \tag{2.97}$$

Integrating (2.97) over the boundary layer and taking the average yields

$$\bar{u}h\frac{\partial q_{lm}}{\partial x} = -\overline{w'q'_l}|_{z=h} + \overline{w'q'_l}|_{z=0} \ . \tag{2.98}$$

Here, the flux of liquid water through the surface is defined as precipitation and is identical (2.30). Furthermore, $\bar{\dot{q}}$ disappears when we integrate over the boundary layer (see section 2.1.1). The entrainment is similar to (2.32), but only the jump in liquid water at the top of the boundary layer is considered. Hence, to calculate the change in liquid water content, we assume that the condensation must account for the liquid water content in the layer, the precipitable water, and the loss of liquid water to the free atmosphere through entrainment.

2.5.4 Budget ratios

To compare our results with e.g. Brümmer (1996b) we compose ratios of the various terms in the budget. An overview is given below.

Bowen ratio The Bowen ratio is a measure of the sensible to latent heat cooling, and can be expressed as

$$B_o = \frac{c_p c_H(\theta_{SST} - \theta_0)}{L_v c_E(q_s - q_a)} = \frac{Q_H}{Q_E} \ . \tag{2.99}$$

The saturation vapour pressure is strongly dependent on temperature. Over a warm wet surface, such as in the tropics, latent cooling dominates over the sensible heat flux, whereas for high latitudes where the surface is generally cold, the sensible heat flux tend to dominate (Hartmann, 2016), which is the case for CAOs at high latitudes. This is different to CAOs over the Gulf Stream, where cold continental air flows off the east coast of USA and encounters the relatively warm water of the Gulf Steam. In these CAOs, the latent heat flux might dominate

over the sensible heating, and consequently the Bowen ratio is less than 1.

The latent heat flux is constrained by the saturation with respect to the SST (Papritz et al., 2015). The sensible heating term is on the other hand constrained by the temperature difference between the ground temperature in the ABL and the SST.

Condensation to evaporation The ratio of water vapour condensed to the water vapour supplied from the surface is expressed as $\frac{\tilde{c}}{\overline{w'q'}|_{z=0}}$. Brümmer (1996b) found this value to continuously increase away from the sea ice edge, form 0.4 to 0.8, and was dependent on the type of convection. Our model does not resolve convection, and therefore this ratio might deviate from what is observed.

Precipitation to condensation Describes how efficiently condensation is converted into precipitation, $P/\tilde{c}$. Observations show that this ratio is close to 0.75, and does not vary considerably with fetch (Brümmer, 1996b).

Precipitation to evaporation The efficiency of precipitation production in relation to the surface vapour flux, $\frac{P}{\overline{w'q'}|_{z=0}}$, and is observed to increase away from the sea ice edge, from about 0.3 to 0.6 (Brümmer, 1996b).

Entrainment to surface flux In our mixed layer model, the ratio between the entrainment heat flux and the surface heat flux ($\frac{\overline{w'\theta'}|_{z=h}}{\overline{w'\theta'}|_{z=0}}$) is constant; 0.2. However, in observations, the ratio is relatively high close to the sea ice edge where the boundary layer increases rapidly, and the ratio decreases away from the sea ice edge (Brümmer, 1996b).

Net condensation to surface flux heating Net condensation to surface flux heating, $\frac{\frac{L_v}{c_p}\tilde{c}}{\overline{w'\theta'}|_{z=0}}$Increases from 0.25 near the sea ice edge to values near 1.3 of more than 300 km downstream.

2.5.5 Ocean heat loss

To calculate the heat loss from the ocean, we compare the initial temperature profile to the final profile in the same grid point. The difference in heat content over the entire mixed layer depth is obtained by multiplying the temperature with the density and specific heat capacity of seawater.

2.5.6 Sea ice

Sea ice growth is not included in the model, but it is possible to diagnose the maximal potential sea ice growth based on the cooling to below the freezing point of seawater. This does not take into consideration that as the sea ice grows thicker, it also grows slower as the heat has to escape through the sea ice (Leppäranta, 1993). Hence, this calculation can only serve as a rough upper estimate of how much sea ice is possibly formed if the sea ice is continuously removed.

We estimate the sea ice thickness, I, as

$$I = \frac{C_{po}\rho_o(T_f - T_m)H}{L_I\rho_I} \ , \tag{2.100}$$

where T_f is the freezing point of seawater, a function of both temperature and salinity (calculated with the seawater package (Fernandes, 2014)). Further, L_I is the latent heat of freezing, 3.3×10^5 J/kg, and ρ_I is the density of sea ice, which typically is 917kg/m^3.

As sea ice forms, it rejects brine, which leads to an increase in salinity of the ocean mixed layer. This is not accounted for in the model, but nevertheless we can calculate the salinity increase in the mixed layer a posteriori, and further check if this is sufficient to cause convection in the mixed layer. To calculate the salinity increase we use

$$\Delta S = \frac{\rho_I L_I(S_m - S_I)}{H\rho_o} \ , \tag{2.101}$$

where S_I is the salinity of the ice. The salinity of newly formed ice can be as high as 10 g/kg, but as the ice gets older, the salinity decreases. On average, first year ice has a salinity between 4-6 g/kg (Wadhams, 2000). We use $S_I = 5$ g/kg.

3 Results

To showcase the capabilities of the model, we first present a typical CAO, where we investigate the atmospheric and oceanic response. We also compare the model results with observations from Arctic field campaigns before investigating how the different components of the model behave and test sensitivity to the initial values. Thereafter, we perform a sensitivity test with respect to the extent and structure of the MIZ.

3.1 Reference run

CAOs are typically identified with the potential temperature difference between the sea surface and a pressure level, chosen between 850 hPa and 700 hPa (Kolstad and Bracegirdle, 2008; Papritz and Spengler, 2017; Kolstad, 2011). Weak CAOs are associated with a temperature difference less than 4 K, moderate and strong between 4-8 K, and 8-12 K, respectively, and very strong with differences greater than 12 K (e.g., Papritz and Spengler, 2017). In addition, a characteristic of CAO air masses is their absolute dryness prior to CAO formation (< 0.5 g/kg) (Papritz and Spengler, 2017). We thus choose our typical CAO values to be $\theta_0 = 253$ K, $\gamma_\theta = 0.012$ K m^{-1}, in accordance with data from the literature (Hartmann et al., 1997; Renfrew and King, 2000; Chechin et al., 2013). It is also within the range of stability (between 0.032 K/m and 0.006 K/m) from the radiosonde from 20 March 1993 over the sea ice (figure 3.1, initial values are plotted with the green line). Finally, we set the initial humidity to 0.30 g/kg. This is the mean of all the specific humidity sampled over the sea ice during ARKTIS1993 which were below 0.5 g/kg (Brümmer, 1996a). (Brümmer, 1996a) measured wind speeds between 4 m/s to 13 m/s in CAOs. Furthermore, the wind speed is observed to increase downstream of the sea ice edge (Chechin et al., 2013), which is not accounted for in our model. Therefore, we choose a wind speed of 10 m/s for our reference. Further, Guest et al. (1995) did a simple scale analysis, and showed that the distance for the atmosphere to adjust to a step in surface temperature, for example in the transition between fast ice and open waters, was about $\sim$300 km. Hence, this is also the scale of interest for cold air outbreaks, and also the scale where we expect the largest variability.

For the ocean mixed layer, we use an idealized profile based on the winter climatology of

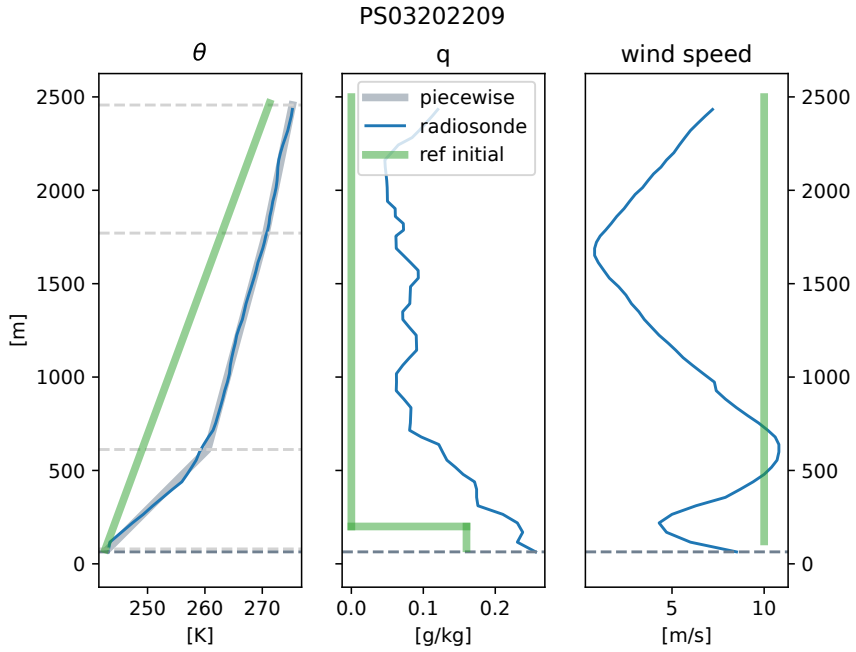

Figure 3.1: Example of radiosonde data from ARKTIS1993, taken from the ship *Polarstern*. Left: potential temperature, middle: specific humidity, right: wind speed. The green line (ref initial) indicates the initial values in the reference run. For details about 'piecewise' radiosonde profile, refer to appendix A.1.

a location in the Greenland Sea (75.5°N, -7.5°E, figure 3.2). The density and salinity profile is well captured, but the temperature profile is missing the feature of the warm tongue underneath the mixed layer. The salinity is more important than temperature in determining the density structure at high latitudes, which can be seen in TS-diagram, and therefore, neglecting the warm tongue will not cause any issues in the stability of the water column. Neglecting the warm tongue will cause a slight increase of the stability of the water column, and might therefore inhibit convection. However, in the absence of mixed layer deepening, neglecting the warm water underneath will not have any impact on the OML as entrainment of the water in the pycnocline is not accounted for. Therefore, for the sake of simplicity of the profile, we neglect the warm tongue. Furthermore, we choose a mixed layer of 50 m, surface salinity of 34.5 g/kg, and SST of 1°C. This is within the range of temperatures encountered during CAOs in the Arctic over the Fram Strait (Hartmann et al., 1997; Brümmer, 1996a; Chechin et al., 2013). The initial profile is constant with fetch, but the SST and salinity are allowed to respond to the turbulent heat fluxes and precipitation with a relaxation time scale of one day ($\tau = 1$).

The ABL height grows at a rate similar to $x^{1/2}$ (figure 3.3a), which is similar to the growth rate we expect from a constant heat flux and dry convection (Stevens, 2007). The ABL height increases to approximately 1 km around 300 km downstream of the sea ice edge. The heating

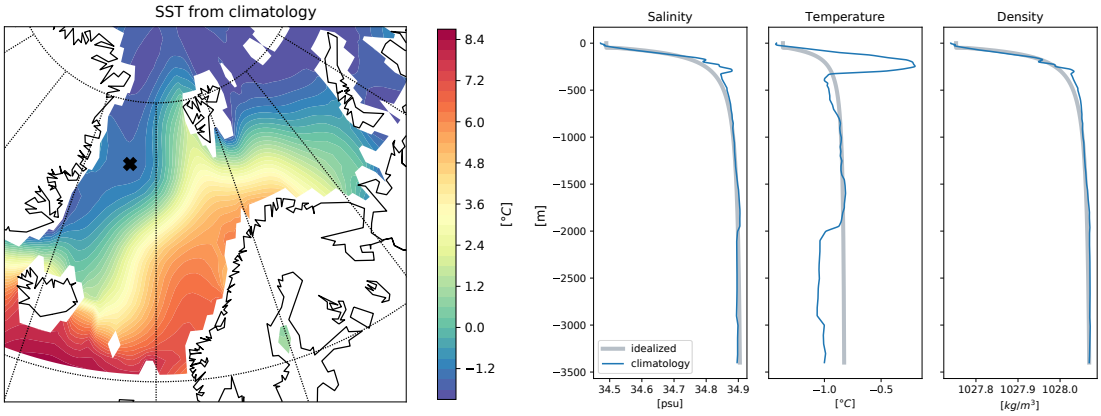

Figure 3.2: Left: climatology of SST, right: idealized temperature, salinity and density profiles based on the climatology from the right in the climatology in the location of the black cross.

of the layer is mainly due to the sensible heat flux, which is consistent with Chang and Braham (1991), who found that the heat flux convergence accounted for roughly 75% of the heating of the ABL. The sensible heat flux is largest at the sea ice edge, where the boundary layer height grows the fastest. The sensible heat flux decreases from 450 W/m^2 near the sea ice edge to 180 W/m^2 at 300 km downstream (figure 3.3b). The sensible heat flux dominates the latent heat flux the first 150 km, but 300 km downstream, the latent heating becomes more important. This is reflected in the Bowen ratio (see section 2.5.4). The Bowen ratio decreases from 1.52 in the first 30 km downstream of the sea ice edge, to 1.11 between 150 km and 300 km downstream. The decrease in the Bowen ratio is caused by the decreasing difference between the air-sea temperatures (figure 3.3h) which leads to a lower sensible heat flux.

The total mixing ratio increases steadily throughout the domain (figure 3.3c) due to the latent heat fluxes. However, condensation and the formation of clouds and rain lead to an increase of the liquid water mixing ratio (figure 3.4a). The maximum liquid water content is 0.39 g/kg, located far downstream where the cloud layer thickness is at its maximum, just below the top of the ABL.

As the cloud layer forms, the liquid water releases latent heat which causes the potential temperature to increase within the cloud layer (figure 3.4b). Where we have the highest liquid water content is through the definition of liquid water potential temperature (2.1), also where we have the maximum potential temperature. The temperature at the top of the cloud layer is 1 K higher than the potential temperature in the below-cloud layer.

However, even though the temperature is higher at the top of the boundary layer than at the ground due to condensation, this increase is small compared to the input from the sensible heating. Of the mean potential temperature increase of 12.5 K, only 7.6% can be attributed to

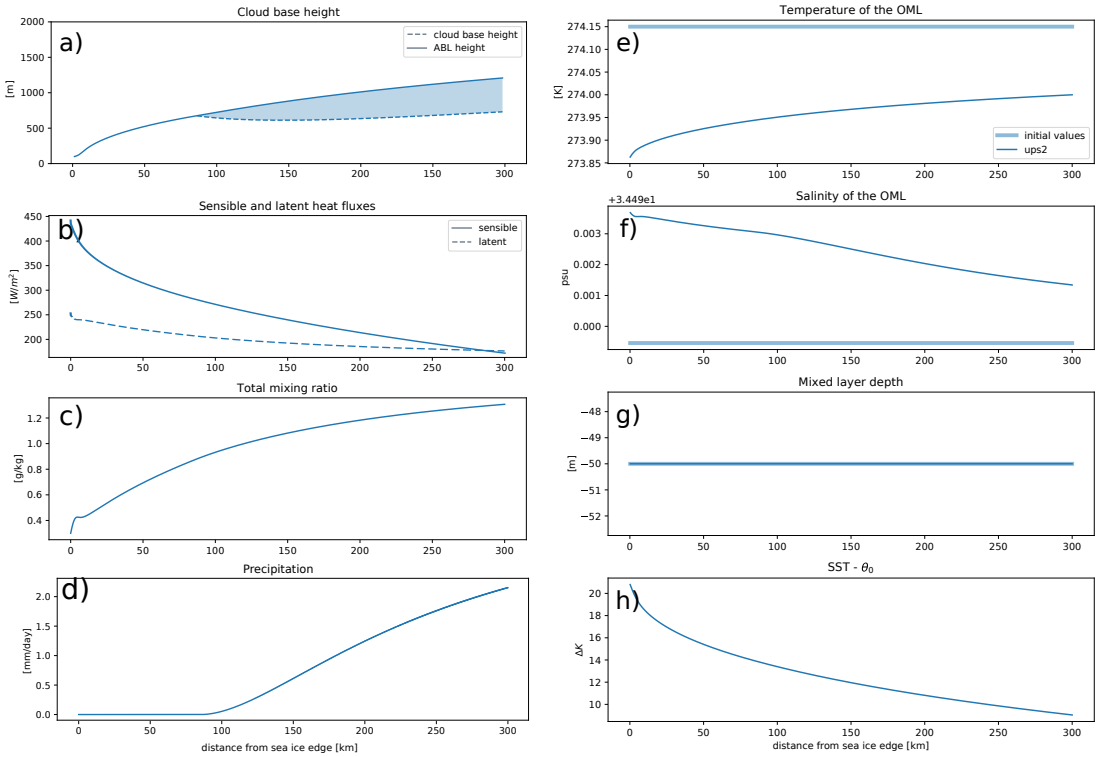

Figure 3.3: ABL and OML characteristics and their respective change with distance from the sea ice edge for the reference run.

the latent heat release (figure 3.5a). Sensible heating and entrainment dominates, with 77.0% and 15.4%, respectively. Between 150-300 km however, the latent heating is more important and accounts for 23.0%, the sensible heating for 64.2%, and the entrainment for 12.8% (box3 in figure 3.5a). This is consistent with Chang and Braham (1991), who estimated that the entrainment and sensible heat flux accounts for 75% of the warming in the ABL for a case of lake convection over Lake Michigan.

In addition to the latent heat release, the cloud also produces precipitation (figure 3.3d). The rate of precipitation increases steadily away from the sea ice edge after the cloud layer forms. In our model formulation, the precipitation scales directly with the cloud thickness and liquid water content. The cloud layer has its maximum thickness 300 km from the sea ice edge, and hence we also find the highest precipitation rates there. The maximum precipitation rate is 2.0 mm/day. The rates are similar to the results from the operationally used COSMO model, which predicts 2.4 mm/day to 9.6 mm/day around 300 km downstream for a vigorous CAO (Papritz and Sodemann, 2018), indicating that we are able to reproduce important behaviour during CAOs in our

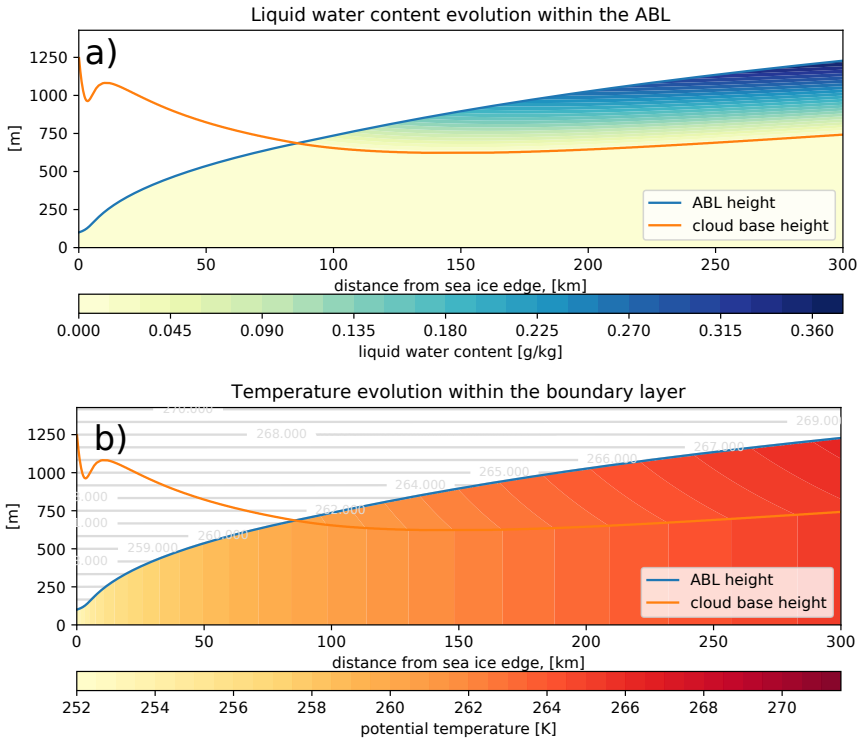

Figure 3.4: Liquid water content, a), and potential temperature, b). The grey contours in b) indicates the overlying stability.

model.

Furthermore, the precipitation to evaporation ratio in our model is at most 23%, whereas (Brümmer, 1996b) got an estimate of 25% to 33% up to 150 km, and the ratio increased to 50% further downstream. Papritz and Sodemann (2018) estimated the precipitation to evaporation ratio to be 34%. Our model is on the lower end of these results, but this ratio is very sensitive to the onset of precipitation, which is dependent on both the initial air temperature, the initial moisture, the SST, and the evaporation rate. Therefore, as the cloud onset is relatively late compared to the CAOs of Brümmer (1996a), who observed clouds just off the sea ice edge in all the CAOs (figure 3.3a), the estimates are of comparable magnitude, but may not be at the correct location. In addition, the precipitation rate might increase due to synoptic scale moisture convergence, which is not taken into account.

Figure 3.5b shows that the contribution from liquid water becomes significant for $x > 150$ km. Condensation is the only source for liquid water, and it is removed both through entrainment and precipitation, where precipitation dominates. The rate of entrainment might be overesti-

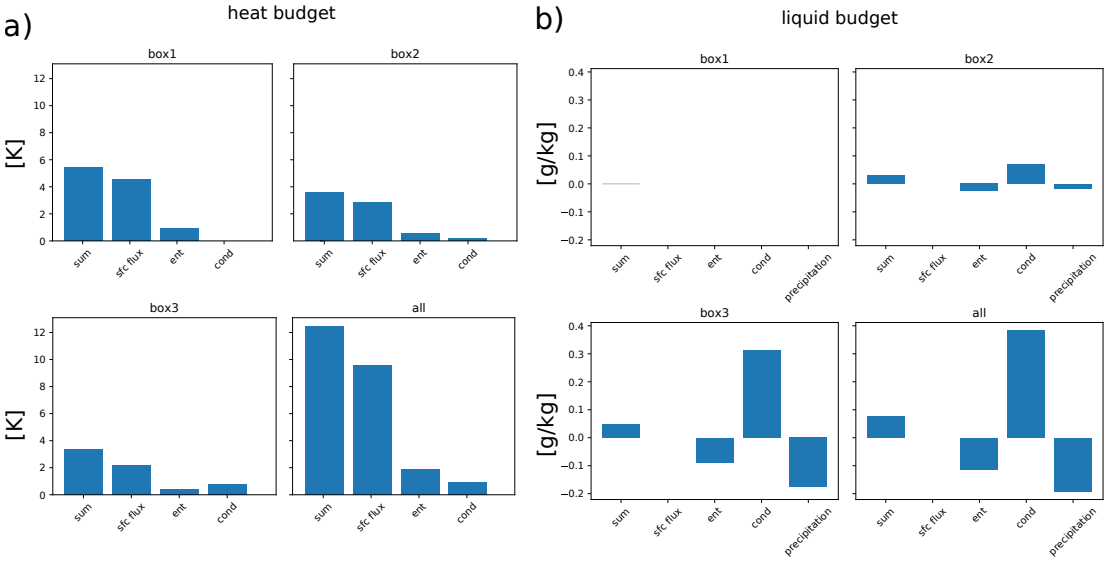

Figure 3.5: The integrated contribution from the different terms in the mean potential temperature a) and mean liquid water b) equations in the box 0-30 km (box1), 30-150 km (box2) and 150-300 km (box3). 'all' is the total change between 0-300 km.

mated, as we assume the free atmosphere to be completely dry. While this assumption might be acceptable for liquid water, it is less accurate for vapour as the atmosphere is not completely dry, and sometimes moisture even increases with height. This would lead to an overall lower total mixing ratio in the ABL. The lower mixing ratio would cause the condensation rates to decrease and would hence lead to an overestimation of the entrainment of liquid water.

The ocean mixed layer depth is unchanged (figure 3.3g). The SST has cooled by 0.28 K close to the sea ice edge, and 0.15 K at 300 km. This cooling distributed over a 50 m deep layer corresponds to an oceanic heat loss of 7×10^7 J/m^2. A temperature decrease of 0.28 K is consistent with an estimate by Isachsen et al. (2013) which indicated that during a CAO, the mean observed temperature decrease was 0.4 K. This also indicates that our relaxation time scale is reasonable, and could even be increased.

Overall, the mixed layer experiences a salinification due to evaporation (figure 3.3f). This is most notable close to the sea ice edge. As cloud and precipitation form in addition to the decreasing latent heat flux (figure 3.3b) the layer becomes increasingly fresher downstream. However, the changes are small, on the order of 10^{-5}, which is not sufficient to contribute to a densification in the layer to erode the stable density stratification to deepen the mixed layer.

3.2 Evaluation of model performance - comparisons

In order to validate our model, we compare it to case studies of cold air outbreaks over the Fram Strait. We test the model against the ARKTIS1993 campaign with the data set from Jeske et al. (2012), and to the budgets from Brümmer (1996b) based on the same campaign. Further, we compare it with observations from Hartmann et al. (1997), measured during a CAO in October 1991 over the Fram Strait. Based on the comparison, we tuned the model to be more consistent with observations.

3.2.1 ARKTIS 1993

Brümmer (1996a) conducted the field campaign ARKTIS1993 to study of the boundary layer modification in wintertime CAOs in the Arctic. The field campaign successfully sampled 10 CAOs by airplane from the Arctic sea ice to the open waters of the Fram Strait. The distance covered by the aircraft ranged from 50 km over the sea ice to about 300 km over open water. The data over the sea ice serves as our initial conditions (see table 3.1). The lapse rate γ_θ is taken to be the mean of the lapse rates measured over the sea ice and over open water, and we assume that the SST follows an *arctan*-profile, such that the SST increase rapid away from the sea ice, which has been observed during previous CAOs over the Fram Strait (figure 3.6). (Hartmann et al., 1997).

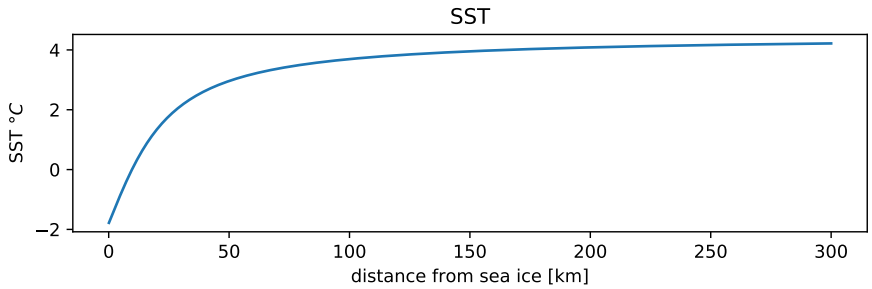

Figure 3.6: Initial SST distribution when the upstream temperature is 4°C, such as for the 5 March.

The model consistently underestimated the boundary layer height when we use the stability measured by the aircraft (figure 3.7). For the 10 March, the boundary layer height is underestimated by 800 m 270 km downstream of the sea ice edge (figure 3.7). The depth of the ABL is an important parameter as it sets the depth of which the surface and entrainment fluxes must act to warm or moisten the layer. Thus, a too shallow boundary layer can lead to an overestimation of both the potential temperature and mixing ratio, and hence also impact the onset of clouds, which would further feed back to the potential temperature. The underestimation might be an indication that a too strong stratification was initialized in the model. The lapse rates in ta-

Table 3.1: Initial conditions for 10 CAO measured during the ARKTIS flight campaign in 1993. Temperature and moisture is measured at 90m, ΔT_{inv} is the inversion above the boundary layer across a 50 m deep layer, and γ_θ is the mean background lapse rate in all the data points given. The SST is given close to the sea ice edge and then 200 km downstream. The two last columns represent the γ_θ measured by the airplane and the ship *Polarstern* (PS) (data from Jeske et al., 2012), respectively. The PS sounding is the 10:30 UTC sounding except the 20 March were 16:30 UTC sounding is shown, to have the sounding corresponding to the time of the aircraft campaign (Brümmer, 1996b). γ_θ from the soundings represent the mean stability of the lower 2000 m. Adapted from Brümmer (1996a,b)

Date March 1993	h [m]	T [°C]	q [g/kg]	u [m/s]	ΔT_{inv} [K]	SST [°C]	γ_θ [K/m]	PS γ_θ [K/m]
5	340	-22	0.67	6.6	2	-1.8/4.0	0.018	0.016
10	210	-31	0.15	5.44	2	-1.8/2.0	0.020	0.013
11	300	-24	0.50	5	11	-1.8/2.0	0.021	0.018
16	150	-24	0.60	4.26	2	-1.8/4.0	0.083	0.022
19	250	-29	0.30	11.87	6	-1.8/2.0	0.069	0.016
20	200	-29	0.25	15	2	-1.8/2.0	0.055	0.013
24	200	-20	0.28	13.2	11	-1.8/2.0	0.066	-
25	220	-26	0.45	12.1	2	-1.8/2.0	0.033	0.012

ble 3.1 show that there is generally a strong inversion residing over the sea ice. For comparison, Renfrew and King (2000) uses a lapse rate of 0.0092 K/m as a reference case for CAOs, and 0.012 K/m as an example of the presence of a strong inversion, which is higher than the lowest value recorded by the aircraft during ARKTIS1993. It is likely that above this strong inversion, there is a layer of weaker stability which could lead to enhanced boundary layer growth if the inversion is eroded, which is not accounted for in this model. Furthermore, we cannot rule out that $\Delta\theta$ is included in the measurements of the potential lapse rate above the top of the boundary layer. We therefore choose to use radiosondes taken from the same time as the flight campaign and take the mean stratification (see last column of table 3.1).

We further wish to assess how the model is performing in terms of the different processes, and see if their relative importance are consistent with observations. Similar to Brümmer (1996b), we look at the ratios between precipitation, entrainment, surface sensible and latent heat flux, and condensation (a brief discussion of all ratios is also given in section 2.5.4). The ratios in table 3.2 are compared to table 8 in Brümmer (1996b).

The ratio of the sensible heat flux to the entrainment is larger than 0.2 in Brümmer (1996b) estimates (table 3.2). This indicates that our approximation of entrainment might not be entirely

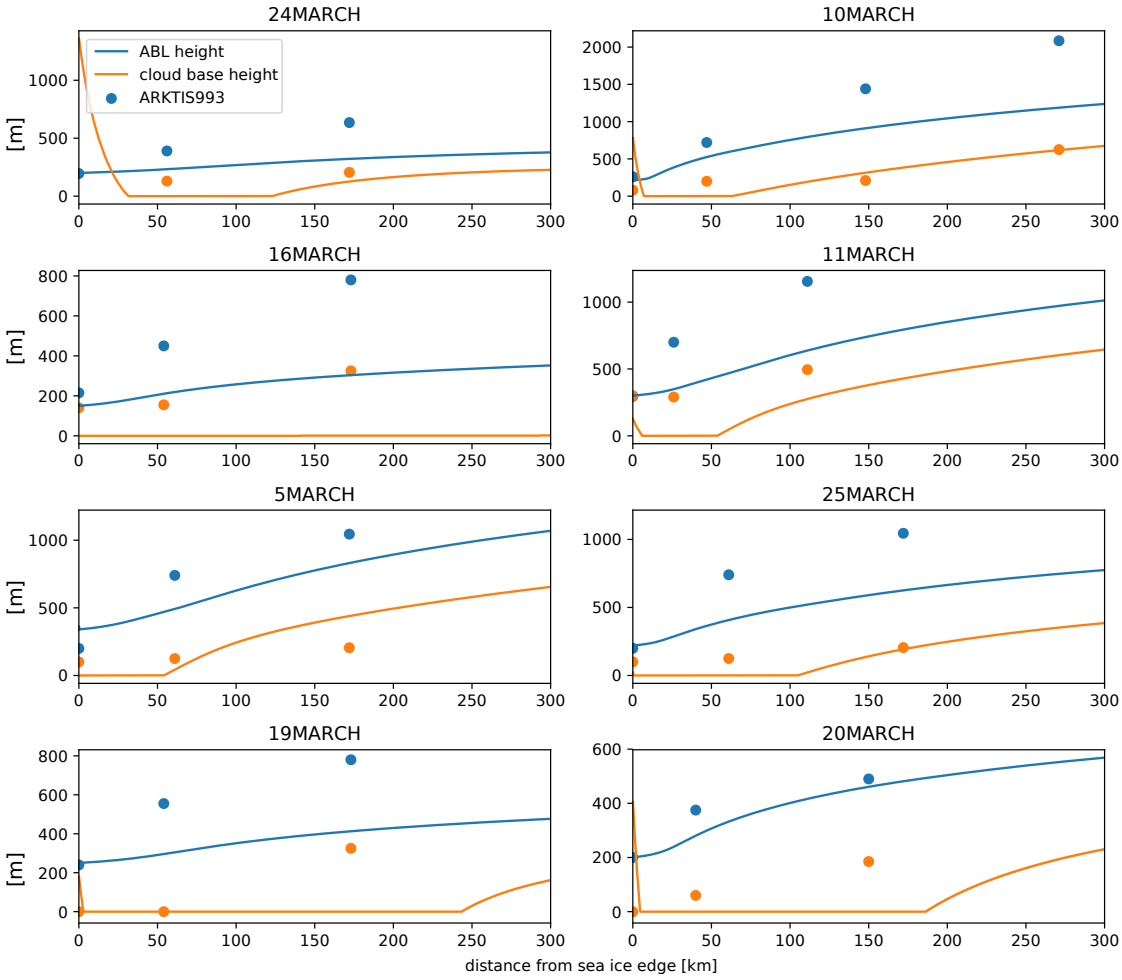

Figure 3.7: Comparisons of the boundary layer height (blue) and cloud base height (orange) between the model (line) and observations (dots) for γ_θ measured by the aircraft.

Table 3.2: Different ratios of condensation to evaporation, precipitation to condensation, precipitation to evaporation, entrainment to surface sensible heat flux, condensation to surface sensible heat flux, and the Bowen ratio, from left to right. The bold are the mean of all the model runs from table 3.1 whereas the light are taken from Brümmer (1996b) table 8.

km	$\frac{c}{\overline{w'q_v'}\|_{z=0}}$	$\frac{P}{c}$	$\frac{P}{\overline{w'q_v'}\|_{z=0}}$	$\frac{\overline{w'\theta'}\|_{z=h}}{\overline{w'\theta'}\|_{z=0}}$	$\frac{c}{\overline{w'\theta'}\|_{z=0}}$	$\frac{c_p\overline{w'\theta'}\|_{z=0}}{L\overline{w'q_v}\|_{z=0}}$
0-30	**0.07**/0.72	**0.39**/0.25	**0.05**/0.25	**0.2**/0.78	**0.02** /0.24	**3.9**/1.49
30-150	**0.14**/0.43	**0.32**/0.74	**0.05**/0.32	**0.2**/0.49	**0.05** /0.33	**2.78**/1.21
150-300	**0.32**/0.70	**0.56**/0.81	**0.20**/0.57	**0.2**/0.30	**0.14**/0.75	**2.2**/0.85
> 300	-/0.86	-/0.77	-/0.66	-/0.49	-/1.32	-/0.85

correct. However, the entrainment is a significant sink of moisture in the boundary layer. The mixing ratio is already underestimated in the model, hence we do not increase this ratio.

The ratios in table 3.2 indicate that the evaporation rate, and hence the latent heat flux, might be underestimated. This is particularly visible in the Bowen ratio (last column), which is more than twice as high as reported by Brümmer (1996b). However, this could also be due to how we prescribed the SST distribution. If the observed SST increases faster in the first 30 km than what we have prescribed, this would lead to lower latent heat fluxes at the beginning of our domain compared to observations. However, the Bowen ratio remains high during the entire domain. In addition to the Bowen ratio, the ratios of condensation to sensible heat heat flux, condensation to latent heat flux, and precipitation to evaporation are also small compared to observations. The ratio of condensation to latent heat flux is one order of magnitude smaller than what (Brümmer, 1996b) calculated. This is also the case with precipitation to evaporation. Papritz and Sodemann (2018) found the rate of precipitation to evaporation to be between 0.25 and 0.5, which is on the lower end of the budgets from ARKTIS1993 (Brümmer, 1996a). Increasing the moisture transfer coefficient, and hence the evaporation rate, would possibly increase the rate of condensation which might lead to an improvement of the ratios compared to observations.

The low Bowen ratio and condensation rate serves as a motivation for increasing the evaporation efficiency. We increase the evaporation efficiency from $c_E = 1.5 \times 10^{-3}$ to $c_E = 2.0 \times 10^{-3}$, while we keep the coefficient for sensible heat $c_H = 1.5 \times 10^{-3}$. Both c_E and c_H are still treated as constants. We calculate new ratios, and see that the increased evaporation efficiency makes the ratios more consistent with Brümmer (1996b) (table 3.3).

The ratios that includes condensation is lower than observed close to the sea ice edge, but they are closer to observations further downstream. Precipitation to latent heat flux is underestimated the most close to the sea ice edge, but this is consistent with an underestimation of the condensation to the latent heat flux as well - therefore, the condensation rates are simply too low in the model compared to observations. This is further backed up by Brümmer (1996b) estimated that the condensation term was the main contribution to the heating budget close to the sea ice edge. This is never the case in our model, where the sensible heat flux always dominates, which might indicate that our condensation rate is underestimated.

However, even though the ratios have improved, the boundary layer height is still underestimated. Therefore, we also use the radiosonde from the ship γ_θ as our stratification. This improves the boundary layer height. However, when the model and the observations already agree, changing the stratification makes the model overestimating the boundary layer height. This highlights the sensitivity of the ABL to the ambient stability, and the need for an accurate lapse rate to capture the structure of the ABL downstream.

Table 3.3: Same as table 3.2 but with increased evaporation efficiency

km	$\frac{c}{\overline{w'q_v'}\|_{z=0}}$	$\frac{P}{c}$	$\frac{P}{\overline{w'q_v'}\|_{z=0}}$	$\frac{\overline{w'\theta'}\|_{z=h}}{\overline{w'\theta'}\|_{z=0}}$	$\frac{c}{\overline{w'\theta'}\|_{z=0}}$	$\frac{c_p\overline{w'\theta'}\|_{z=0}}{L\overline{w'q_v}\|_{z=0}}$
0-30	**0.26**/0.72	**0.28**/0.25	**0.08**/0.25	**0.2**/0.78	**0.12** /0.24	**2.20**/1.49
30-150	**0.44**/0.43	**0.56**/0.74	**0.25**/0.32	**0.2**/0.49	**0.28** /0.33	**1.60**/1.21
150-300	**0.57**/0.70	**0.76**/0.81	**0.43**/0.57	**0.2**/0.30	**0.47**/0.75	**1.21**/0.85
> 300	-/0.86	-/0.77	-/0.66	-/0.49	-/1.32	-/0.85

We choose to focus on 16 March, where the observations and the model results show good agreement (figure 3.8). The layer-mean potential temperature and the mixing ratio are rather well represented the first 200 km downstream of the sea ice edge. The potential temperature is slightly underestimated, but the difference decrease away from the sea ice edge. In contrast, the boundary layer height is slightly overestimated 170 km downstream of the sea ice edge, but in general captures the evolution well. The slight overestimation of the boundary layer height is consistent with a lower layer-mean potential temperature, as the heat fluxes must act to warm a deeper layer. Similar to observations, clouds form just off the sea ice edge. However, the cloud base touches the ground in our model, which is not observed. Both the observations and the model show the cloud base lifting away from the sea ice edge. The lower cloud base in the model is consistent with the lower temperatures, as lower temperatures are closer to saturation for a given mixing ratio according to Clausius-Clapeyron relationship.

The liquid water content reaches a maximum 20 km downstream off the sea ice edge and it decreases further downstream. The main sink of liquid water is precipitation, followed by entrainment. That the entrainment is so important for both the vapour and liquid water should raise some concern, as previous observations during field campaigns have shown that the turbulent transport of moisture through the top of the boundary layer is small, and in most cases only slightly negative. For instance, Brümmer (1996b) approximated the flux when no data was available to zero. As already discussed, the assumption of a dry free atmosphere might lead to an overestimation of the turbulent moisture flux across the top of the boundary layer.

However, Brümmer (1996b) further showed that the large scale subsidence decreases the moisture content through entraining dryer air. As this model does not take into account large scale subsidence, the turbulent transport of moisture content through the top of the ABL could compensate for not including this part. This could be the reason that the model is able to reproduce the moisture content in the ABL without including this effect.

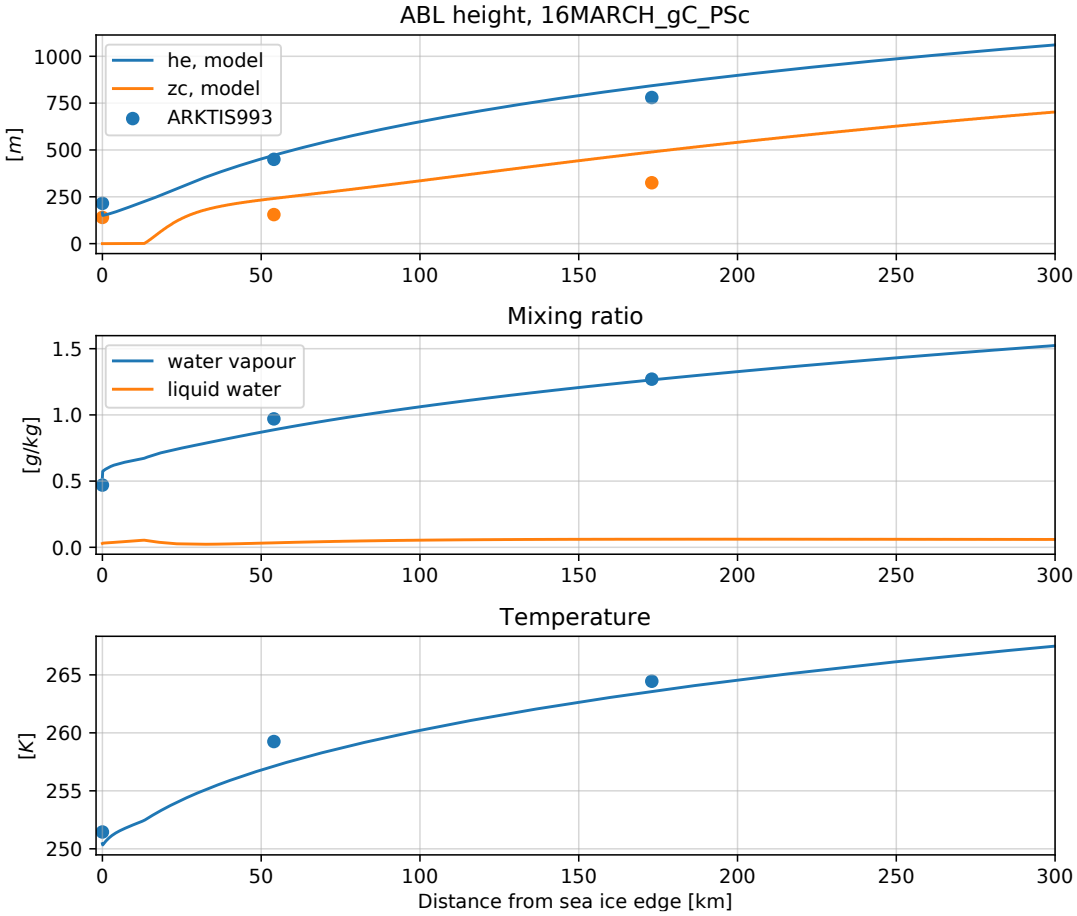

Figure 3.8: Top: comparing boundary layer height (he) and cloud base (zc) with observations (dots) for the 16 March. We have used the γ_θ from radiosondes as our stratification and increased the evaporation coefficient c_E.

3.2.2 Cold air outbreak over the Fram Strait 14/10/1991

Hartmann et al. (1997), used field measurements to document a case of roll convection during a CAO over the Fram Strait in October 1991. As the observations show nearly ideal mixing in equivalent potential temperature and cross-flow advection of only 1% compared to the along flow component, this is a good case for comparing observations to our mixed layer model. Table 3.4 shows the observed upstream initial conditions over the sea ice from the field campaign which we use to initialize the mixed layer model. We let the SST follow an *arctan*-function (figure 3.6), such that it increase rapidly from -1.8°C to 4.0°C, similar to what Hartmann et al. (1997) observed .

Table 3.4: Initial conditions for the cold air outbreak 14/10/1991. Adapted from Hartmann et al. (1997). We have decreased the ABL temperature by 1 K, which yields better results

Date 1991	h [m]	T [°C]	q [g/kg]	u [m/s]	ΔT_{inv} [K]	SST [°C]	γ_θ [K/m]
14/10	100	-16	0.7	10	-	-1.8/4.0	0.012

Further, Hartmann et al. (1997) concluded that heat and evaporation coefficients had to be $c_H = 1.2 \times 10^{-3}$ and $c_E = 1.1 \times 10^{-3}$ to close the budget. However, these coefficients provide too small evaporation rates, and clouds appear only at more than 250 km downstream, whereas observations show the clouds to appear immediately off the sea ice edge. We therefore adjust the coefficients to be $c_E = 2.0 \times 10^{-3}$ and $c_H = 1.5 \times 10^{-3}$, which also yielded better budget ratios during the ARKTIS1993 campaign.

We compare the model runs with the observations given in Hartmann et al. (1997) table 1, shown in figure 3.9. The ABL height and temperature is remarkably well represented in the model the first 150 km. However, the mixing ratio that the model shows after 300 km is observed already after 100 km, indicating that the rate of increase of the mixing ratio is too slow. However, except from a decrease in the mixing ratio around the sea ice edge, the change of the mixing ratio is well captured. In contrast, the fluxes are not well represented in the model, as both the latent heating and sensible heat flux are more than twice as high as the observations. It is therefore surprising that the other quantities are so well represented, as the surface fluxes are the main source for both the heat and the moisture of the boundary layer.

The heat fluxes in Hartmann et al. (1997) are calculated by looking at the change of liquid water and potential temperature over a distance Δy. Furthermore, Hartmann et al. (1997) assumed that there was no flux of heat or moisture through the top of the boundary layer, and that no moisture was lost to precipitation. These assumptions might impact both the sensible and latent heat flux calculations. Assuming that no moisture is lost from the ABL can affect the rate

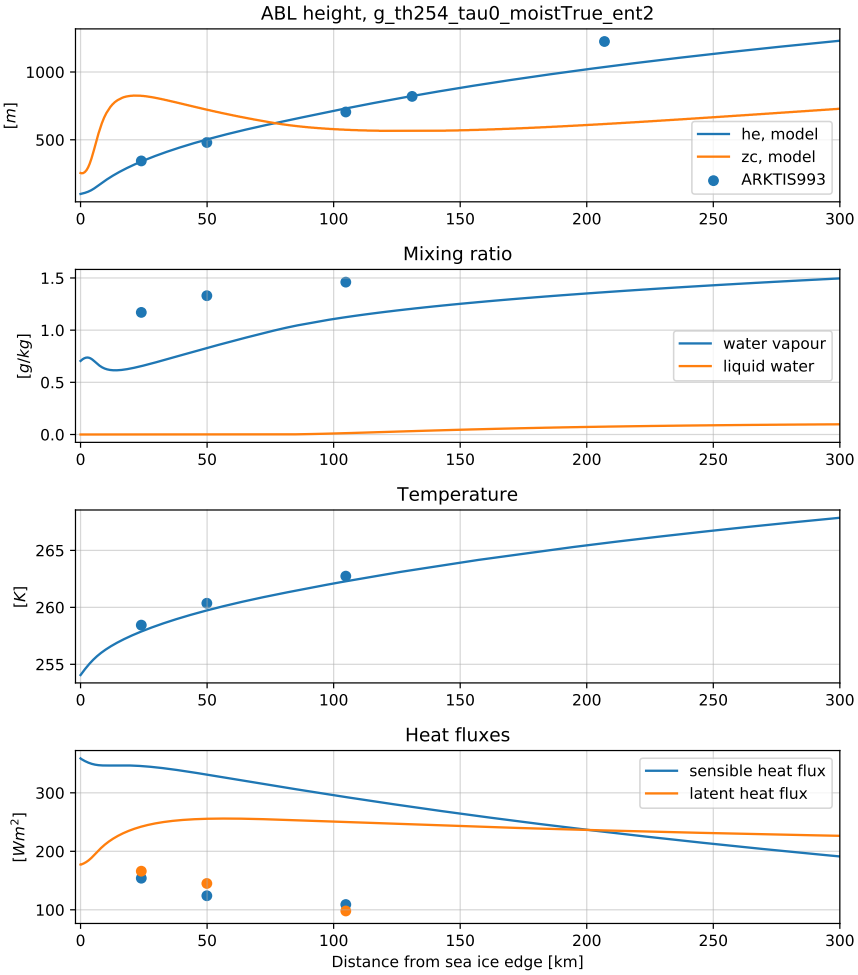

Figure 3.9: Comparisons with Hartmann et al. (1997), showing ABL height, mixing ratio, temperature and heat fluxes.

of heating (figure 3.10). The liquid water lost has already released latent heat. If this additional latent heat release is not accounted, the warming that occurred by this process will instead be attributed to the sensible heat flux, and consequently lead to an overestimation of the sensible heat flux. Given these arguments, we would expect the sensible heat flux to be underestimated in the model. However, both fluxes are overestimated compared to the observations. This could be because too much moisture is lost to the free atmosphere in the model (as previously discussed). More moisture lost to the free atmosphere would lead to a lower mixing ratio, which again act to enhance the latent heat flux. However, the cloud onset appear relatively late in the model compared to the observations. Hence, the effect of the latent heating is underestimated in our mixed layer model, and thus the sensible heat flux is higher. However, it is difficult to explore

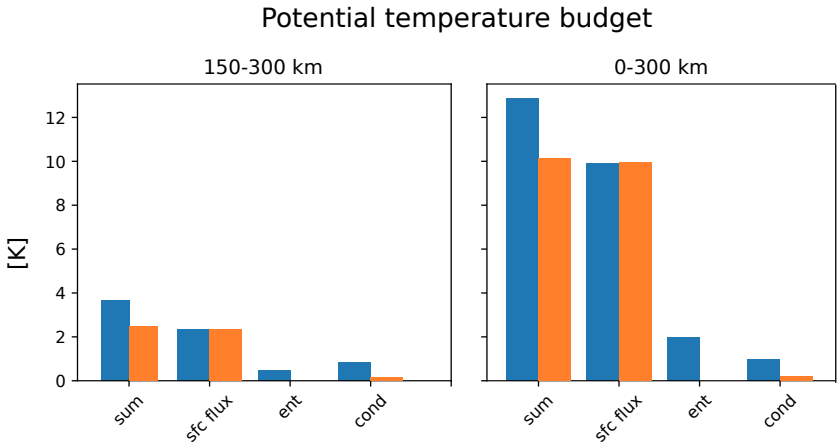

Figure 3.10: Left panel: Contributions from the different processes (sfc flux - sensible heat flux, ent - entrainment, cond - condensation) to the potential temperature budget between 150-300 km downstream of the sea ice edge. Right: same as left but for 0-300 km. Orange colour is the respective quantities calculated with the assumptions that no liquid water has escaped either to the free atmosphere or through precipitation, whereas the blue bar takes this into consideration.

the effect of the delayed cloud onset, as we have few observations to compare to downstream of $\sim$ 100 km. However, the fluxes remain higher than observations also after the cloud onset, indicating that the rates of condensation is too small.

The ABL height is accurately represented, but after it grows beyond 1000 m, it starts to deviate from the observations. The deviation could be related to the fact that γ_θ is only constant below 1000 m, while radiosonde data show a layer with lower stratification above, which would enhance the boundary layer growth. The change in stratification is not represented.

In the first 50 km away from the sea ice edge, observations show an increase in temperature of 0.09 K/km, whereas the model shows an increases of 0.11 K/km, a slight overestimation. In general, the model slightly overestimates the potential temperature increase. The overestimation of the temperature increase might be related to the surface sensible heat flux, as the turbulent heat fluxes are high compared to the observations. The entrainment rate is directly proportional to the surface sensible heat fluxes, and hence, an overestimation of the heat flux will also lead to an overestimation of the warming by entrainment.

An overestimation of the entrainment rate is further consistent with the underestimation of the mixing ratio we observe. Furthermore, the rate of increase of the mixing ratio is also underestimated. The model shows an increase of 0.0015 g kg^{-1} km^{-1} in the first 50 km downstream, which is $\sim$1/5 of the observed increase of 0.0073 g kg^{-1} km^{-1}. While observations show that

the rate of increase decreases further downstream, the rate of change in mixing ratio increases and becomes larger than the observed. The underestimation of the mixing ratio is most likely an effect of the assumption of entrainment, as decreasing the entrainment rate gives a mixing ratio more consistent with observations (not shown). However, this has also cause the ABL height to be underestimated the first 100 km downstream of the sea ice edge, and the surface fluxes increases relative to when entrainment is included. As the ABL height is very important in determining the layer for which the surface flux and the moisture flux should be mixed in, it is crucial to represent it accurately.

Comparing the model, figure 3.11, to figure 7 in Hartmann et al. (1997) shows that the cloud layer is much deeper in the observations than in the model. The onset of liquid water (and hence cloud) is just off the sea ice edge, whereas the modelled cloud onset is 71 km downstream. The observations indicate that the maximum liquid water content is ~ 0.65 g kg^{-1} km^{-1}, which is higher than the modelled maximum liquid water content of 0.45 g kg^{-1} km^{-1}. The liquid water exhibits similar behaviour, increasing from the cloud base and upward, but with more structure in the observations. The maximum in liquid water content is 300 km downstream in both the observations and in the model. However, the maximum is located closer to the ground in the observations. This is most likely due to the assumptions in the model. As the entrainment acts to decrease the moisture content equally in the entire water column, it will have more localized effects in nature and affect the top of the ABL more than at lower altitudes within the ABL. However, the mean liquid water content might not be very different between the model and observations.

Observations further show the contribution of latent heat release within the boundary layer cloud amount to 20% of the total heating of the boundary layer (Hartmann et al., 1997). The maximum heating of condensation in the layer is 33% of the total heating, at $\sim$ 300 km downstream, whereas the mean contribution of condensational heating is 9.4% of the total heating. 9.4% is rather low compared to the observed rates. However, as the cloud onset is later in the model than what is observed, it might be better to compare the condensational heating when we have a cloud present. The mean average contribution of the condensational heating to the total heating when a cloud is present, is 25.6%, which is closer to the estimate.

-

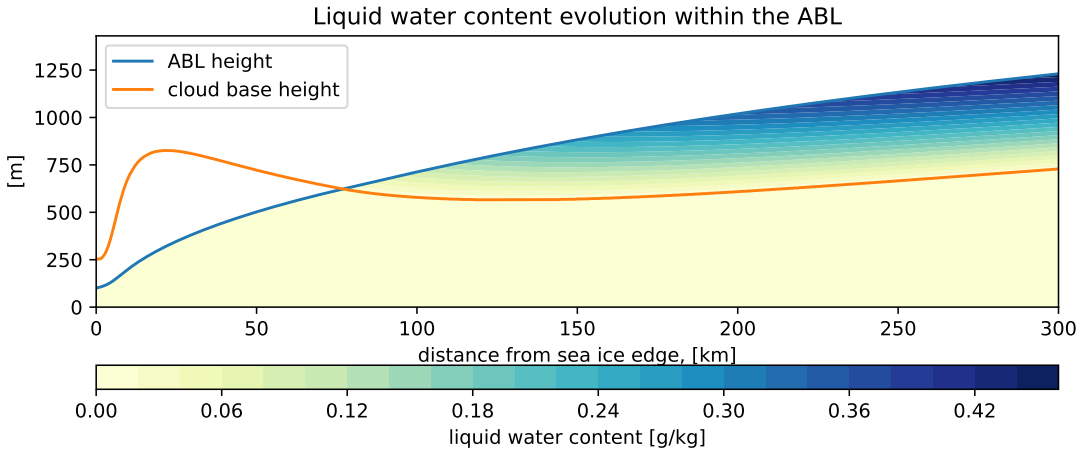

Figure 3.11: The structure of liquid water content. Liquid water content increases with height inside the cloud and becomes maximum just beneath the top of the ABL.

3.3 Sensitivity to different complexities

To understand the relative importance of the different processes and how they influence the structure of the ABL, we do experiments with various complexities. We vary the rate of entrainment through Υ, turn on and off the effects of moisture, and change the relaxation time scale, τ, of the ocean. A choice of $\tau = 0$ is equivalent to keeping the SST constant and hence decouple the atmosphere from the ocean. The larger the relaxation time scale, the more the ocean is allowed to change. Apart from the changes listed in table 3.5, the experiments have similar initial conditions as the reference run (section 3.1).

Table 3.5: Overview of experiments in the complex runs

ocean τ	0	1	2	5
entrainment Υ	0	0.1	0.2	
moisture	on	off		

When moisture is not included, the main factor controlling the boundary layer growth is entrainment (figure 3.14, right). Entrainment both act to warm the boundary layer and increase the boundary layer through the jump in potential temperature, $\Delta\theta$. Even if two boundary layers had the same potential temperature, if $\Delta\theta$ was larger than zero in one of them, it would act to increase the boundary layer height relative to the other where $\Delta\theta = 0$. By definition, $\Delta\theta$ is equal to zero when $\Upsilon = 0$, or entrainment turned off. Thus, the runs with the effect of entrainment have a higher boundary layer than those where entrainment is turned off.

However, the inclusion of moisture makes the effect of entrainment on the boundary layer height more complicated. Figure 3.14 shows that the growth of the boundary layer is no longer proportional to the entrainment rate. When we include moisture, we introduce latent heating as an additional source of heat to the ABL. Latent heating is dependent on the liquid water content of the ABL. Therefore, we first need to understand how entrainment affects the liquid water content in order to understand the growth of the ABL in the moist simulations.

The effect of entrainment in the moist runs is most noticeable in the total mixing ratio and cloud depth (figure 3.13a,d). Without entrainment ($\Upsilon = 0$) the only sink of moisture in the ABL is precipitation, and therefore the mixing ratio is higher when there is no entrainment. The increased mixing ratio is accompanied by a cloud base that extends further down (figure 3.13a), a higher precipitation rate, and an earlier onset of precipitation. Entrainment therefore seems to be a key parameter in controlling the moisture content of the boundary layer in this framework.

The increased cloud depth when entrainment is not included is consistent with enhanced latent heating (figure 3.13a). The layer-mean potential temperature increases rapidly when the

cloud base touches the ground (figure 3.13c). The enhanced warming rates are also reflected in the sensible heat flux, which starts decreasing at the same location (figure 3.13b). As the sensible heat flux associated with no entrainment is similar to the sensible heat flux to with entrainment included, we can attribute this difference to latent heating. However, the rapid growth of potential temperature is only sustained for a short distance, and it declines already after 50 km. The stagnation in the potential temperature growth may be explained by both smaller sensible heat fluxes and a stabilization of liquid water content (figure 3.12). Latent heating is dependent on a supply of liquid water. If the liquid water stops increasing, the potential temperature can no longer increase at the same rate. However, after 100 km, as the cloud layer lifts from the ground, the rate of change of potential temperature starts to increase again. This is also consistent with an increase of the sensible heat flux into the layer. The potential temperature for $\Upsilon = 0$ remains higher than for $\Upsilon > 0$ during the entire model domain, indicating that heating by condensation can dominate over heating by entrainment.

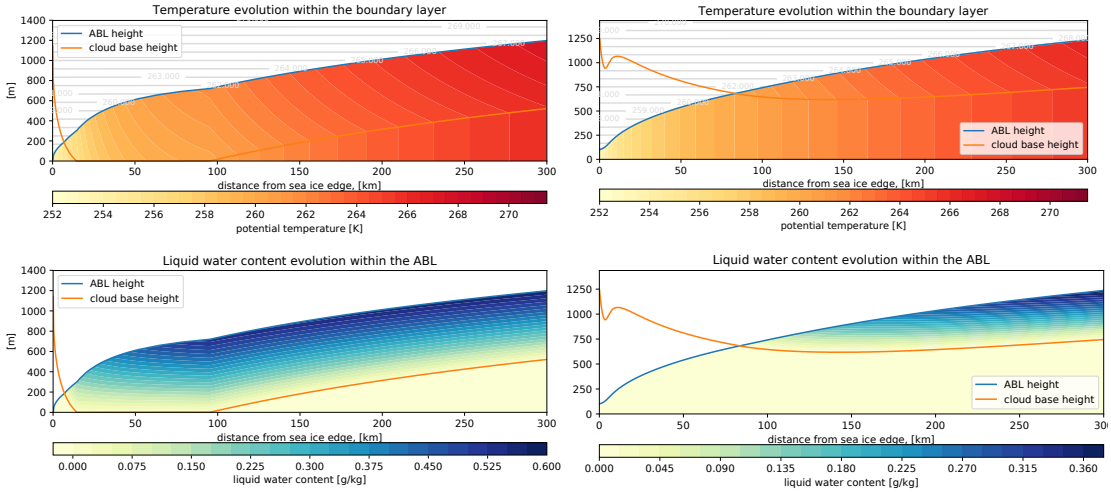

Figure 3.12: Upper left panel: Potential temperature structure for $\Upsilon = 0$. Lower left panel: Liquid water content for Υ. Right: same as left, but for $\Upsilon = 0.2$. Not that the temperature scale is similar, but that the liquid water content scales are different.

Latent heating has the potential to be important for the boundary layer growth. At the same time as the potential temperature associated with $\Upsilon = 0$ starts increasing rapidly, the boundary layer height also starts to increase (figure 3.13a, structure of the potential temperature in figure 3.12). The boundary layer growth seem to follow the potential temperature increase. However, whereas the potential temperature for $\Upsilon = 0$ was consistently higher than for $\Upsilon > 0$, this is not the case for the boundary layer height. The boundary layer height for $\Upsilon = 0.2$ is larger than the two others 150 km downstream, despite the lower potential temperatures in the layer. The higher boundary layer for $\Upsilon = 0.2$ might be attributed to the jump in potential temperature, $\Delta\theta$.

If $\Delta\theta$ is larger than the difference between the temperatures associated with $\Upsilon = 0$ and $\Upsilon = 0.2$ at the top of the ABL, $\Delta\theta$ will lead to a higher boundary layer height for $\Upsilon = 0.2$. However, $\Upsilon = 0.1$ is associated with the lowest boundary layer height of all the three runs. This indicates that $\Delta\theta$ is not large enough to compensate for the lower temperature for $\Upsilon = 0.1$. Furthermore, despite the lower entrainment rate, the mixing ratio and cloud layer do not differ significantly between $\Upsilon = 0.2$ and $\Upsilon = 0.1$. Therefore, the latent heating rate is lower for $\Upsilon = 0.1$ than for $\Upsilon = 0$. When moisture is included, latent heating can act to enhance the boundary layer growth. Latent heating has the potential to be more important than entrainment, but only when the moisture content is high and increasing. Otherwise, entrainment is generally the main factor for controlling the boundary layer growth.

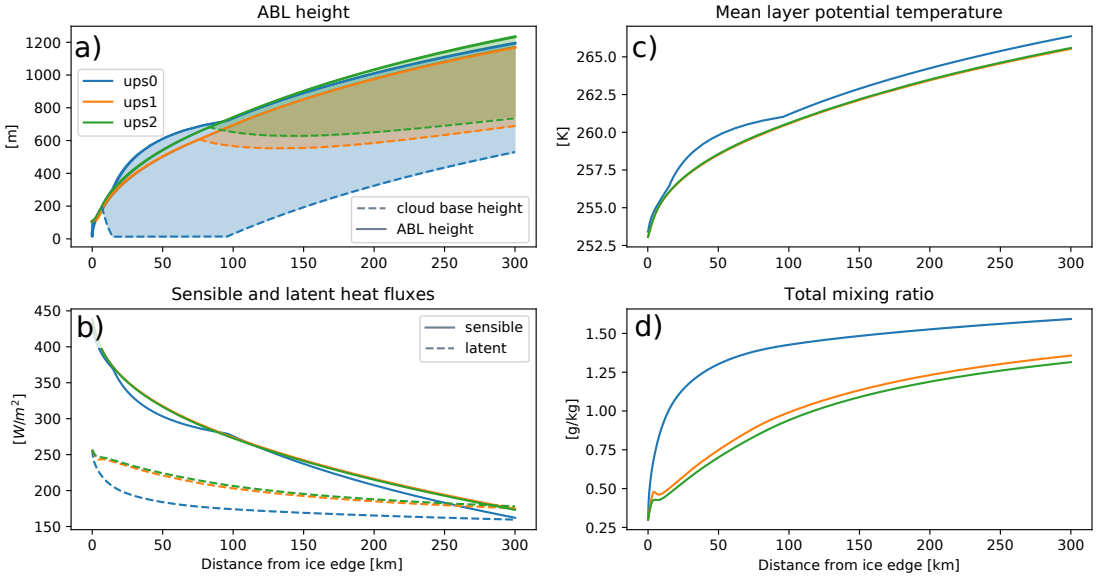

Figure 3.13: The effect of different entrainment rates, Υ (ups), for the moist, uncoupled runs, on the boundary layer height, sensible and latent heat fluxes, mean layer potential temperature, and total mixing ratio.

In addition to the moisture, the boundary layer height is also sensitive to the coupling to the ocean (figure 3.14). When the relaxation time scale increases, the boundary layer height decreases. This can be understood by looking at the domain-integrated sensible heat flux (figure 3.15). The integrated heat fluxes to the atmosphere is largest when the ocean is decoupled. The flux decreases with increasing relaxation time scale. However, the differences in the boundary layer height differ by less than 50 m at 300 km downstream. Given that the coupling has a relatively small effect can be attributed that even if it has been a significant heat loss of the ocean, this has been distributed over the mixed layer of 50 m. Thus, the ocean has cooled by only 0.1 K, which has a marginal impact on the temperature contrast between the atmosphere

and the ocean, and the heat fluxes are still large. .

The domain-integrated sensible heat flux to the atmosphere shows a strong dependence on both the inclusion of moisture and the rate of entrainment in addition to the coupling (figure 3.15). When moisture is turned off, the domain-integrated sensible heat flux is smallest when $\Upsilon = 0.2$, which is an effect of the warming by entrainment. However, when moisture is included, it has the ability to decrease the integrated sensible heat flux in two ways; to cool the ocean through the latent heat flux, and to increase the potential temperature in the layer through latent heating. As the latent heat flux is lower for no entrainment, the ocean cools less, and hence the air-sea temperature contrast is larger. Thus, the lower integrated heat flux in this experiment when $\tau > 0$, can be attributed to the higher rates of latent heating which lead to higher potential temperatures.

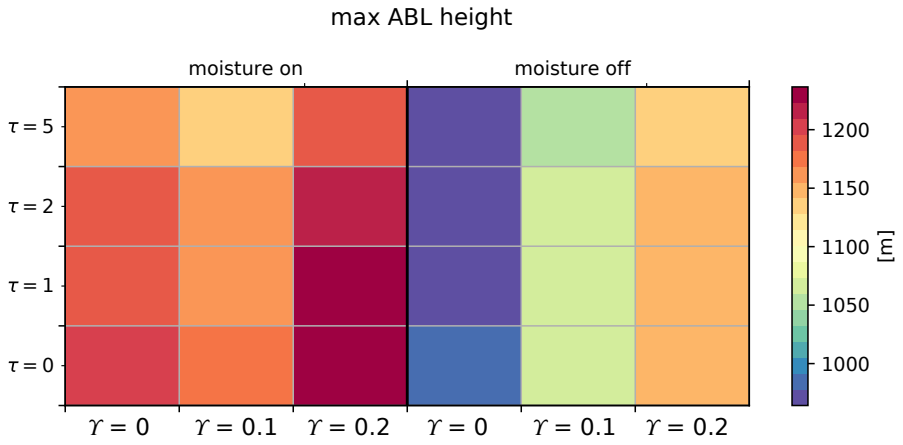

Figure 3.14: Boundary layer height maximum. The y-axis represents the different relaxation time scales and hence the strength of coupling to the ocean, and the x-axis is the different entrainment velocities.

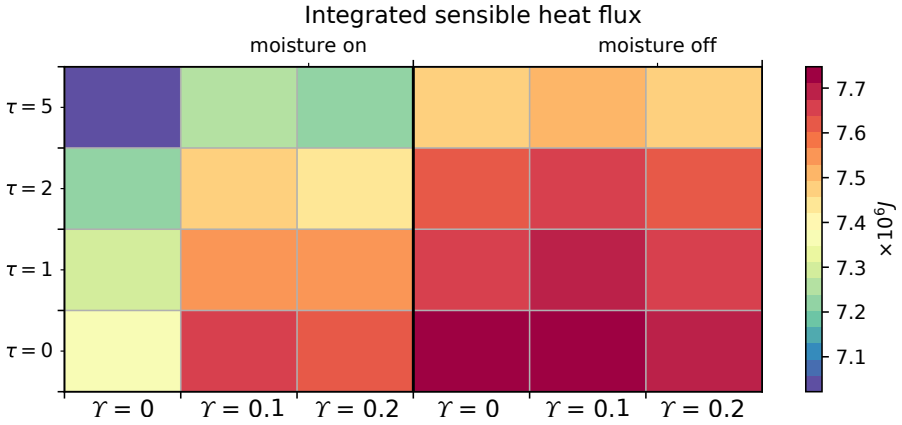

Figure 3.15: Integrated sensible heat flux for the different complexities. Otherwise same as figure 3.14

3.4 Sensitivity to initial conditions

After identifying the pertinent processes in the model, we now investigate how sensitive the results are to the initial conditions. We investigate the influence of wind speed, temperature and mixing ratio, as well as γ_θ and the SST distribution. We also aim to obtain a better understanding of the role of the ocean by checking the initial mixed layer depth and the ocean stratification.

3.4.1 Wind speed

To investigate the sensitivity to the wind speed, we initialize the model with $u = 5$ m/s, $u = 10$ m/s, and $u = 15$ m/s. As both the surface fluxes and the entrainment scale directly with the wind speed, the high wind case also has the highest fluxes (figure 3.16d). However, even though the fluxes are higher with high wind speed, the individual air columns are advected faster through our domain and are therefore exposed to the higher fluxes for a shorter period. Conversely, air columns advected with low wind speed are exposed to lower fluxes, but for a longer period. This means that the same amount of heat is added to the different air columns. Hence, we expect the potential temperature and boundary layer height to be identical for different wind speeds (figure 3.16a,c).

For the mixing ratio, however, the simulations deviate in the moisture content after 150 km downstream. The variations between the runs are first noticeable in the precipitation (figure 3.16b). The precipitation rate is lower for the low wind speed, and vice versa. Consistent with the lower precipitation rate, the moisture content is also lower. Furthermore, there is a difference in the cloud base height (figure 3.16a). The cloud base height starts lifting in the low wind speed case relative to the high wind speed case at 150 km downstream, which is consistent with the lower moisture content and lower precipitation rates.

The mixing ratio's dependence on wind speed is most likely related to the parameterization of the precipitation rate, which does not scale with wind speed in contrast to the moisture flux and entrainment. The precipitation rate is only a function of the liquid water content and the autoconversion rate, which is constant. Hence, as the precipitation rate initially is the same for different wind speeds, the slow air column will have more moisture precipitating out as it is advected slower. As more moisture precipitates out, the mixing ratio decreases, and eventually the cloud base starts lifting and the precipitation rate decreases further downstream.

To confirm that precipitation is enhanced in the lower wind speed, we look at the budget ratios, introduced in section 2.5.4 and in section 3.2.1. The ratio of evaporation to precipitation and the ratio of condensation to precipitation both increase with decreasing wind speed. 50 km to 300 km downstream, the ratio of precipitation to evaporation is 0.2, 0.26, and 0.37 for

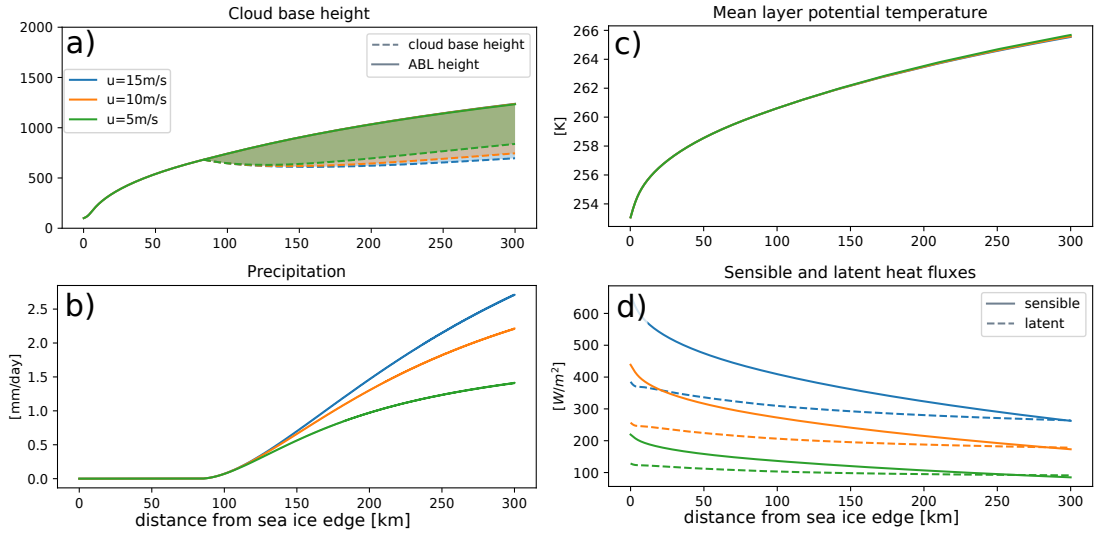

Figure 3.16: Cloud base height, layer-mean potential temperature, precipitation and the sensible and latent heat flux for the different wind speeds.

$u = 15$ m/s, $u = 10$ m/s, and $u = 5$ m/s, respectively. The increasing ratios indicate that a larger fraction of the moisture is lost through precipitation for the low wind speed. This is also seen in the mixing ratio budgets, which show that even though the increase in mixing ratio is smaller for the low wind speed, more moisture is lost through precipitation (figure 3.17).

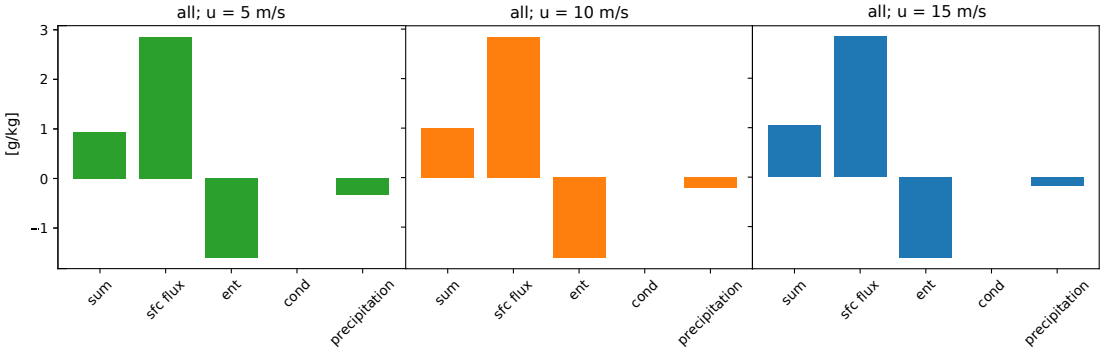

Figure 3.17: Contributions to the total mixing ratio budget for the different wind speeds. 'all' indicates that the budget for the entire fetch. The x-axis are the different processes and their relative contributions. Sum is the total contribution, sfc flux the contribution from the surface flux, in this case evaporation, ent the entrainment, cond the condensation, which is not applicable when we look at the mixing ratio as the mixing ratio looks at both moisture in vapour and liquid form, and finally precipitation is the moisture lost through precipitation.

The sensitivity to the wind speed might be important for the atmospheric water cycle during CAOs. If the wind speed during a CAO is low, most of the water might precipitate out over the ocean compared to a CAO with stronger winds. Stronger winds might therefore bring precipitation further downstream, before the CAO intersects with topography and leading to even higher precipitation rates.

Lastly, we investigate the effect of the coupling. As the ocean relaxation time scale is independent of the wind speed, the main effect of the wind speed is the magnitude of the fluxes. The ocean cools more in the high wind speed cases, as the turbulent heat flux scales directly with the wind speed. In addition, the evaporation rate increases, which in turn acts to increase the salinity in the cases of high wind.

When we increase the coupling through the relaxation time scale, both the ABL and the OML budgets become more sensitive to the magnitude of the wind speed. The ocean integrated heat loss varies both with wind speed and with the relaxation time scale. For $\tau = 5$, the maximum heat loss varies between 1 to $8 \times 10^{11} J$ for the different wind speeds, where the maximum heat is lost for $u = 15$ m/s. The boundary layer height is more dependent on the wind speed when the relaxation time scale is large, but the overall variations are small. The largest variations are seen in the onset of clouds, which happen later when $\tau = 5$ for the high winds compared to the low winds. The latent heat flux is very sensitive to the SST, as the Clausius-Clapeyron for SST yields an exponential relation for how the saturation mixing ratio depends on the temperature. As the ocean cools more for high wind speeds, the evaporation decreases in the coupled experiment to the uncoupled. Lower evaporation rates are consistent with a lower moisture content in the ABL, and hence also lower precipitation rates. This indicates that the ABL is more sensitive to the wind speed when the ocean is coupled to the atmosphere. However, the maximum heat fluxes differ by at most 10% between $\tau = 0$ and $\tau = 5$ for $u = 15$ m/s.

Stage (1983) used a mixed layer model with moisture to investigate the effect of the wind speed in a similar setup as presented here. The model was that of Stage and Businger (1981), and included a more sophisticated formulation of entrainment than in our mixed layer model, which also accounted for the effects of radiation. Sensitivity studies with this model showed that radiation had a tendency to decrease θ and promote entrainment, which further acted to decrease q_m. Unlike the effect of entrainment and surface fluxes, the effect of radiation does not scale with wind speed (Stage and Businger, 1981). Hence, in weak wind cases, the radiation dominates the effect of the surface fluxes, whereas the opposite is true for the high wind speed case. Similarly to our model, the moisture and heat added by surface fluxes scaled directly with the wind speed. Stage and Businger (1981) showed that because high wind speed cases were dominated by surface fluxes and low winds by radiation, the boundary layer structure at a given fetch was less sensitive to the wind speed during high than low winds. This is not seen in our

model as it does not include the effect of radiation. Thus, if we had used a more complicated expression for our entrainment velocity, our solutions could have been more sensitive to the wind speeds, and as the effect of radiation is to reduce both the temperature and humidity, we would expect the humidity to be even lower in the low wind speed case. This might have lead to a more rapid decrease in the cloud thickness and hence lower precipitation rates.

Differences might also arise for the parameterization of the surface fluxes. Whereas we have used a simple bulk formula in this model, Renfrew and King (2000) used a more sophisticated routine based on Monin-Obukhov theory. Renfrew and King (2000) model might therefore yield more accurate flux calculations. Experiments with their model[1] show that in contrast to our results, the temperature increase is not identical for the different wind speeds. The experiment with the low wind speed warmed the most. If these estimates are correct, it might imply a delay in cloud onset for the low wind speed, as the temperature increases faster away from the sea ice edge. A delay in the cloud onset could possibly lead to a shallower cloud base and thus lower latent heating rates further downstream. This would act to reduce the overall temperature difference between the experiment with the high and low wind speed. However, if the cloud base does not change significantly in the low wind speed case, we would still expect more moisture to precipitate out of the ABL compared to the higher wind speed cases.

[1] Available from `https://archive.uea.ac.uk/~e046/resources/cibl.htm`, accessed June 3, 2019

3.4.2 Atmospheric stability

When we compare results from our model to observations (section 3.2.1), the structure of the ABL and the boundary layer height is very sensitive to the ambient stability, γ_θ. We therefore want to explore this sensitivity further. For simplicity, we keep the ocean static, and besides changing the stability, the initial values are identical to the reference run (section 3.1). We vary γ_θ similarly to Renfrew and King (2000), between $\gamma_\theta = 6.2$ K km^{-1}, $\gamma_\theta = 9.8$ K km^{-1} and $\gamma_\theta = 12$ K km^{-1}.

The boundary layer height is mostly controlled by the stability - the less stable the inversion over the boundary layer, the more vigorous the boundary layer growth (figure 3.19 a). Further, the boundary layer height affects both the potential temperature and the moisture content of the ABL (figure 3.19 b,d). If the boundary layer is shallow, both the heat and moisture originating from surface fluxes are distributed over a shallower layer, indicating both a higher potential temperature and higher mixing ratio in a shallow boundary layer.

Interestingly, even though the moisture content is varies for the different stabilities, the cloud onset happens almost at the exact same location (figure 3.19a). However, the cloud base height is higher for the least stable boundary layer. This can be explained when we consider that the mixing ratio is lower for low stability (figure 3.19d). The temperature decreases according to the dry adiabatic lapse rate beneath the cloud base, and because of the lower mixing ratio, condensation happens higher above the ground. The lower potential temperature for lower stabilities also aids the layer to saturation at lower mixing ratios.

Furthermore, the cloud depth is different (figure 3.19a). The lower the stability, the deeper the cloud layer. The deeper cloud layer is associated with higher liquid water content and therefore also higher latent heating rates (figure 3.18). Thus, the importance of the latent heating increases with the decreasing stability. However, despite the increased relative importance of the latent heating, the additional heat supply by condensation is never sufficient to compensate for that the surface fluxes have to be distributed over a deeper layer. This is in contrast to when we varied the entrainment rate in section 3.3, but it is important to note that the variation in the boundary layer height is much larger here than when we varied the entrainment rate. The low stability is therefore associated with lower potential temperature and mixing ratio.

The results after 50 km are similar to what Renfrew and King (2000) found in their simple model of the convective boundary layer. The boundary layer height varies between 568 m and 812 m in our mixed layer model for the dry case, whereas for Renfrew and King (2000), the boundary layer height varies between 575 m and 800 m. Including moisture has no effect after 50 km as condensation has not been reached yet. The small differences between the two models might arise from slight differences in the calculations of the sensible heat fluxes, as our model is

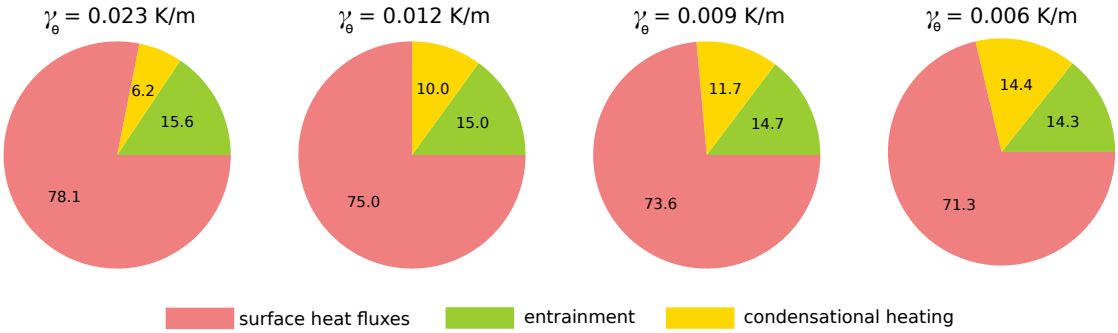

Figure 3.18: Contribution of the different heating terms (in %) to the heat budget for different stabilities γ_θ and for $\Upsilon = 0.2$ and moisture on.

based on a simple bulk formula whereas their model is based on Monin-Obukhov theory. Furthermore, there is a difference in the calculations of $\Delta\theta$. Renfrew and King (2000) have a dry mixed layer model, and hence $\Delta\theta$ can be solved analytically. In our case, $\Delta\theta$ has to be diagnosed numerically. Moreover, after 50 km, the potential temperature in the dry case varies between 257.3 K to 258.2 K, which is also similar to the finding by Renfrew and King (2000).

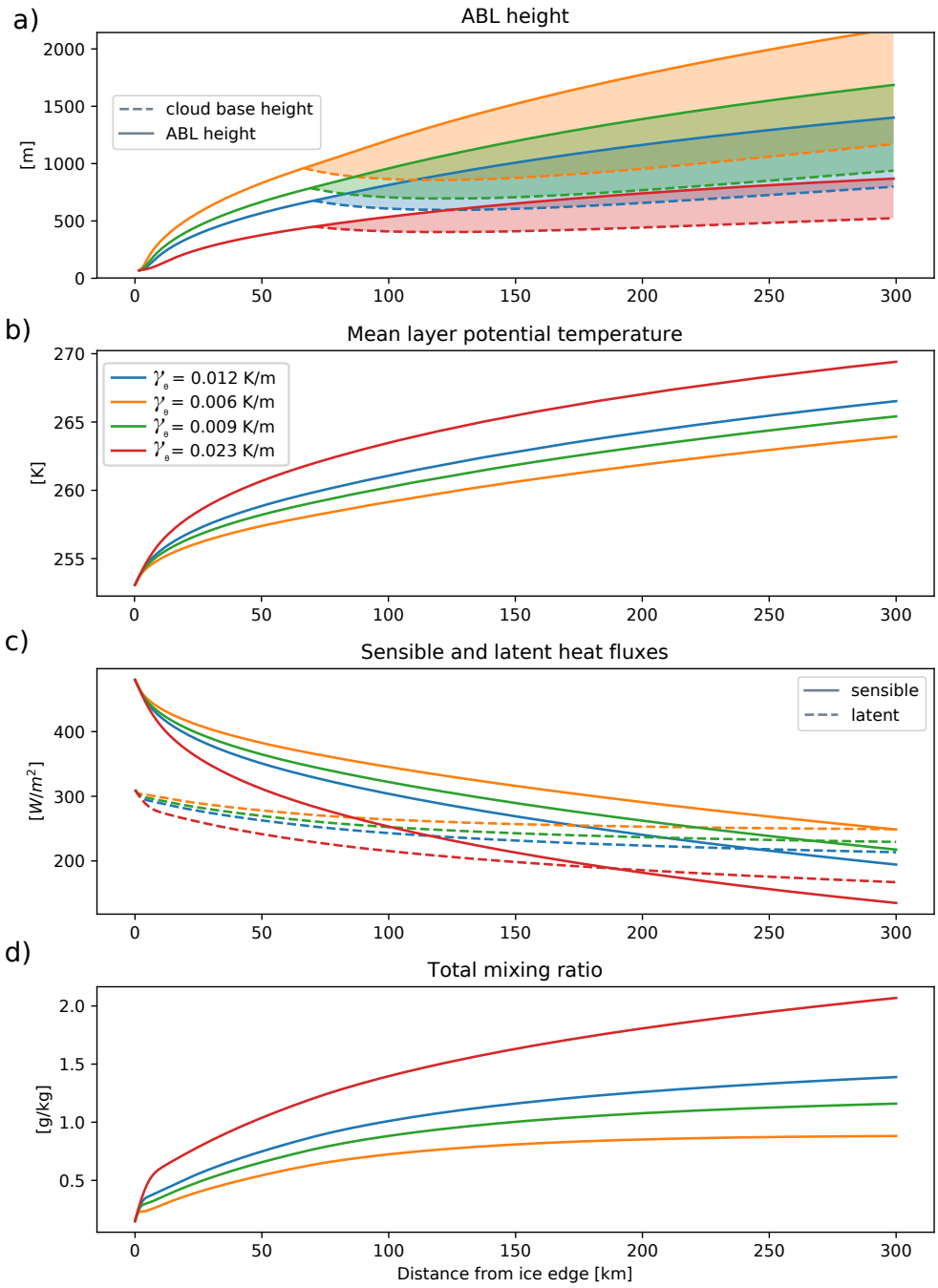

Figure 3.19: ABL height and cloud base height, layer-mean potential temperature, sensible and latent heat flux, and total mixing ratio for different stabilities.

3.4.3 Air temperature and humidity

We change the initial temperature and humidity content to see how the ABL structure is affected by these quantities, as listed in table 3.6. Otherwise, the other initial conditions are similar to the reference run (section 3.1).

Table 3.6: Initial conditions for all the different combinations of the experiments. We form abbreviations for the different temperature and humidity combinations, i.e. TH243q2 is the combination of $\theta = 243$ K and q_m=0.2 g/kg.

θ [K]	243	248	253	258
q_m [g/kg]	0	0.1	0.2	
Υ	0	0.1	0.2	

Varying the initial moisture content has relatively little effect when entrainment is turned on ($\Upsilon > 0$). If the initial moisture content is high, more moisture is lost to the free atmosphere, and hence the solutions differ little downstream (not shown). The cloud onset for the different initial moisture occurs and the same initial temperature happen within 10 km of each other. However, when entrainment is turned off ($\Upsilon = 0$) the solutions become more sensitive to the initial moisture content. The onsets of clouds differ more in the no entrainment runs than when entrainment is turned on. Entrainment delays the onset of clouds mainly by acting as a sink of moisture, but also by heating the boundary layer from above. Furthermore, turning off the entrainment has a tendency to make the cloud layer occupy the entire depth of the ABL. In contrast, when entrainment is turned on, the cloud layer occupies the entire depth of the ABL only in the coldest and moistest (TH243q2) run for a brief distance. Differences in cloud onset and cloud depths are associated with differences in precipitation. The precipitation and liquid water content seem to be the most sensitive parameters to the initial moisture content.

Varying the initial temperature appears to be more important than varying the initial moisture content for saturation with fetch. When the air is cold, the initial moisture content is closer to saturation, because saturation is determined from the Clausius-Clapeyron relationship (figure 3.20), and thus the air saturates earlier. In CAOs, clouds are often seen forming just off the sea ice edge (Brümmer, 1996a). This behaviour can be recreated in the model if the initial air is very cold.

Different initial temperatures are also associated with different heat fluxes. Heat fluxes are proportional to the air-sea temperature contrast, and, consequently, the cold run has a higher sensible heat flux. The more intense fluxes enhance both the entrainment rate at the top of the boundary layer and the boundary layer growth (figure 3.21). The TH243q2 experiment satu-

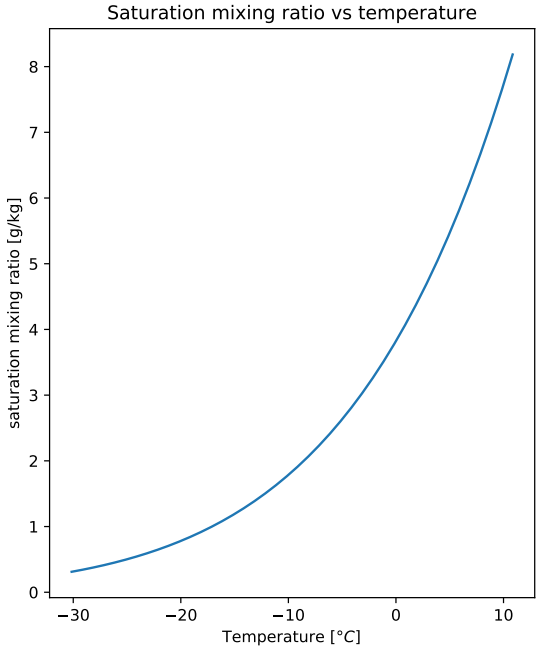

Figure 3.20: Saturation mixing ratio's dependence on temperature (Clausius-Clapeyron) at 1000 hPa.

rates first and at the lowest altitude for all the experiments. Combined also with the highest boundary layer height, TH243q2 has the deepest cloud layer, and also most intense precipitation. The relatively higher precipitation rates lead to a decrease in the total water content downstream.

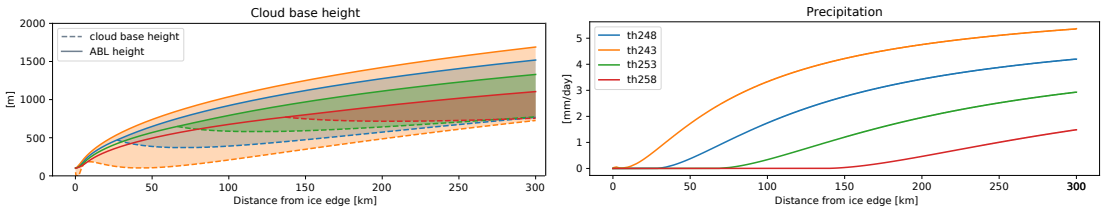

Figure 3.21: Precipitation, total water content and cloud base height for the different initial temperatures and $q_m = 0.2$ g/kg.

3.4.4 Ocean temperatures

We change the SST to see how it affects the boundary layer structure. We first choose the SST to be constant, and let it vary between -1 °C and 4°C. We also change the SST distribution to mimic that of a front (as in figure 3.6), and let it approach to its final value after 50 km (narrow, tN), 100 km (medium, tM) and 200 km (wide, tW).

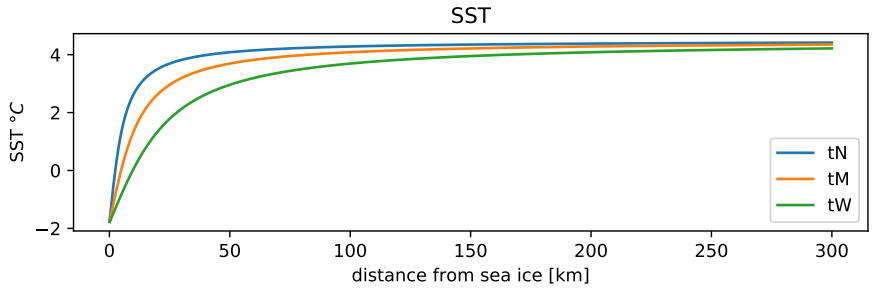

Figure 3.22: Different initial SST distributions.

For constant SST, we keep the difference between the air temperature and the sea surface to be the same for the different experiments to isolate the effect of a varying latent heat flux. The air temperature for SST 0°is 253 K, and the other air temperatures are adjusted accordingly. The latent heat flux is dependent on the SST through the Clausius-Clapeyron relationship (figure 3.20), such that a higher SST will result in a higher latent heat flux.

For the constant SST, the largest differences are observed in the mixing ratio. The higher SST is associated with a more intense latent heat flux, which adds more moisture to the ABL. Hence, the highest SST also has the highest mixing ratio. However, despite the relative high mixing ratio for the high SST, the cloud onset occurs later (figure 3.24). A later cloud onset is consistent with the discussion in section 3.4.3, because as the air temperature is higher, more moisture is needed for saturation. Changes in the latent heat flux and the associated moisture flux to the ABL are thus to a large extent compensated by the increasing air temperature in terms of saturation. If we had kept the air temperature constant and only varied the SST, the cloud base height and precipitation might have been more affected by the increased latent heating rate.

There are some variations in the domain-integrated sensible heat flux (not shown), which are small deviations that arise from the difference in densities between the warmer and the colder air. The difference amounts to at most 6 W/m^2, but is sustained during the entire run. Without this difference, the sensible heating differs by at most 0.5 W/m^2. Despite the low differences in the sensible heat flux, as we couple the atmosphere to the ocean, the ocean cools more for SST 4°C compared to SST -1°C. This is attributed to the higher latent heat rate for the higher

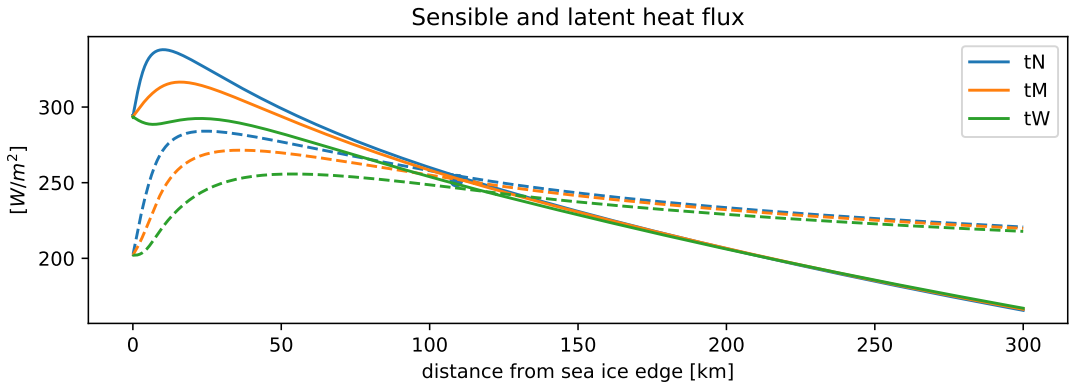

Figure 3.23: Distribution of sensible and latent heating for different widths of a SST front.

temperature.

Varying the SST distribution changes where the heat fluxes peak. For both tM and tN, the associated maxima occur some distance downstream of the sea ice edge (figure 3.23). For tW, however, the peak of the sensible occur just off the sea ice edge, but remain nearly constant the first 50 km downstream of the sea ice edge. The peak of the latent heat flux occur further downstream relative to the maximum in sensible heat fluxes. A shift in location for where the maxima of latent and sensible heat flux occur, is consistent with observations from a CAO in the Labrador Sea (Pagowski and Moore, 2001). Pagowski and Moore (2001) observed that the sensible heat flux was maximized just off the sea ice edge, whereas the latent heat flux occurred further downstream where the SST was higher. The shift in the latent heat flux were attributed to the nonlinear dependence of saturation vapour pressure. This indicates that in addition to the spatial distribution of the MIZ, the SST distribution and in particular how fast the temperature increase away from the sea ice edge is important for determining an accurate distribution of surface fluxes.

The wide SST front, tW, is always associated with lower turbulent heat fluxes compared to tN and tM. In tN, the SST increase rapidly away from the sea ice edge, and hence the air-sea temperature contrast increases downstream if the SST increases faster than the ABL temperature. In contrast, the SST and air temperature seem to decrease at approximately the same rate away from the sea ice edge, and hence, the fluxes remain nearly constant the first 50 km off the sea ice edge. The latent heat flux associated with tW peaks further downstream than tN and tM because the SST increases slower. However, as the SST approach the same values and the SST determines the upper bound on the latent heat flux Papritz et al. (2015), the domain-integrated latent heat fluxes will always be larger when the SST increases faster away from the sea ice edge.

Furthermore, the SST distribution is important for where the air first saturates. As the

SST increases most rapidly away from the sea ice for tN, tN is also associated with the highest latent heat flux. Therefore, tN has the highest moisture content and as well as the earliest onset of clouds. An early onset of clouds is consistent whit higher precipitation rates downstream.

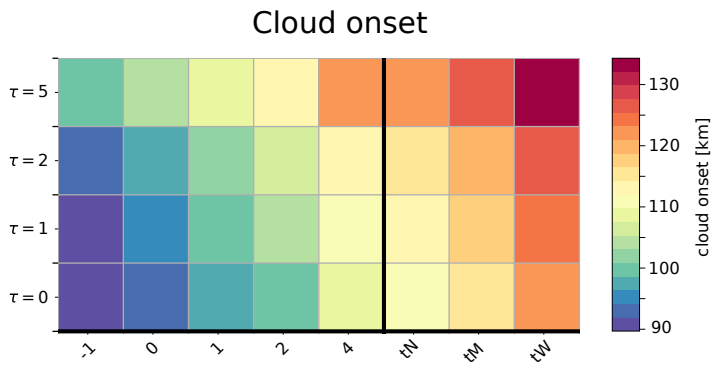

Figure 3.24: Different cloud onset for the different SST. x-axis represents the different distributions, where left side is constant SSTs and right is varying SSTs. Narrow, medium and wide indicates the width of the SST front as explained in the text. y-axis represents the different relaxation time scale and if moisture is included (upper panel) or not (lower panel).

3.4.5 Ocean stratification and mixed layer depth

So far we have focused mostly on varying the atmospheric aspects of CAOs. In this section, we explore the sensitivity of both the ABL and OML to the ocean stratification and different mixed layer depths. We start by using the reference profiles (figure 3.2) and change the initial mixed layer depths to be 10 m, 50 m, and 100 m (abbreviated mld10, mld50, and mld100, respectively). We then increase and decrease the salinity in the mixed layer to weaken and strengthen the stratification, respectively. The salinity of the mixed layer is varied between 34.5 g/kg, 34.6 g/kg, and 34.7 g/kg. We choose to change the stratification of the ocean through salinity because density changes are more sensitive to changes in salinity for cold water. In addition, we want to attribute the temperature change in the ocean mixed layer to the stratification and differences in mixed layer depth. Otherwise, the other initial values are equal to the reference run (section 3.1).

For $\tau = 1$ and an initial mixed layer salinity of 34.7 g/kg (indicating a weak stratification, as the overlying salinity is quite close to the salinity within the pycnocline, figure 3.25), the mixed layer deepens in all the cases. It deepens most for the shallow mixed layer. The deepest mixed layer in this case is 54 m, while it is 84 m for the initial mixed layer depth of 50 m and 117 m for the initial 100 m mixed layer depth. The variation in salinity is small, and for the different mixed layer depths it varies by ~ 0.001 g/kg. The salinity increase is largest for mld10. The temperature also decreases the most for mld10, as the cooling scales with the mixed layer depth. However, the temperature difference between the different mixed layer depths vary at most by 0.16 K, which is not significant enough to influence the ABL properties.

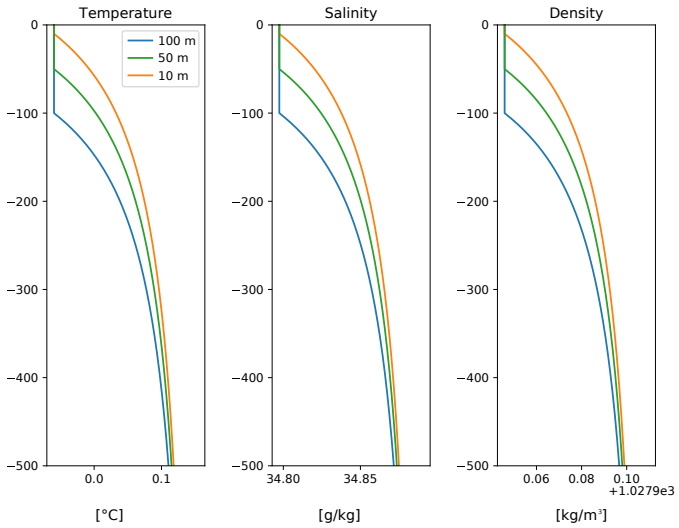

Figure 3.25: Initial temperature, salinity and density profiles for the different mixed layer depths for the weak-stratification case. The stratification is the same even though the mixed layer depths are different.

We further increase the stability of the water column by making the mixed layer fresher (34.7 g/kg), while keeping the same relaxation time scale. The ocean cools more when the stratification is strong, because the temperature is allowed to decrease more before the density stratification is eroded and mixing occurs. As the mixing both brings up heat from below the pycnocline and deepens the mixed layer to cool further, it has the potential to decrease the cooling of the mixed layer. The shallow mixed layer cool more than the deep mixed layer, and this difference amounts to 0.25 K.

However, if we also increase the relaxation time scale, to $\tau = 5$, the temperature difference between the deepest and the shallowest mixed layer increases to to 0.72 K (figure 3.26d). The shallowest mixed layer cools more than the deep mixed layer (figure 3.26d). The temperature in the shallowest mixed layer has decreased sufficiently to influence the latent heat flux. The latent heat flux differs by 70 W/m^2 throughout the entire domain (figure 3.26a). A higher latent heat flux is consistent with a higher moisture content and a deeper cloud layer for the initial mixed layer depth of 100 m (figure 3.26c), which is also consistent with higher precipitation rates (figures 3.26b). The increased moisture content also gives a slightly higher boundary layer height through latent heat release (figure 3.26).

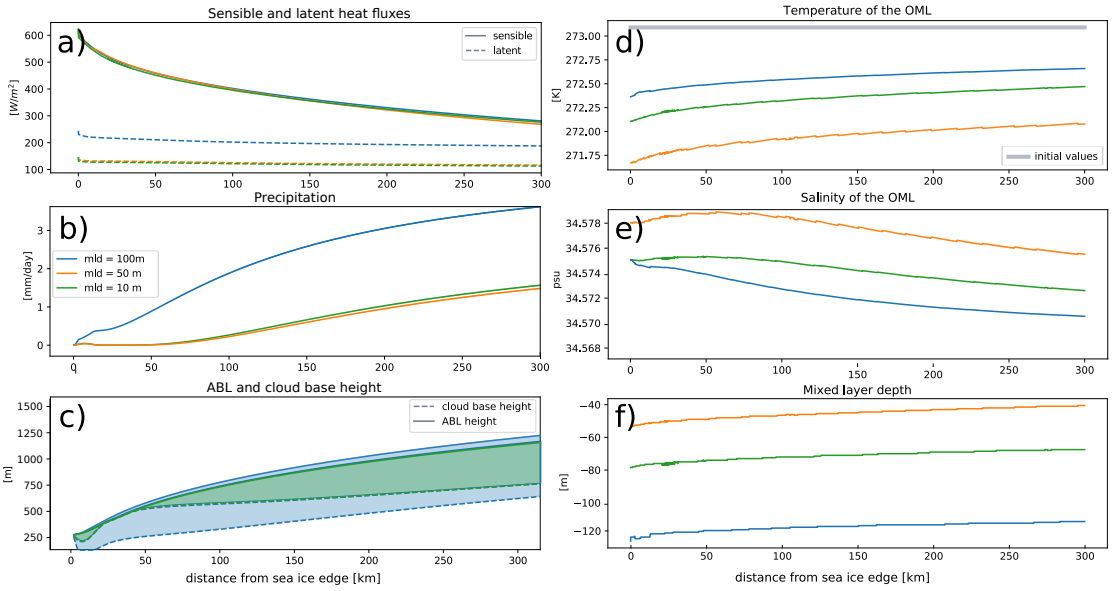

Figure 3.26: The ABL (left) and OML (right) properties for the different mixed layer depths with a strong stratification and $\tau = 5$.

The ocean stratification is therefore potentially important for the atmospheric feedback. If

the ocean is allowed to cool because of shallow mixed layer depths and strong stratification, it could potentially lower the latent heat flux, and hence also the precipitation and the cloud onset. However, how realistic such a setup is, remains an open question. Nevertheless, the experiments show that the moisture-related parameters are highly affected by the coupling, and hence neglecting moisture when investigating the effect of the coupling might yield an erroneous estimate of the coupling's importance.

3.5 Sensitivity to the width and shape of the marginal ice zone

Moore et al. (2015) showed that the location of the sea ice edge is important for ocean convection, and Pagowski and Moore (2001) showed that the atmospheric boundary layer modification over sea ice could impact the sensible heat fluxes hundreds of kilometres downstream. To test the influence of the width and shape of the MIZ, we conduct experiments with varying width and shapes of the MIZ, as listed in table 3.7. The MIZ width list in table 3.7 corresponds to the linear sea ice shape, and all the other sea ice distributions are adjusted accordingly such that the areas are equal (more details in section 2.4). Moreover, we change the size of our domain such that the total fetch over open water is the same, which is at least 1000 km. The relatively long fetch is to make sure that the solutions asymptote toward the end of the domain. Other than varying the sea ice cover, the initial values are the same as in the reference run (section 3.1).

Table 3.7: Overview of the MIZ experiments. The names in italics for the different sea ice distributions are the abbreviations that is used in the text (refer to figure 2.3 for illustrations of tanh, tanhU and tanhL).

shape of MIZ	tanh	tanh upper (*tanhU*)	tanh lower (*tanhL*)	linear (*lin*)	step
width of MIZ	45 km	90 km	180 km		
ocean τ (days)	0	1	2	5	
moisture	on	off			

We compare the sensible and latent heat fluxes for the tanh sea ice distribution for the different widths of the MIZ (figure 3.27). The more abrupt the transition between open water and fast ice, the higher the peak fluxes. However, the fluxes associated with the narrowest MIZ decrease faster with distance away from the sea ice. When the MIZ widens, the associated maximum in sensible heat flux is lower. However, the sensible heat fluxes associated with the wide MIZ are consistently higher, and the difference between the heat fluxes for the narrow and wide MIZ differ in the mean by 11 W/m^2 downstream of 150 km. There are smaller differences in the latent heat flux than in the sensible heat flux, which differ in the mean by 3 W/m^2 between the wide and narrow MIZ downstream of 150 km. The smaller difference in the latent heat flux than in the sensible heat flux indicates that it is the SST rather than the moisture content that sets the upper limit of the latent heat flux.

The different sea ice distributions do not have a profound impact on the ABL. For the different sea ice distributions, the solutions are similar 200 km downstream, and as the MIZ narrows, the solutions converge relatively fast (shown for the boundary layer height for the tanh sea ice distribution). The moist properties of the ABL seem to be more affected than the other parameters, such as the potential temperature and the boundary layer height. The latent heat flux converges relatively fast, but differences in the beginning of the domain for the different

widths (figure 3.27) could indicate that there is differences in total moisture content received to the atmosphere. That the properties of the ABL are relatively independent of the sea ice are consistent with the findings by Liu et al. (2006) who, using the non-hydrostatic and moist CReSS model, varied the sea ice concentrations, showed that the ABL properties seemed to have a relative short memory of the upstream sea ice concentrations. Rather, it seems like it is the total fetch over open water that are important for the structure of the atmospheric boundary layer.

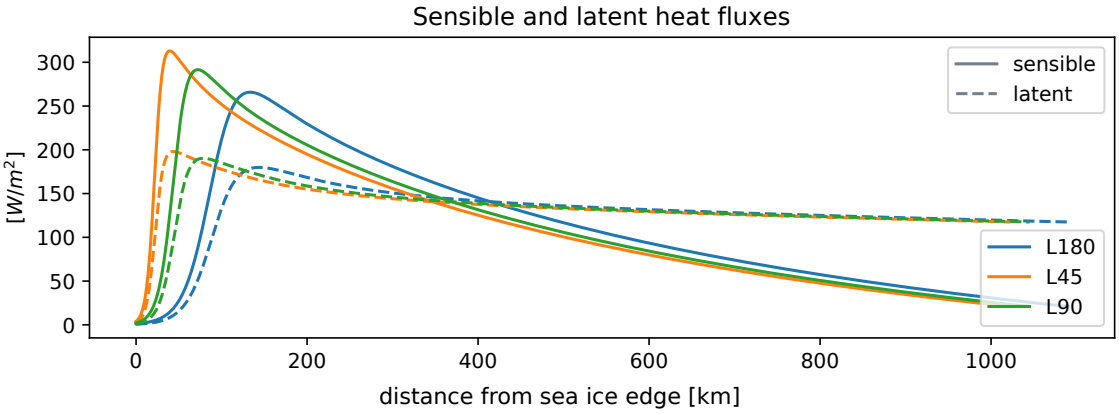

Figure 3.27: Sensible (solid) and latent (dashed) heat fluxes for $\tau = 0$, shape = tanh for the different widths of the MIZ.

In addition to the different widths of the MIZ, the shape of the MIZ also matters for the maximum heat fluxes (figure 3.28). The heat fluxes associated with the step function have the highest peaks, and as the sea ice distributions become smoother, where the tanhL distribution is the smoothest, the distributions' associated heat fluxes and their peaks become lower. However, the sea ice distributions which are associated with the highest peaks in heat fluxes also have a later onset of the heat fluxes. That the smooth sea ice distribution is associated with the lowest flux indicates that more boundary layer modification is allowed to take place over the sea ice, and hence the air-sea contrast weakens before the air column is exposed to open water, and thus the maximum fluxes are lower. Furthermore, in contrast to the fluxes for the different widths of the MIZ, the largest variations in the sensible heat fluxes are prior to the maxima.

These results differ slightly from those of Pagowski and Moore (2001). They investigated air-sea interaction and the structure of the ABL away and over the sea ice using the mesoscale forecast model MM5, and looked at the effect of a step function in sea ice concentration vs a parameterization of the MIZ consistent with observations. Pagowski and Moore (2001) showed that the air mass modification over the sea ice can result in a significant reduction of the fluxes several hundred kilometres downstream of the sea ice edge. The fluxes from the step-MIZ were consistently higher. However, the sea ice area might not be the same in their experiments. If

the sea ice area differs, so does the total fetch over open water. Consequently, the air that has passed over the sea ice with lower concentration will have been exposed to higher heat fluxes prior to it passing over open water, and therefore the air-sea temperature contrast is smaller. However, it highlights the importance of an accurate representation of the MIZ to get accurate fluxes.

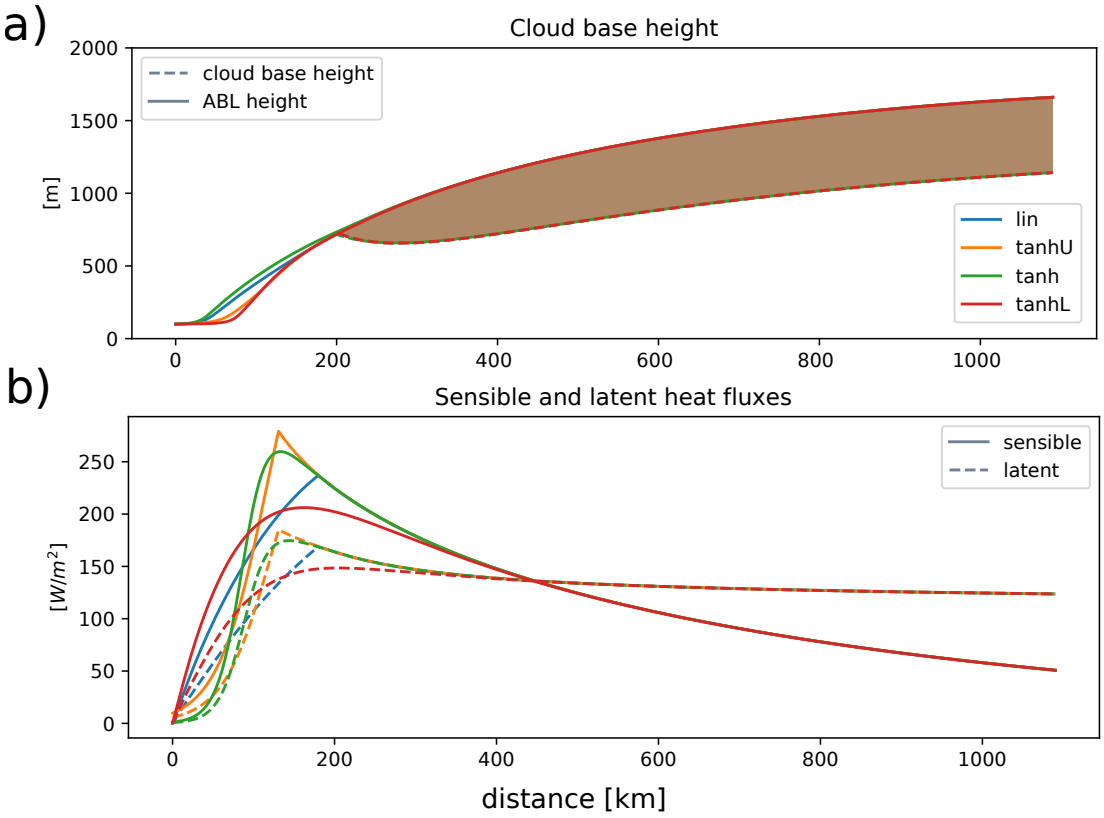

Figure 3.28: Sensible (solid) and latent (dashed) heat fluxes for $\tau = 0$, width = 180 km for the different shapes of the MIZ.

As indicated in figure 3.28, the sea ice distribution is most important for determining the maximum heat flux. If we also expand the analysis to include the other widths of the MIZ, moisture and ocean coupling ,it is still evident that the shape of the MIZ is the most important parameter (figure 3.29). Furthermore, the differences between the different sea ice distributions become larger as the MIZ widens. The step function is independent of the width of the MIZ, as it does not allow for any boundary layer modification to happen to the air column before it is exposed to open water regardless of the width. The opposite is true for the tanhL sea ice distribution, which as the MIZ widens, allows for more boundary layer modification over sea ice. The tanhL sea ice distribution is the only distribution that has the maximum fluxes appearing over the sea ice. The maximum heat fluxes associated with the wide tanhL occur over sea ice

concentration of 14%. This gives further insight to why the tanhL distribution is associated with the lowest heat fluxes.

Moisture and coupling play minor roles in decreasing the maximum heat fluxes. As the relaxation time scale increases, the maximum heat fluxes decrease. Moisture acts to increase the heat loss of the ocean through the latent heat flux, which lowers the air-sea contrast. The effect of moisture becomes more evident as the relaxation time scale increases. For the maximum oceanic heat loss, the pattern more or less follows the atmospheric maximum heat loss, but is more dependent on the relaxation time scale than on moisture. There is also a more visible effect of the moisture, because moisture induces additional oceanic heat loss through the latent heat flux.

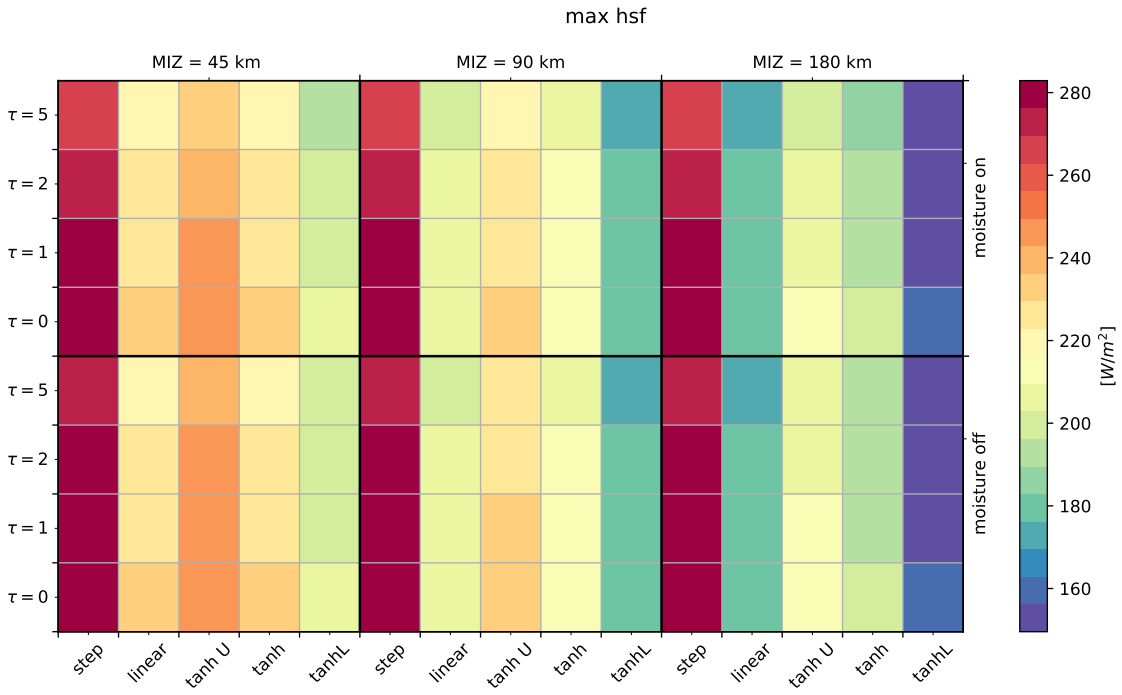

Figure 3.29: Maximum sensible heat flux for the different MIZ experiments

In contrast to the maximum heat fluxes, the domain-integrated sensible heat fluxes do not depend on either the shape or the width of the MIZ (figure 3.30). The integrated heat flux is most sensitive to the inclusion of moisture and the coupling to the ocean through the relaxation time scale. Moisture leads to lower integrated sensible heat fluxes, both through the enhanced cooling of the ocean (as previously discussed) and by warming the atmosphere through latent heating. Moisture has the largest effect on the integrated sensible heat flux, and the difference is large even when the ocean is decoupled. This indicates that the latent heating is relatively more important than the ocean coupling for determining the integrated sensible heat flux. Fur-

thermore, there are subtle differences within the integrated sensible heat flux, and for $\tau = 5$, the differences amount to 1700 J. However, this is insignificant when the total integrated sensible heat flux is on the order of 10^6 J, and is hence masked by the differences due to ocean coupling.

The domain-integrated oceanic heat loss does not show the same clear dependence on moisture as the integrated sensible heat flux (figure 3.31). Instead, it shows a stronger dependence on the relaxation time scale. The lowest integrated oceanic heat flux is when the relaxation time scale is lowest, $\tau = 1$. However, the moisture is important, and neglecting the latent heat flux on the ocean is equivalent to neglecting almost 40% of the oceanic heat loss. Similarly to the domain-integrated sensible heat flux, the total oceanic heat loss does not depend on neither the width nor the shape of the MIZ.

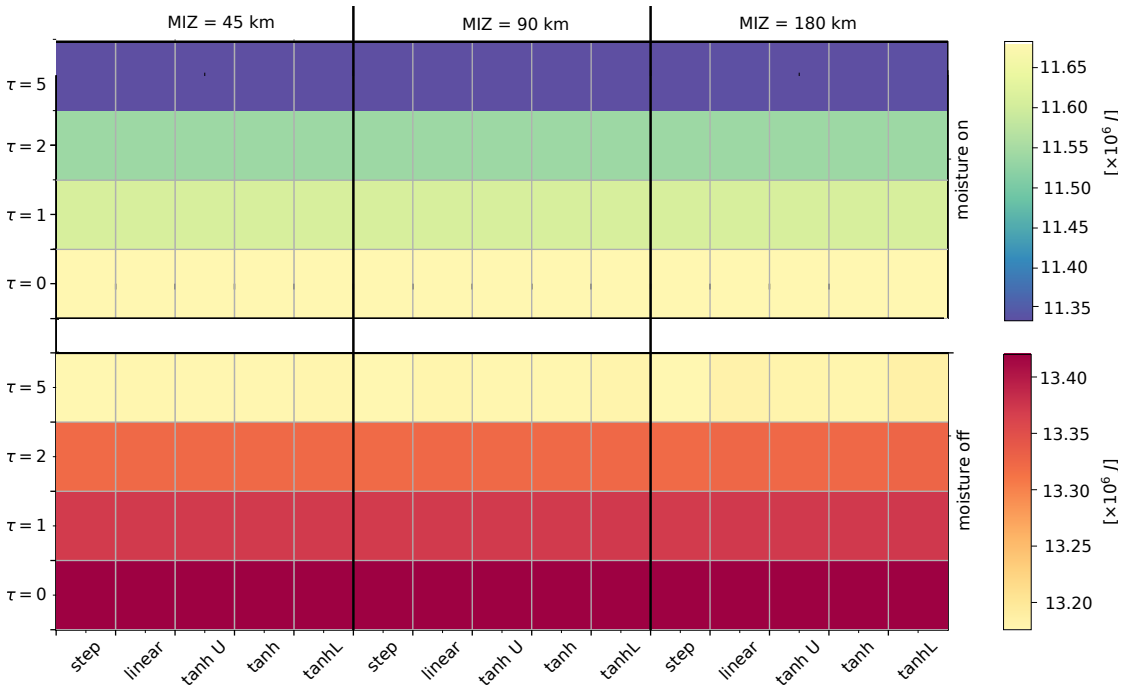

Figure 3.30: Integrated sensible heat flux for the different MIZ experiments. Note that two different colour scales are used and that variations within them are different.

The coupling affects the integrated sensible heat flux, but the ABL properties themselves are only weakly affected by the coupling. The largest difference in the boundary layer temperatures is 0.5 K 1000 km of the sea ice edge. That the ABL properties are independent of the coupling is similar to what Xue et al. (2002) found. Xue et al. (2002) attributed this to that the heat loss of the ocean is only a small fraction of the total oceanic heat content, and hence the mixed layer temperature of the ocean does not change enough to influence the sensible heat flux sub-

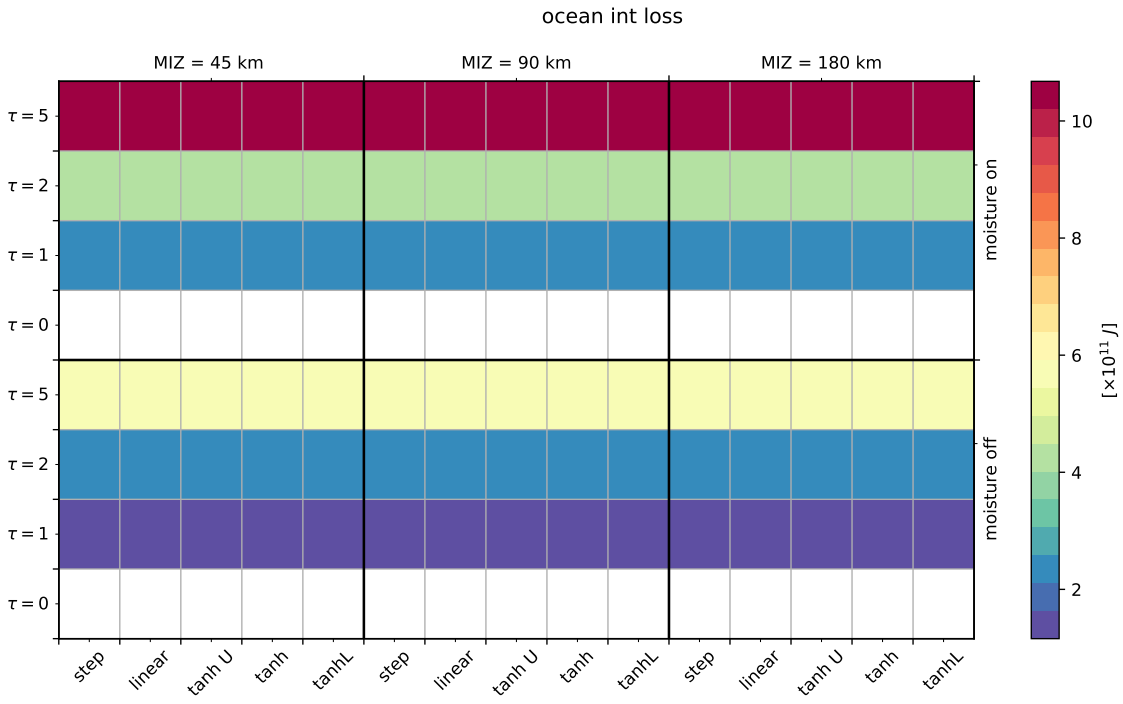

Figure 3.31: Integrated heat loss from the ocean for the different MIZ experiments.

stantially. In our case, the maximum oceanic heat loss accounts for 0.5% the total heat content in the oceanic mixed layer, however it is the main source of heat to the ABL, and accounts for nearly 80% of the observed warming.

For long relaxation time scales, the heat loss to the atmosphere is large enough to cause below freezing mixed-layer temperatures in our model. Based on how much the mixed layer has cooled below freezing, we are able to give an upper estimate of the sea ice production (details in section 2.5.6). These calculations show that in total over the 1000 km fetch, for the tanh sea ice distribution and with a relaxation time scale of $\tau = 5$, between 307 m and 421 m of sea ice has formed, where the narrow MIZ is associated with the highest sea ice production rates (figure 3.32a). The maximum sea ice thickness is 30 cm, which is high, but within the range compared to values observed in polynyas which ranges from 5 to 31 cm/day, and the turbulent heat fluxes are also within the observed range (Smith et al., 1990). Thus, as we consider a heat loss over 5 days, these results are not unrealistically high as they serve as an upper estimate of the sea ice production rates. The impact of 30 cm ice on the salinity flux and the mixed layer depth is substantial (figure 3.32b), as the mixed layer depth increases from 54 m to over 100 m (figure 3.32c)

Considering the large sea ice formation rate in the cases of $\tau = 5$, and the potential impact

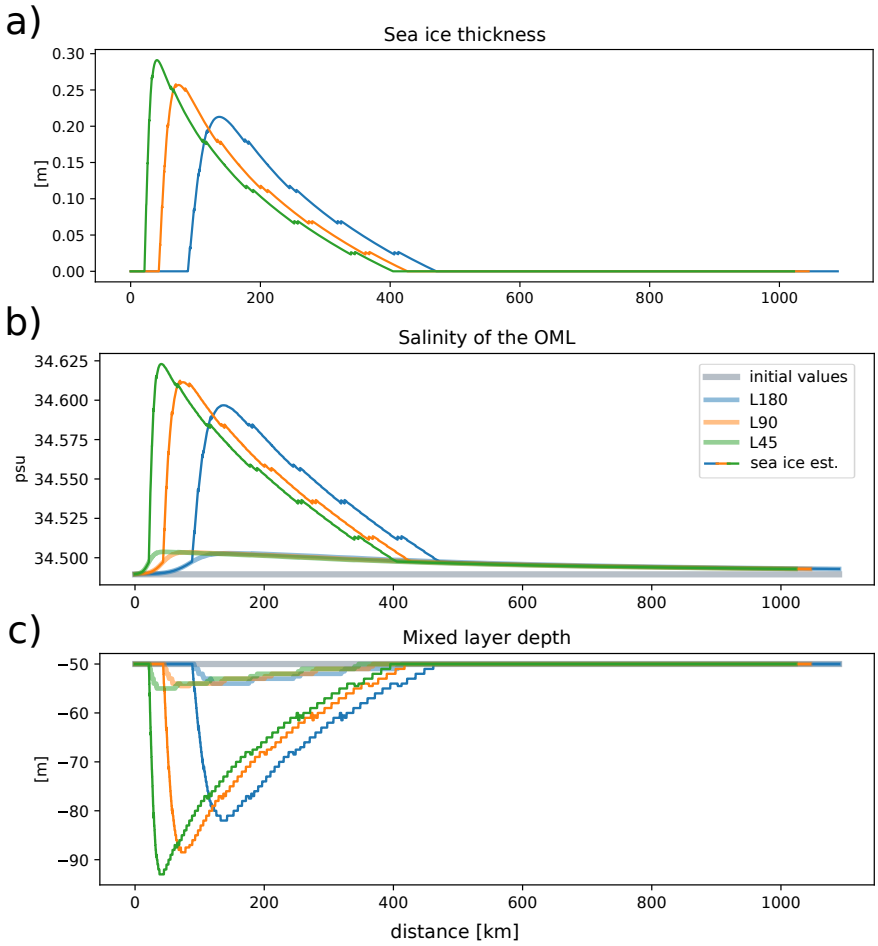

Figure 3.32: Figure showing the impact of sea ice on the OML properties, and the mixed layer depth in particular. For tanh sea ice distribution, moisture on, and $\tau = 5$, and showing the different widths, where L180, L90, L45 represents 180 km, 90 km and 45 km width of the MIZ, respectively. Further, the thicker, transparent lines are the original results from the model and the thinner and stronger-coloured lines are the estimates when the effect of sea ice is taken into account.

on the OML properties, the effect of the coupling must be interpreted with caution. It highlights one of the important limitation of this model, namely that it does not include sea ice formation. The sea ice production described here would possibly lead to a decrease in the heat flux more than the ocean cooling itself, which might impact the structure of the ABL more than the coupling through the heat fluxes. Furthermore, as the maximum fluxes happen just off the sea ice, but are sensitive to the shape of the MIZ, the MIZ are important for accurately representing the mixed layer deepening of the ocean. Furthermore, the retreating sea ice in the Nordic Seas change the location of the maximum fluxes, and hence new water masses are exposed and might be ventilated (Våge et al., 2018).

4 Limitations

This study has shown that especially the moisture content, the heating of the layer and the boundary layer height are sensitive to the entrainment rate. The entrainment rate in this model is, however, very simplified. It is generally accepted that the entrainment rate is determined by turbulent kinetic energy in the boundary layer (Stull, 1997). Air is entrained against the buoyancy force and thus entrainment of warm and dry air downward from the inversion requires energy. Whereas other mixed layer models of the cloud topped boundary layer use virtual potential temperature, θ_v (e.g., Stage and Businger, 1981; Pelly and Belcher, 2001; Deardorff, 1976b), we formulate it in terms of potential temperature. The virtual potential temperature is always larger than the potential temperature when moisture is present because it includes the effect of vapour upon buoyancy. The natural counterpart to be used in this model would be the liquid water virtual potential temperature, which has proven to be useful for determining the entrainment velocity in the shallow planetary boundary layer (Marquet, 2011). A more accurate entrainment rate might also provide an even better estimate of the downstream development of the boundary layer height.

Furthermore, some studies have included the effect of radiation upon the entrainment velocity (Stage and Businger, 1981) or reformulated it in terms of the jump in radiative cooling divided by the jump in virtual potential temperature (Pelly and Belcher, 2001). This was shown to give accurate results in terms of the boundary layer height, and could possibly provide better estimates for this mixed layer model as well.

That we have not taken the effect of radiation into account would generally imply that we are underestimating the boundary layer temperature in the ABL and hence overestimating the sensible heat flux (Renfrew and King, 2000). However, the precipitation does not evaporate below the cloud layer, which would have caused the potential temperature below the cloud layer to be overestimated. The relative importance of these terms has yet to be explored.

Large scale divergence in CAOs has shown to be important (Brümmer, 1996a). As the air is being advected over the warmer ocean surface, it heats, and consequently sets up a pressure gradient in the along-wind direction (Chechin et al., 2013). The pressure gradients leads to an

acceleration of the wind downstream and hence divergence (Brümmer, 1996b). As the system has to conserve mass, this leads to a large scale subsidence. Subsidence can also be imposed by the synoptic conditions (Fletcher et al., 2016). The process act to dry the boundary layer by entraining dryer air (Brümmer, 1996b), and hence the exaggerated loss of moisture to the free atmosphere, might compensate for the lack of large-scale features in the model.

Moreover, the accelerating winds tend to increase the boundary layer warming primarily through heat flux convergence enhanced by radiative flux convergence and microphysical processes (Renfrew and King, 2000). Neither the wind speed increase nor the radiative effect is taken into account in the model, but unlike Renfrew and King (2000) we have considered the microphysical processes. Renfrew and King (2000) argued that the absence of these processes are compensating as the wind speed would enhance the fluxes, whereas the additional warming by the radiative and microphysical processes would act to decrease the fluxes. In our mixed layer model, the warming of the boundary layer is not sensitive to the magnitude of the wind speed. Therefore, these effects might not be compensating, but rather act to decrease the heat flux from the ocean to the atmosphere. However, this might be sensitive to how we calculate the heat fluxes. Whereas we used a bulk formula for calculating the surface heat fluxes, Renfrew and King (2000) used a more sophisticated routine for the surface flux calculation which yielded heating rates sensitive to the wind speed.

That the moisture behaves according to Clausius-Clapeyron relationship and assuming that the temperature within the cloud follows the moist adiabat is an oversimplification, but the same method is used also on observations to determine the liquid water content in the clouds (e.g. Hartmann et al., 1997). The estimates of the liquid water content might therefore be on the high end of what is expected. However, we have overestimated the loss of moisture to the free atmosphere. These two processes might therefore be compensating, and hence give us reasonable results for the wrong reason.

Furthermore, we have assumed liquid water within the clouds. During CAOs, very cold air is being advected over the open water, and it would therefore have been more appropriate to assume ice or mixed phase clouds instead. The saturation vapour pressure is lower over ice than over water, such that if ice particles were considered in the cloud instead of liquid water, the cloud base would extend lower. The sublimation of water, and hence ice formation, release more energy than the condensation of water, which would cause enhanced warming of the cloud layer. However, the latent heat of sublimation is not significantly larger than the latent heat of vaporization (2.8×10^6 J/kg compared to 2.5×10^6) J/kg). Hence, we believe the difference to be small.

Caution must be taken as we have tuned the transfer coefficients to give budget ratios and the ABL structure most similar to observations from two flight campaigns, which both measured

CAOs over the Fram Strait in 1991 and 1993. Furthermore, we kept the routine for calculating the surface fluxes simple. A more sophisticated routine like the one by Renfrew and King (2000) based on Monin-Obukhov theory might provide more realistic results. The tuning of the coefficients yielded a good representation of the structure of the ABL and budget ratios when compared to the estimates by Brümmer (1996b), but the actual heat fluxes were overestimated compared to observations by Hartmann et al. (1997). However, an inadequate representation of fluxes would potentially also impact the ocean mixed layer. The representation of fluxes in high latitudes is challenging, but crucial for getting the right energy balance between the atmosphere and the ocean (Bourassa et al., 2013).

The OML model is less complex compared to its atmospheric counterpart. The initial focus was on the development of the atmospheric boundary layer structure during CAOs, and hence there was less time for the development of the OML. There is no entrainment from the underlying water, and hence, it is simpler than other mixed layer models (e.g. Niiler and Kraus, 1977; Stephens et al., 2005; Price et al., 1986). Entrainment with the underlying water column would cause the temperature in the mixed layer to decrease less as the water underneath is generally warmer at high latitudes. The oceanic response to the atmospheric heat flux might therefore be different than what is modelled here. This thus remains as task for future development of the model.

Previous studies have shown that the main factor of the coupling is not through the heat fluxes, but rather the momentum fluxes, through changes in currents and upwelling (Xue et al., 2002). We have not considered mixing due to wind stress in the ocean, which would act to entrain water from below the pycnocline into the mixed layer. Furthermore, there are complex surface currents within the MIZ (Häkkinen, 1986), which, depending on the shape of the MIZ might lead to upwelling close to the sea ice edge. Depending on the properties of the water column, this upwelling might actually bring up warmer waters which would lead to enhanced sensible heat fluxes and perhaps act against the surface cooling.

One important limitation of the model is that the sea ice concentration is treated as a static quantity. Not only is the MIZ highly dynamic, and changing depending on the wind etc. (e.g. Häkkinen, 1986), but sea ice formation is not included either. This implies that even though the water is cooled to the freezing point, it will only continue to cool. The real ocean does not cool below freezing, but instead forms sea ice. Sea ice formation, in addition to insulating the ocean from the atmospheric heat fluxes, is also important because of brine rejection. Brine rejection is thought to be important for deep water formation in both the Arctic (Aagaard et al., 1985; Årthun et al., 2011; Marshall and Schott, 1999) and around Antarctica (Nicholls et al., 2009).

However, in order for deep convection to occur, it is necessary for the stratification to be

weak enough (Brakstad et al., 2018). Lateral advection of temperature and salinity is important for setting the stratification in the ocean. Brakstad et al. (2018) used a 1-D model to investigate the most important factors contributing to the deep water formation in the Greenland Sea, and found the turbulent heat fluxes to be most important. Sea ice formation also contributed to the mixed layer depths in some winters, but the effect was not strong enough to result in convection beyond 400 m (Brakstad et al., 2018). Lateral advection, and hence the possibility of restratifying the ocean is not taken into account in this model. However, as this model focus only on episodic events of CAO, the relative importance of the lateral advection remain uncertain.

The results shown here calculated the largest possible amount of brine that could be rejected from the sea ice. As this is an upper estimate, it showcases the possibility of the sensitivity that deep water formation can have to the input of salinity. However, the effects of the brine rejection here are exaggerated. Even if this much sea ice formed during a CAO, the brine rejection would have mixed more gradually with the underlying water, and might even have brought up warmer waters from underneath the pycnocline. This warmer water could possible have provided a heat supply efficient enough to melt some of the sea ice, or slow down further growth of sea ice as the additional heat must be removed to reach the freezing point again.

Due to these processes and their ability to limit the sea ice production, caution must be taken when interpreting the presented results. The estimates given in this work solely look at the highest possible values from a thermodynamic perspective, and only show that brine rejection from sea ice formation could be an important driver for mixed layer deepening. Brakstad et al. (2018) found that whenever sea ice actually did form in the Greenland Sea Gyre, the surface water was initially too fresh for convection to reach greater depths. However, while Brakstad et al. (2018) looks at the change in mixed layer deepening through an entire winter, we consider the effect of an individual CAO. We examine the changes in OML properties during an individual CAO, which shows that over a mixed layer depth of 50 m, the cooling can be sufficient to form sea ice. If no sea ice forms, the salinity change is insignificant. However, whether sea ice formation actually occurs during a CAO appears to be an unanswered question.

5 Summary and conclusions

We raised the following questions in the introduction;

- Is the mixed layer model able to realistically represent the ABL structure during CAOs?
- How does moisture affect ABL characteristics?
- Does the coupling between the atmosphere and the ocean impact the fluxes and the structure of the ABL?
- How does the distribution of sea ice affect the structure of the ABL through coupling?

We are able to reproduce central ABL characteristics with our mixed model. Given the simplicity of the model, the structure is rather well represented in the ABL. The moisture content has a tendency to be underestimated compared to observations, which we have attributed to an overestimation of loss of moisture to the free atmosphere. After tuning the coefficients to make the model more consistent to observations, we get budget ratios similar to Brümmer (1996b). That the budget ratios are correct indicate that the pertinent processes are well represented in the model.

Moisture is important for the ABL structure in CAOs. It acts to increase the potential temperature in the mixed layer, and through latent heat release in the cloud layer, the boundary layer height increases. In the mean, condensation heating accounts for roughly 12% of the ABL heating when a cloud is present in the domain. However, the condensation rates and their relative importance is lower than what Brümmer (1996b) estimated.

Furthermore, Papritz and Sodemann (2018) argued that CAOs are important for the freshwater balance in the Arctic. In our mixed layer model, we never have enough freshwater input by precipitation during CAOs to actually decrease the salinity in the mixed layer of the ocean. There is always a salinification of the OML due to evaporation, which is consistent with the findings by Papritz and Sodemann (2018). However, the contribution to the salinity budgets in the ocean mixed layer is small when we only consider changes due to evaporation and precipitation. This indicates that an individual CAO does not have a substantial impact on the freshwater

flux to the ocean. Furthermore, the temperature changes associated with CAOs are much larger than the salinity changes, which may imply that cooling is more important for ocean mixed layer deepening than the increase in salinity.

The coupling affects the domain-integrated sensible heat flux, and as the ocean cools, the integrated heat fluxes decrease. This leads to slightly lower temperatures in the atmosphere, but the coupling in general seems not to be important for the ABL structure, similar to the discovery by Xue et al. (2002). However, when the ocean stratification is strong and the mixed layer shallow, the temperature in the ocean can change enough to impact the latent heat flux several hundred kilometres downstream. The effect of the coupling strengthens when moisture is included. Not including the latent heat flux from the ocean is equivalent to neglecting almost 40% of the oceanic heat loss, and hence the ocean mixed layer temperature decreases further. The main effect of the coupling is not through the integrated sensible heat flux, but rather through moisture content and the onset of clouds in the ABL. Therefore, neglecting moisture when the ocean is coupled to atmosphere could yield erroneous results on the importance of the coupling, because 1) the ocean does not cool through the latent heat flux and 2) the coupling impact the moist properties of the ABL and the onset of clouds rather than the standard parameters; such as boundary layer height and potential temperature.

Lastly, we investigated the effects of different sea ice distributions on the coupling and ABL structure. The distribution of the sea ice had a marginal impact on the domain-integrated sensible heat fluxes, even when coupling was included, and the ABL structure did not differ much for the different sea ice distributions downstream of the sea ice edge. The results are consistent with Liu et al. (2006) who showed that the ABL had a relatively short memory of the upstream sea ice conditions. Rather, it is the fetch over open water that is important.

Hence, the different sea ice distributions are not important for the domain-integrated quantities, but it matters a lot for the distribution of fluxes and the ocean cooling. However, the feedback to the atmosphere resulting from this ocean cooling is small. We used a constant SST away from the sea ice edge, and in reality the sea surface temperature tend to increase away from the sea ice edge. This could possibly alter the distribution of the fluxes further, and also change the location of the maximum heat loss.

The sea ice distribution, and also the MIZ width, does matter for the OML properties. The abrupt transition between fast ice and open water are associated with higher maximum heat fluxes, and are therefore also associated with deeper mixed layer depths and greater cooling. The model does not take into account sea ice formation, but calculations show that up to 30 cm of sea ice can be formed, which would yield an additional salinity flux that may have profound impact on the mixed layer depth of the ocean.

6 Outlook - recommendations for further studies

This thesis has covered some basic setups of the model. Further sensitivities should be explored, and more comprehensive testing against observations. Furthermore, the testing against observations in this thesis has been rather limited and a more in-depth testing against airplane data would be valuable. Furthermore, testing this model to more sophisticated models may help determine the validity of the results presented here.

A more thorough study on the effect of the coefficients should be performed. In the MIZ-experiment, we kept the transfer coefficient over sea ice constant. As these coefficients depend, among other things, on the roughness of the surface, changing the coefficients could make the MIZ have a stronger impact on the downstream development. (Pagowski and Moore, 2001) comes with a suggestion on how to let the heat and moisture coefficients to vary, and the study further showed that the representation of the MIZ had a profound effect on the downstream development.

The coefficients we use for precipitation also deviates from the standard coefficient in literature (Stensrud, 2011, explained in section 2.1.2). A more detailed analysis of the the precipitation parameterization could be performed. Furthermore, more appropriate parameterizations for precipitation could be explored.

The results presented here covered some basic sensitivity tests, but additional tests could provide interesting results. For example, as both the SST distribution and the sea ice distribution are important for the distribution of the fluxes, their relative importance could be explored in a combined sensitivity test.

Apart from more sensitivity studies, the model can also be improved;

Moist(er) background We showed that entrainment often cause the moisture in the mixed layer to be underestimated. To use another approximation than a completely dry atmosphere above the mixed layer might be important. Furthermore, we developed a method to use piecewise

linear profiles for the ambient stability of the atmosphere. However, due to time constrictions, these were not properly investigated. A similar approach could also be used on the background moisture content of the atmosphere, which might allow for the use of idealized radiosondes as initial conditions, not only for the background temperature, but also for the moisture content.

Ice or mixed phase clouds. We only included liquid water in the model which might not be the best assumption during CAOs as the temperatures are sufficiently low for water vapour to turn into ice and not liquid water. A detailed description on the formulation of the ice liquid water potential temperature can be found in Bryan and Fritsch (2004), which also discuss a formulation for the mixed-phase clouds potential temperature. The subsequent study of the ABL properties will be interesting as most mixed layer models that has been used to study the cloud topped boundary layer with mixed layer model has all been in the formulation of either equivalent potential temperature or liquid water potential temperature or been dry (Stage and Businger, 1981; Deardorff, 1976a; Pelly and Belcher, 2001; Renfrew and King, 2000; Økland, 1983).

Entrainment in the ocean model. As discussed previously, the mixed layer model of the ocean is underdeveloped compared to its atmospheric counterpart. A natural extension of the ocean mixed layer model would be to include the effect of entrainment by finding an equation for Δb that differs from the one outlined in section 2.2. If this is possible it would be possible to include the effect of entrainment from the pycnocline into the mixed layer. The effect of entrainment might alter the oceanic response, as the entrainment might act as a heat source to the mixed layer and therefore limit the cooling to a larger extent.

Formation of sea ice. The other major issue with the ocean mixed layer model is that the formation of sea ice is not included. It might be useful to spend time developing a way to include the sea ice formation as sea ice will increase the salinity flux to the ocean and also alter the heat flux as it insulates the ocean from the atmosphere.

A Possible extensions of the model (implemented, but not explored)

A.1 Using radiosondes

A strong inversion is almost always present over the Arctic (Guest et al., 1995), but atop is often a layer of less stratified air. (Renfrew and King, 2000) pointed out that for climatological studies, there is a need to be able to represent both the inversion and the less stratified layer above. If the surface layer is eroded, this will cause the subsequent mixing to be more efficient. To account for how the temperature profile changes downstream, we may create piecewise linear profiles such that the lapse rate is no longer constant with height.

We create linear segments out of radiosonde-data (e.g. Jeske et al. (2012)) based on linear least squares fit. We assume that three line segments are sufficient to accurately represent the background temperature, and use the *pwlf*[1] package for python. Figure A.1 shows how a piecewise linear profile looks like.

[1] Full documentation is available at `https://jekel.me/piecewise_linear_fit_py/how_it_works.html`

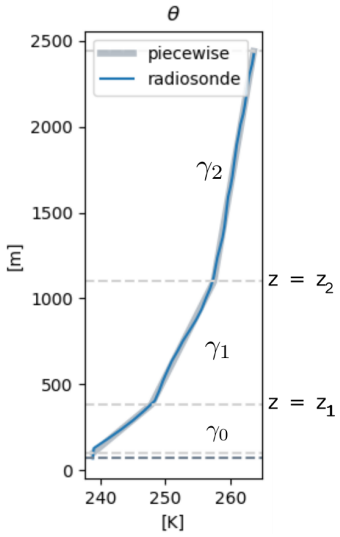

Figure A.1: Temperature profile taken from the ship *Polarstern* 5 March 1993, at 10:30. The grey line indicates the piecewise linear profile hat is used to approximate the radiosonde data.

As the background temperature profile γ_θ is no longer constant, we need to modify the equations for the jump in potential temperature and boundary layer height. The jump in potential temperature is still written as

$$\Delta\theta = \theta^b(z) - \theta \ . \tag{A.1}$$

θ^b is the background temperature, which must take into account that the lapse rate is no longer constant with height, and depending on h, it is written as

$$\theta^b = \theta_0 + \begin{cases} \gamma_0 h & h \leq z_1 \\ \gamma_1(h - z_1) + \gamma_0 z_1 & z_1 < h \leq z_2 \\ \gamma_2(h - z_2) + \gamma_1(z_1 - z_2) + \gamma_0 z_1 & z_2 < h \end{cases} \ . \tag{A.2}$$

The symbols in (A.2) are explained in figure A.1. We differentiate (A.2) with respect to x, and evaluate at $z = h$. This yields:

$$\frac{\partial \Delta\theta}{\partial x} = \frac{\partial \theta^b}{\partial x} - \frac{\partial \theta}{\partial x} \ , \tag{A.3}$$

which can be written as;

$$\frac{\partial \Delta\theta}{\partial x} = \frac{\partial \theta^b}{\partial h}\frac{\partial h}{\partial x} - \frac{\partial \theta}{\partial x} \ . \tag{A.4}$$

(A.4) in its full form reads

$$\frac{\partial \Delta\theta}{\partial x} = -\frac{\partial \theta}{\partial x}|_{z=h} + \frac{\partial h}{\partial x} \begin{cases} \gamma_0 & h \leq z_0 \\ \gamma_1 & z_0 \leq h \leq z_1 \\ \gamma_2 & z_1 \leq h \end{cases} . \tag{A.5}$$

We combine (2.22) and (2.14) and rewrite (A.5) to

$$\frac{\partial \Delta\theta}{\partial x} = -\frac{\partial \theta}{\partial x}|_{z=h} + \frac{\Upsilon \overline{w'\theta'}|_{z=0}}{\Delta\theta \bar{u}} \begin{cases} \gamma_0 & h \leq z_0 \\ \gamma_1 & z_0 \leq h \leq z_1 \\ \gamma_2 & z_1 \leq h \end{cases} . \tag{A.6}$$

In addition, we have to modify the equation for the boundary layer height;

$$h = \begin{cases} \frac{1}{\gamma_0} \\ \frac{1}{\gamma_1} \\ \frac{1}{\gamma_2} \end{cases} \left(\Delta\theta - \theta_0 + \theta|_{z=h} + \begin{cases} 0 & h \leq z_0 \\ z_1(\gamma_1 - \gamma_0) & z_0 \leq h \leq z_1 \\ z_2(\gamma_2) - \gamma_1(z_2 - z_1) - \gamma_0 z_1 & z_1 \leq h \end{cases} \right) . \tag{A.7}$$

Note that, if there is a weakly stratified layer above the strong inversion, problems of convergence might occur. An inversion always has to be present for the model to give physically realistic results as it is one of the main assumptions when deriving the equations for the model.

Bibliography

K. Aagaard, J. H. Swift, and E. C. Carmack. Thermohaline circulation in the Arctic Mediterranean Seas. *Journal of Geophysical Research*, 90(C3):4833–4846, 1985. ISSN 0148-0227. doi: 10.1029/JC090iC03p04833. URL `http://doi.wiley.com/10.1029/JC090iC03p04833`.

M. Årthun, R. B. Ingvaldsen, L. H. Smedsrud, and C. Schrum. Dense water formation and circulation in the Barents Sea. *Deep-Sea Research Part I: Oceanographic Research Papers*, 58(8):801–817, 2011. ISSN 09670637. doi: 10.1016/j.dsr.2011.06.001.

M. A. Bourassa, S. T. Gille, C. Bitz, D. Carlson, I. Cerovecki, C. A. Clayson, M. F. Cronin, W. M. Drennan, C. W. Fairall, R. N. Hoffman, G. Magnusdottir, R. T. Pinker, I. A. Renfrew, M. Serreze, K. Speer, L. D. Talley, and G. A. Wick. High-latitude ocean and sea ice surface fluxes: Challenges for climate research. *Bulletin of the American Meteorological Society*, 94(3):403–423, 2013. ISSN 00030007. doi: 10.1175/BAMS-D-11-00244.1.

T. Boyer, O. Baranova, M. Biddle, D. Johnson, A. Mishonov, C. Paver, D. Seidov, and M. Zweng. Arctic Ocean Regional Climatology (NCEI Accession 0115771). Version 2.2. *NOAA National Centers for Environmental Information. Dataset.*, 2015. doi: 10.7289/V5QC01J0.

A. Brakstad, K. Våge, L. Håvik, and G. W. K. Moore. Water Mass Transformation in the Greenland Sea during the Period 1986–2016. *Journal of Physical Oceanography*, 49(1):121–140, 2018. ISSN 0022-3670. doi: 10.1175/jpo-d-17-0273.1.

B. Brümmer. Boundary-layer modification in wintertime cold-air outbreaks from the arctic sea ice. *Boundary-Layer Meteorology*, 80(1-2):109–125, 1996a. ISSN 00068314. doi: 10.1007/BF00119014.

B. Brümmer. Boundary Layer Mass, Water, and Heat Budgets in Wintertime Cold-Air Outbreaks from the Arctic Sea Ice. *Monthly Weather Review*, 125(8):1824–1837, 1996b. ISSN 0027-0644. doi: 10.1175/1520-0493(1997)125<1824:blmwah>2.0.co;2.

G. H. Bryan and J. M. Fritsch. A Reevaluation of Ice–Liquid Water Potential Temperature. *Monthly Weather Review*, 132(10):2421–2431, 2004. ISSN 0027-0644. doi: 10.1175/1520-0493(2004)132<2421:aroiwp>2.0.co;2.

S. S. Chang and R. R. Braham. Observational Study of a Convective Internal Boundary Layer over Lake Michigan. *Journal of the Atmospheric Sciences*, 48(20):2265–2279, 1991. ISSN 0022-4928. doi: 10.1175/1520-0469(1991)048<2265:osoaci>2.0.co;2.

S.-Y. Chao. An air-sea interaction model for cold-air outbreaks. *Journal of Physical Oceanography*, 22:821–842, 1992.

D. G. Chechin, C. Lüpkes, I. A. Repina, and V. M. Gryanik. Idealized dry quasi 2-D mesoscale simulations of cold-air outbreaks over the marginal sea ice zone with fine and coarse resolution. *Journal of Geophysical Research Atmospheres*, 118(16):8787–8813, 2013. ISSN 21698996. doi: 10.1002/jgrd.50679.

J. A. Curry, W. B. Rossow, D. Randall, and J. L. Schramm. Overview of arctic cloud and radiation characteristics. *Journal of Climate*, 9(8):1731–1764, aug 1996. ISSN 08948755. doi: 10.1175/1520-0442(1996)009<1731:OOACAR>2.0.CO;2. URL http://journals.ametsoc.org/doi/abs/10.1175/1520-0442{%}281996{%}29009{%}3C1731{%}3AOOACAR{%}3E2.0.CO{%}3B2.

B. Cushman-Roisin and J.-M. Beckers. *Introduction to Geophysical Fluid Dynamics: Physical and Numerical Aspects*, volume 101 of *International Geophysics*. Elsevier Science, 2 edition, 2011. ISBN 0120887592.

J. W. Deardorff. Usefulness of liquid-water potential temperature in a shallow-cloud model, 1976a. ISSN 0021-8952.

J. W. Deardorff. On the entrainment rate of a stratocumulus topped mixed layer. *Quarterly Journal of the Royal Meteorological Society*, 102(433):563–582, 1976b. ISSN 1477870X. doi: 10.1002/qj.49710243306.

T. Eldevik, J. E. Ø. Nilsen, D. Iovino, K. Anders Olsson, A. B. Sandø, and H. Drange. Observed sources and variability of Nordic seas overflow. *Nature Geoscience*, 2(6):406–410, 2009. ISSN 1752-0894. doi: 10.1038/ngeo518. URL http://www.nature.com/doifinder/10.1038/ngeo518.

Fernandes. python-seawater v3.3.2, aug 2014. URL https://zenodo.org/record/11395.

J. Fletcher, S. Mason, and C. Jakob. The climatology, meteorology, and boundary layer structure of marine cold air outbreaks in both hemispheres. *Journal of Climate*, 29(6):1999–2014, 2016. ISSN 08948755. doi: 10.1175/JCLI-D-15-0268.1.

N. P. Fofonoff and R. C. Millard Jr. Algorithms for the computation of fundamental properties of seawater. *UNESCO Technical Papers in Marine Sciences*, 44, 1983. URL http://hdl.handle.net/11329/109.

J. R. Garratt. The atmospheric boundary layer. Cambridge atmospheric and space science series, page 316. Cambridge University Press, Cambridge, 1992. ISBN 0521380529.

P. S. Guest, K. L. Davidson, J. E. Overland, and P. A. Frederickson. Atmosphere-Ocean Interactions in the Marginal Ice Zones of the Nordic Seas. *Arctic Oceanography: Marginal Ice Zones and Continental Shelves. Coastal and Estuarine Studies*, 49:51–95, 1995.

S. Häkkinen. Coupled ice-ocean dynamics in the marginal ice zones: Upwelling/downwelling and eddy generation. *Journal of Geophysical Research*, 91(C1):819, 1986. ISSN 0148-0227. doi: 10.1029/JC091iC01p00819. URL http://doi.wiley.com/10.1029/JC091iC01p00819.

D. L. Hartmann. Chapter 4 - The Energy Balance of the Surface. In D. L. Hartmann, editor, *Global Physical Climatology (Second Edition)*, pages 95–130. Elsevier, Boston, second edi edition, 2016. ISBN 978-0-12-328531-7. doi: https://doi.org/10.1016/B978-0-12-328531-7.00004-9. URL http://www.sciencedirect.com/science/article/pii/B9780123285317000049.

J. Hartmann, C. Kottmeier, and S. Raasch. Roll Vortices and Boundary-Layer Development During a Cold Air Outbreak. *Boundary-Layer Meteorology*, (1992):45–65, 1997.

P. E. Isachsen, M. Drivdal, S. Eastwood, Y. Gusdal, G. Noer, and O. Saetra. Observations of the ocean response to cold air outbreaks and polar lows over the Nordic Seas. *Geophysical Research Letters*, 40(14):3667–3671, 2013. ISSN 00948276. doi: 10.1002/grl.50705.

H. Jeske, G. Kruspe, B. Brümmer, A. Nagurny, G. Müller, and C. Wetzel. ARKTIS 1993 - Air mass modification and convection in off-ice air flows over Fram Strait: meteorological measurements of the research aircraft Falcon and radiosoundings at the research vessels Valdivia, Polarstern and Prof. Multanovsky and at 4 land stati. *World Data Center for Climate (WDCC) at DKRZ. Dataset.*, 2012. doi: 10.1594/WDCC/UNI_HH_MI_ARKTIS1993. URL https://doi.org/10.1594/WDCC/UNI{_}HH{_}MI{_}ARKTIS1993.

V. I. Khvorostyanov and J. A. Curry. Thermodynamic Relations. In *Thermodynamics, kinetics, and microphysics of Clouds*, pages 73–95. Cambridge University Press, 2014. ISBN 978-1-107-01603-3.

E. W. Kolstad. A global climatology of favourable conditions for polar lows. *Quarterly Journal of the Royal Meteorological Society*, 137(660):1749–1761, 2011. ISSN 00359009. doi: 10.1002/qj.888.

E. W. Kolstad and T. J. Bracegirdle. Marine cold-air outbreaks in the future: An assessment of IPCC AR4 model results for the Northern Hemisphere. *Climate Dynamics*, 30(7-8):871–885, 2008. ISSN 09307575. doi: 10.1007/s00382-007-0331-0.

M. Leppäranta. A review of analytical models of sea-ice growth. *Atmosphere-Ocean*, 31(1):123–138, 1993. ISSN 0148-0227. doi: 10.1080/07055900.1993.9649465. URL `http://onlinelibrary.wiley.com/doi/10.1029/JC094iC10p14485/full{%}5Cnhttp://doi.wiley.com/10.1029/JC094iC10p14485{%}5Cnhttp://onlinelibrary.wiley.com/doi/10.1029/JC092iC04p03778/full{%}5Cnhttp://doi.wiley.com/10.1029/JC092iC04p03778{%}5Cnhttp://onlinelibrary.wile`.

Y. Li. Air-sea interactions during the passage of a winter storm over the Gulf Stream: A three-dimensional coupled atmosphere-ocean model study. *Journal of Geophysical Research*, 107(C11):1–13, 2002. ISSN 0148-0227. doi: 10.1029/2001jc001161.

A. Q. Liu, G. W. K. Moore, K. Tsuboki, and I. A. Renfrew. The effect of the sea-ice zone on the development of boundary-layer roll clouds during cold air outbreaks. *Boundary-Layer Meteorology*, 118(3):557–581, 2006. ISSN 00068314. doi: 10.1007/s10546-005-6434-4.

P. R. Lowe and J. N. Ficke. The computation of saturation vapour pressure. *Environmental Prediction Research Facility (Navy) Monterey, California. Distributed by NTIS National Tehcnical Information Service, U.S. Department of Commerce*, (March), 1974.

P. Marquet. Definition of a moist entropy potential temperature: Application to FIRE-I data flights. *Quarterly Journal of the Royal Meteorological Society*, 137(656):768–791, 2011. ISSN 00359009. doi: 10.1002/qj.787.

J. Marshall and F. Schott. Open-ocean convection: Observations, theory, and models. *Reviews of Geophysics*, 37 (1):1–64, 1999. ISSN 87551209. doi: 10.1029/98RG02739.

G. W. K. Moore, R. Swinbank, G. N. Petersen, R. S. Pickart, J. E. Kristjánsson, D. Sproson, S. L. Gray, E. A. Irvine, S. Zhang, H. Ólafsson, I. A. Renfrew, T. Haine, C. Hay, A. Woolley, K. Bovis, A. Lawrence, M. Shapiro, S. Outten, T. Ohigashi, P. R. A. Brown, and I. Føre. THE GREENLAND FLOW DISTORTION EXPERIMENT. *Bulletin of the American Meteorological Society*, 89(9):1307–1324, 2008. ISSN 0003-0007. doi: 10.1175/2008bams2508.1.

G. W. K. Moore, K. Vage, R. S. Pickart, and I. A. Renfrew. Decreasing intensity of open-ocean convection in the Greenland and Iceland seas. *Nature Climate Change*, 5(9):877–882, 2015. ISSN 17586798. doi: 10.1038/nclimate2688.

K. W. Nicholls, S. Østerhus, K. Makinson, T. Gammelsrød, and E. Fahrbach. Ice-ocean processes over the continental shelf of the southern Weddell Sea, Antarctica: A review. *Reviews of Geophysics*, 47(3):RG3003, jul 2009. ISSN 8755-1209. doi: 10.1029/2007RG000250. URL `http://www.eos.ubc.ca/{~}mjelline/453website/eosc453/E{_}prints/newfer010/Nicholls{_}iceocean{_}antarctica{_}RG09.pdf{%}5Cnpapers://2e7eb9ea-3d62-4a3f-aa55-889be2e26302/Paper/p1030http://doi.wiley.com/10.1029/2007RG000250`.

P. Niiler and E. B. Kraus. *One-Dimensional Models of the upper ocean*. Pergamon Press, 1977.

H. Økland. Modelling the height, temperature and relative humidity of a well-mixed planetary boundary layer over a water surface. *Boundary-Layer Meteorology*, 25(2):121–141, feb 1983. ISSN 0006-8314. doi: 10.1007/BF00123970. URL `http://openurl.ingenta.com/content/xref?genre=article{&}issn=0167-5427{&}volume=33{&}issue=4{&}spage=415http://link.springer.com/10.1007/BF00123970`.

M. Pagowski and G. W. K. Moore. A Numerical Study of an Extreme Cold-Air Outbreak over the Labrador Sea: Sea Ice, Air–Sea Interaction, and Development of Polar Lows. *Monthly Weather Review*, 129(1):47–72, 2001. ISSN 0027-0644. doi: 10.1175/1520-0493(2001)129<0047:ANSOAE>2.0.CO;2. URL `http://journals.ametsoc.org/doi/full/10.1175/1520-0493(2001)129{%}3C0047:ANSOAE{%}3E2.0.CO{%}3B2`.

L. Papritz and H. Sodemann. Characterizing the Local and Intense Water Cycle during a Cold Air Outbreak in the Nordic Seas. *Monthly Weather Review*, 146(11):3567–3588, 2018. ISSN 0027-0644. doi: 10.1175/mwr-d-18-0172.1.

L. Papritz and T. Spengler. A Lagrangian climatology of wintertime cold air outbreaks in the Irminger and Nordic Seas and their role in shaping air-sea heat fluxes. *Journal of Climate*, 30(8):2717–2737, 2017. ISSN 08948755. doi: 10.1175/JCLI-D-16-0605.1.

L. Papritz, S. Pfahl, H. Sodemann, and H. Wernli. A climatology of cold air outbreaks and their impact on air-sea heat fluxes in the high-latitude South Pacific. *Journal of Climate*, 28(1):342–364, 2015. ISSN 08948755. doi: 10.1175/JCLI-D-14-00482.1.

J. L. Pelly and S. E. Belcher. A mixed-layer model of the well-mixed stratocumulus-topped boundary layer. *Boundary-Layer Meteorology*, 100(1):171–187, 2001. ISSN 00068314. doi: 10.1023/A:1019215221726.

W. H. Press, S. Teukolsky, W. Vetterling, and B. Flannery. Integration of Functions. In *Fortran numerical recipes: Vol. 1: Numerical recipes in Fortran 77: the art of scientific computingt*, chapter 4, pages 123–134. Cambridge University Press, Cambridge, 2nd ed. edition, 1996a. ISBN 052143064X.

W. H. Press, S. Teukolsky, W. Vetterling, and B. Flannery. Integration of Ordinary Differential Equations. In *Fortran numerical recipes: Vol. 1: Numerical recipes in Fortran 77: the art of scientific computing*, volume Vol. 1, chapter 16, pages 700–708. Cambridge University Press, Cambridge, 2nd ed. edition, 1996b. ISBN 052143064X.

J. F. Price, R. A. Weller, and R. Pinkel. Diurnal cycling: Observations and models of the upper ocean response to diurnal heating, cooling, and wind mixing. *Journal of Geophysical Research*, 91(C7):8411, 1986. ISSN 0148-0227. doi: 10.1029/JC091iC07p08411. URL `http://doi.wiley.com/10.1029/JC091iC07p08411`.

I. a. Renfrew and J. C. King. a Simple Model of the Convective Internal Boundary. *Boundary Layer Meteorology*, 94(1984):335–356, 2000.

S. D. Smith, R. D. Muench, and C. H. Pease. Polynyas and leads: An overview of physical processes and environment. *Journal of Geophysical Research*, 95(C6):9461, 1990. ISSN 0148-0227. doi: 10.1029/JC095iC06p09461. URL `http://doi.wiley.com/10.1029/JC095iC06p09461`.

S. A. Stage. Factors influencing the marine boundary layer during a cold-air outbreak. *Boundary-Layer Meteorology*, 26(3):269–287, jul 1983. ISSN 0006-8314. doi: 10.1007/BF00121402. URL `http://link.springer.com/10.1007/BF00121402`.

S. A. Stage and J. A. Businger. A Model for Entrainment into a Cloud-Topped Marine Boundary Layer. Part I: Model Description and Application to a Cold-Air Outbreak Episode, 1981. ISSN 0022-4928.

D. J. Stensrud. Microphysics parameterizations. In *Parameterization Schemes: Keys to Understanding Numerical Weather Prediction Models*, volume 9780521865, chapter 7, page 281. Cambridge University Press, Cambridge, 2011. ISBN 9780511812590. doi: 10.1017/CBO9780511812590. URL `http://ebooks.cambridge.org/ref/id/CBO9780511812590`.

M. Y. Stephens, R. J. Oglesby, and M. Maxey. A one-dimensional mixed layer ocean model for use in three-dimensional climate simulations: Control simulation compared to observations. *Journal of Climate*, 18(13): 2199–2221, 2005. ISSN 08948755. doi: 10.1175/JCLI3380.1.

B. Stevens. On the Growth of Layers of Nonprecipitating Cumulus Convection. *Journal of the Atmospheric Sciences*, 55(24):3616–3638, 2007. ISSN 0022-4928. doi: 10.1175/1520-0469(1998)055<3616:lesosp>2.0.co;2.

C. Strong. Atmospheric influence on Arctic marginal ice zone position and width in the Atlantic sector, February-April 1979-2010. *Climate Dynamics*, 39(12):3091–3102, 2012. ISSN 09307575. doi: 10.1007/s00382-012-1356-6.

R. B. Stull. Chapter 11 - Convective Mixed Layer. In *An introduction to boundary layer meteorology*, volume vol. 13 of *Atmospheric and oceanographic sciences library*, pages 441–493. Springer, Dordrecht, repr. with edition, 1997.

L. D. Talley. *Descriptive physical oceanography: an introduction*. Elsevier/Academic Press, Amsterdam, 6th ed. edition, 2011. ISBN 9780750645522.

K. Våge, G. W. K. Moore, S. Jónsson, and H. Valdimarsson. Water mass transformation in the iceland sea. *Deep-Sea Research Part I: Oceanographic Research Papers*, 101:98–109, 2015. ISSN 09670637. doi: 10.1016/j.dsr.2015.04.001. URL `http://dx.doi.org/10.1016/j.dsr.2015.04.001`.

K. Våge, L. Papritz, L. Håvik, M. A. Spall, and G. W. Moore. Ocean convection linked to the recent ice edge retreat along east Greenland. *Nature Communications*, 9(1), 2018. ISSN 20411723. doi: 10.1038/s41467-018-03468-6. URL `http://dx.doi.org/10.1038/s41467-018-03468-6`.

P. Wadhams. *Ice in the Ocean*. Gordon and Breach Science Publishers, Amsterdam, 1 edition, 2000. ISBN 90-5699-296-1.

H. Xue, Z. Pan, and J. M. Bane. A 2D Coupled Atmosphere–Ocean Model Study of Air–Sea Interactions during a Cold Air Outbreak over the Gulf Stream. *Monthly Weather Review*, 128(4):973–996, 2002. ISSN 0027-0644. doi: 10.1175/1520-0493(2000)128<0973:acaoms>2.0.co;2.